U.S. Department
of Transportation

**Federal Railroad
Administration**

On-Line High-Speed Rail Defect Detection, Part II

Office of Railroad
Policy and Development
Washington, DC 20590

DOT/FRA/ORD-12/02

Final Report
March 2012

REPORT DOCUMENTATION PAGE

Form approved
OMB No. 0704-0188

1. AGENCY USE ONLY (Leave blank)	2. REPORT DATE	3. REPORT TYPE AND DATES COVERED
	March 2012	Technical Report

4. TITLE AND SUBTITLE
On-Line High-Speed Rail Defect Detection, Part II

5. FUNDING NUMBERS
FR-RRD-0001-10-01-00

6. AUTHOR(S)
Stefano Coccia, Robert Phillips, Ivan Bartoli, Salvatore Salamone,
Piervincenzo Rizzo,* Francesco Lanza di Scalea
University of California–San Diego
*University of Pittsburgh

7. PERFORMING ORGANIZATION NAME(S) AND ADDRESS(ES)
University of California–San Diego
Department of Structural Engineering
9500 Gilman Drive, M.C. 0085
La Jolla, CA 92093-0085

8. PERFORMING ORGANIZATION REPORT NUMBERS

9. SPONSORING/MONITORING AGENCY NAME(S) AND ADDRESS(ES)
U.S. Department of Transportation
Federal Railroad Administration
Office of Railroad Policy and Development, MS 20
1200 New Jersey Avenue, SE
Washington, DC 20590

10. SPONSORING/MONITORING AGENCY REPORT NUMBER
DOT/FRA/ORD-12/02

11. SUPPLEMENTARY NOTES
Program Manager: Mahmood Fateh

12a. DISTRIBUTION/AVAILABILITY STATEMENT
This document is available to the public online through the FRA Web site at http://www.fra.dot.gov.

12b. DISTRIBUTION CODE

13. ABSTRACT
The objectives of this project were (1) to improve the defect detection reliability and (2) to improve the inspection speed of conventional rail defect detection methods. The prototype developed in this work uses noncontact transducers, ultrasonic guided waves, and real-time statistical pattern recognition to improve system reliability. The prototype was field tested seven times with the support of the Federal Railroad Administration (FRA) R-4 hy-railer vehicle. The latest tests at Herzog, Inc., in June 2010 showed excellent results. Two blind tests resulted in a defect detection reliability exceeding industry average and American Railway Engineering and Maintenance-of-Way Association recommendations. These tests also proved the potential for distinguishing good welds from defective welds, an excellent detestability of the vertical split head defect, and the potential for characterizing different rail surface conditions for grinding management purposes. Within this project, a 250-foot-long rail defect farm was also constructed at the University of California–San Diego, with in-kind donations from BNSF Railway, for the development of this and other rail inspection technologies of interest to FRA and to the railroad industry.

14. SUBJECT TERMS
Transverse cracks, ultrasonic guided waves, noncontact ultrasonic testing, laser ultrasonic, air-coupled sensors, finite element modeling, automatic defect classification

15. NUMBER OF PAGES
140

16. PRICE CODE

17. SECURITY CLASSIFICATION OF REPORT	18. SECURITY CLASSIFICATION OF THIS PAGE	19. SECURITY CLASSIFICATION OF ABSTRACT	20. LIMITATION OF ABSTRACT
Unclassified	Unclassified	Unclassified	

NSN 7540-01-280-5500

Standard Form 298 (Rev.2-89)
Prescribed by ANSI/NISO Std. 39.18
298-102

METRIC/ENGLISH CONVERSION FACTORS

ENGLISH TO METRIC

LENGTH (APPROXIMATE)

1 inch (in) = 2.5 centimeters (cm)
1 foot (ft) = 30 centimeters (cm)
1 yard (yd) = 0.9 meter (m)
1 mile (mi) = 1.6 kilometers (km)

AREA (APPROXIMATE)

1 square inch (sq in, in^2) = 6.5 square centimeters (cm^2)
1 square foot (sq ft, ft^2) = 0.09 square meter (m^2)
1 square yard (sq yd, yd^2) = 0.8 square meter (m^2)
1 square mile (sq mi, mi^2) = 2.6 square kilometers (km^2)
1 acre = 0.4 hectare (he) = 4,000 square meters (m^2)

MASS - WEIGHT (APPROXIMATE)

1 ounce (oz) = 28 grams (gm)
1 pound (lb) = 0.45 kilogram (kg)
1 short ton = 2,000 pounds (lb) = 0.9 tonne (t)

VOLUME (APPROXIMATE)

1 teaspoon (tsp) = 5 milliliters (ml)
1 tablespoon (tbsp) = 15 milliliters (ml)
1 fluid ounce (fl oz) = 30 milliliters (ml)
1 cup (c) = 0.24 liter (l)
1 pint (pt) = 0.47 liter (l)
1 quart (qt) = 0.96 liter (l)
1 gallon (gal) = 3.8 liters (l)
1 cubic foot (cu ft, ft^3) = 0.03 cubic meter (m^3)
1 cubic yard (cu yd, yd^3) = 0.76 cubic meter (m^3)

TEMPERATURE (EXACT)

[(x-32)(5/9)] °F = y °C

METRIC TO ENGLISH

LENGTH (APPROXIMATE)

1 millimeter (mm) = 0.04 inch (in)
1 centimeter (cm) = 0.4 inch (in)
1 meter (m) = 3.3 feet (ft)
1 meter (m) = 1.1 yards (yd)
1 kilometer (km) = 0.6 mile (mi)

AREA (APPROXIMATE)

1 square centimeter (cm^2) = 0.16 square inch (sq in, in^2)
1 square meter (m^2) = 1.2 square yards (sq yd, yd^2)
1 square kilometer (km^2) = 0.4 square mile (sq mi, mi^2)
10,000 square meters (m^2) = 1 hectare (ha) = 2.5 acres

MASS - WEIGHT (APPROXIMATE)

1 gram (gm) = 0.036 ounce (oz)
1 kilogram (kg) = 2.2 pounds (lb)
1 tonne (t) = 1,000 kilograms (kg) = 1.1 short tons

VOLUME (APPROXIMATE)

1 milliliter (ml) = 0.03 fluid ounce (fl oz)
1 liter (l) = 2.1 pints (pt)
1 liter (l) = 1.06 quarts (qt)
1 liter (l) = 0.26 gallon (gal)
1 cubic meter (m^3) = 36 cubic feet (cu ft, ft^3)
1 cubic meter (m^3) = 1.3 cubic yards (cu yd, yd^3)

TEMPERATURE (EXACT)

[(9/5) y + 32] °C = x °F

QUICK INCH - CENTIMETER LENGTH CONVERSION

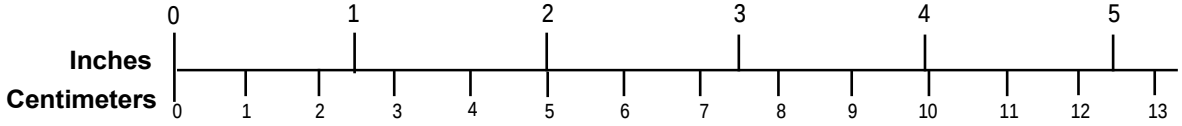

QUICK FAHRENHEIT - CELSIUS TEMPERATURE CONVERSION

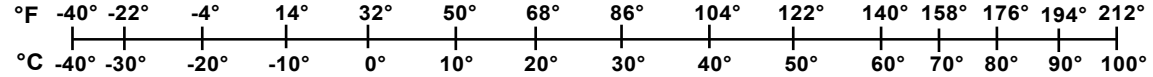

For more exact and or other conversion factors, see NIST Miscellaneous Publication 286, Units of Weights and Measures. Price $2.50 SD Catalog No. C13 10286

Updated 6/17/98

Acknowledgments

This work has been performed by University of California–San Diego (UCSD) under university research grants DTFR53-02-G-00011 (basic agreement through Amendment 9) and FR-RRD-0001-10-01-00, awarded by the Federal Railroad Administration's (FRA) Office of Research and Development, U.S. Department of Transportation. The authors are grateful to Mahmood Fateh, FRA's Technical Representative, for his technical guidance and valuable comments during all phases of this research and to Gary Carr, FRA's Chief of Track Research Division, for providing technical and logistic support during the prototype assembly and field testing. Thanks are also extended to Leith Al-Nazer from FRA, to John Choros from the John A. Volpe National Transportation Systems Center, and to Eric Sherrock and Jeff Bloom from ENSCO, Inc., for the helpful support during the field tests. BNSF Railway provided an in-kind donation of rail materials used for the construction of the UCSD Rail Defect Test Bed. Finally, the authors extend their special thanks to Mahmood Fateh for correcting this report and for suggesting several areas of improvement to this report's technical accuracy.

Contents

Illustrations

Tables

Executive Summary

This report discusses the design, development, and field testing of a prototype system for the high speed noncontact detection of rail defects in railroad tracks. The objectives of this research project are to improve the defect detection reliability and the efficiency of conventional rail defect detection methods. The results prove that the prototype detection system successfully met these objectives.

The prototype uses a pulsed laser to generate ultrasonic waves in the rail and an array of air-coupled sensors to detect the waves. The method is particularly sensitive to transverse-type defects, notoriously one of the most potentially hazardous flaws in rails. Advanced signal processing algorithms, based on real-time statistical analysis, have been developed and integrated in the prototype to maximize the signal-to-noise ratio of the defect indications and to minimize false-positive indications. The prototype was tested in the field multiple times on the Federal Railroad Administration (FRA) Hy-railer (R-4) Research Car with the support of ENSCO, Inc., FRA's technical support contractor.

This report presents numerical modeling analyses of ultrasonic guided waves propagating in rails as well as the results of seven field tests. The latest field test, conducted in June 2010, demonstrated an excellent reliability of detection of several internal rail flaws, which compared favorably to both American Railway Engineering and Maintenance-of-Way Association (AREMA) Standards and Industry Average Performance. The last portion of the report also discusses the new, 250-foot-long University of California–San Diego (UCSD)/FRA Rail Defect Test Bed constructed at UCSD's Englekirk Center Laboratories for the development of rail flaw inspection technologies.

1. Introduction

UCSD, under an FRA Office of Railroad Policy and Development grant, has developed a system for high-speed and noncontact rail defect detection. A prototype has been designed and field tested with the support of the John A. Volpe National Transportation Systems Center (Volpe Center) and ENSCO. The goal of this project is to develop a rail defect detection system that provides (a) better defect detection reliability (including internal transverse head defects under shelling and vertical split head defects) and (b) higher inspection speed than achievable by current rail inspection systems.

1.1 Current Rail Inspection Techniques

The predominant techniques utilized today for rail inspection are magnetic induction testing and ultrasonic testing. Magnetic induction exploits the perturbations in the rail magnetic field induced by the presence of geometrical discontinuities such as cracks. Contact brushes are required to induce an electric current. The disadvantages of the magnetic induction method include the contact requirement for the brushes, the elevated sensitivity to joint switches and other structural elements of the rail, and the limited inspection in terms of efficiencies.

Conventional ultrasonic testing of rails uses wheels or sleds filled with water that host an array of piezoelectric sensors. The sensors are typically operated from the top of the rail head in a pulse-echo mode with orientations at 0° (for horizontal defects) and at 70° (for transverse defects (TDs)) from the normal to the running surface. The disadvantages associated with these methods include the requirement for bulky wheels and the contact conditions, which limit inspection speed and area coverage. The contact conditions are sensitive to environmental changes (such as temperature fluctuations) that can affect the output of the test. Perhaps the most critical disadvantage is ineffectiveness in the presence of shallow horizontal cracks (shells) near the surface of the rail head. They tend to prevent the ultrasonic beams from reaching the target internal defects (IDs) with resultant limited defect detection reliability.

This limitation was the cause of train derailments in Superior, WI, in 1992 and Oneida, NY, in 2007, where severe problems were caused by hazardous material spillage. In response to these accidents and others, the National Transportation Safety Board (NTSB) recommended that the FRA conduct research for improving the effectiveness of rail inspection technologies to detect internal rail defects, particularly under shelling (NTSB, 2005). Other drawbacks of wheel-based ultrasonic rail inspections are the limited speed (typically less than 15 miles per hour (mph)) and challenges in detecting vertical split head defects also critical for rail safety.

1.2 Type of Rail Defects Targeted by the Prototype

FRA Safety Statistics Data (2008) report that train accidents caused by track failures including rail, joint bars, and anchoring resulted in 3,386 derailments and $685 million in associated damage costs during the decade 1998–2008.

The first leading cause of these accidents was the transverse fissure (TF) defect, shown in Figure 1.1, found responsible for 815 derailments and $160 million in cost during the same

time period. Another type of TD is a rolling contact fatigue (RCF) defect that typically initiates at the gage corner of the rail head. The detail fracture (DF), also shown in Figure 1, is the most common RCF defect and was responsible for 427 derailments and $137 million in associated damage cost (second highest cost) during 1998–2008 in the United States. Unfortunately, rail safety concerns will likely become more serious given the aging of the transportation infrastructure and the increasing rail tonnage.

On the basis of these statistics, the primary targets of the UCSD/FRA rail inspection prototype are TDs (TFs and DFs), including under shelling, as well as vertical split heads and compound fractures.

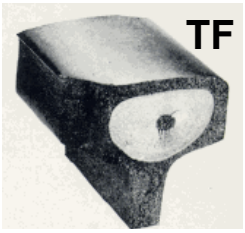

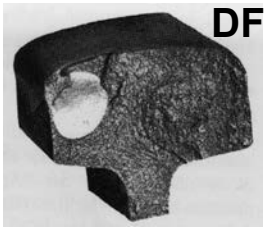

Type of Defect	% Total Defects	Direct Damage Cost	# Derailments
Transverse/ Compound Fissure	23 % (1st leading cause)	$ 160 M (highest cost)	815
Detail Fracture	12 % (2nd leading cause)	$ 137 M (2nd highest cost)	427

Figure 1.1. TF, DF, and FRA Safety Statistics Data for 1998–2008—Rail, Joint Bar, and Rail Anchoring—All U.S. Railroads

1.3 Noncontact Ultrasonic Guided Wave Approach

The method that has been developed uses ultrasonic guided waves excited by a pulsed laser and detected by an array of air-coupled sensors (Lanza di Scalea et al., 2005a, 2005b, 2006, 2007a, 2007b) (Figure 1.2). The primary advantages of this approach include 1) the increased reliability of detection, even in the presence of surface shelling; 2) the potential for extremely high testing speeds, because guided waves propagate at the speed of sound in steel (~3,000 m/s); 3) the extended rail coverage in a single test, because at present only a few feet of rail can be inspected at once; and 4) the ease of field deployment, because sensors can be positioned above the rail head as far as 2.5 inch (in) from the rail surface.

The UCSD prototype uses noncontact ultrasonic probing of the rail head, ultrasonic guided waves, and a proprietary real-time statistical analysis algorithm that maximizes the sensitivity to defects while minimizing false positives.

The ultrasonic guided modes insonify a large portion of the rail head and allow for a larger distance between the front and the rear noncontact sensors, which, in turn, increases the maximum achievable inspection speed. The prototype has been tested at speeds up to 15 mph in the field, although higher speeds are potentially possible. The maximum speed potentially achievable with the current design is on the order of 40 mph. Higher speeds would require some modifications to the hardware design.

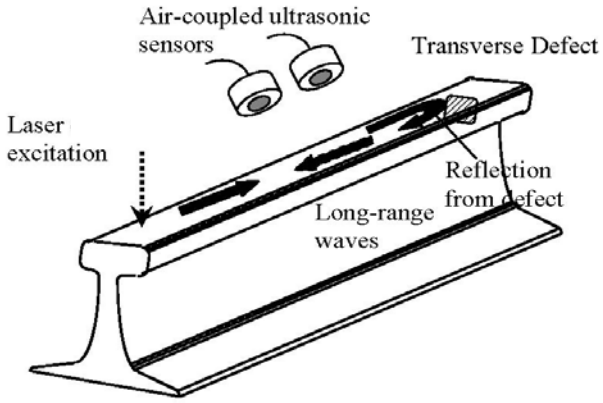

Figure 1.2. Rail Defect Detection by Ultrasonic Guided Waves Excited by a Laser and Detected by an Array of Air-Coupled Sensors

2. Numerical and Experimental Study of the Unforced and Forced Solutions of Guided Waves for Detection of Defects in the Rail Head

Various numerical and experimental studies have examined the propagation of ultrasonic guided waves in railroad tracks. This topic is of interest to the area of rail defect detection by long-range ultrasonic inspection (Lanza di Scalea et al., 2004; Rose et al., 2004; Coccia et al., 2009) as well as in the context of noise generated by passing trains (Ryue et al., 2008; Thompson, 2008). It is well known that the use of numerical methods is necessary to obtain the dispersion curves for an arbitrary cross-section waveguide like a rail over a wide range of frequencies and wavenumbers. Hesse and Cawley (2006) determined dispersion curves of guided waves for rail sections up to a frequency of 350 kilohertz (kHz), using axisymmetric finite element (FE) models.

Semianalytical FE (SAFE) methods, also referred to in the literature as spectral or waveguide FE methods, have also emerged for modeling guided waves (Rose et al., 2004; Bartoli et al., 2006; Loveday, 2009). The general SAFE approach for extracting dispersive solutions uses a FE discretization of the cross section of the waveguide alone. The displacements along the wave propagation direction are conveniently described in an analytical fashion as harmonic exponential functions. The following sections show the forced high-frequency SAFE solution for a rail head. Next, the experimental response of the rail head to a pulsed laser excitation is presented and compared with the numerical forced solution for this source. The final section discusses the sensitivity of the low-order waves to typical defects in a rail head such as surface cracks or internal TDs.

2.1 Unforced and Forced Solutions of Guided Waves in a Rail Head

The SAFE model is applied to the head of a 115-pound (lb) American Railway Engineering and Maintenance-of-Way (AREMA) rail, the cross section of which is shown in Figure 2.1 along with the FE mesh of the head. The wave propagates along the x direction, with wavenumber ξ and frequency ω.

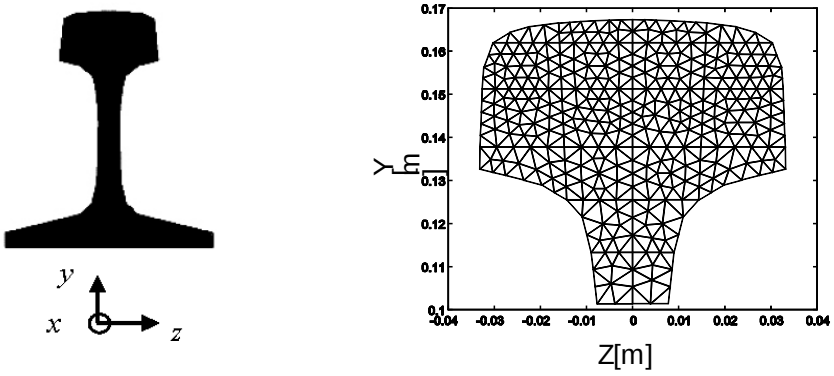

Figure 2.1. Cross Section of 115-Pound AREMA Rail and FE Mesh of the Rail Head

The arbitrary cross section lies in the *y*-*z* plane. The constitutive relations at a point are given by

$$\boldsymbol{\sigma} = \tilde{\mathbf{C}}\boldsymbol{\varepsilon} \tag{1}$$

where $\boldsymbol{\sigma}$ and $\boldsymbol{\varepsilon}$ are, respectively, the harmonic stress and strain fields, and $\tilde{\mathbf{C}}$ is the constitutive matrix, generally complex (Hayashi et al., 2003). The equations of motion for the cross section are formulated by inserting the kinetic and potential energies into Hamilton's equation. The discretized version of the Hamiltonian leads to the final expression for the wave equation as (Hayashi et al., 2003):

$$\left[\mathbf{A} - \xi\mathbf{B}\right]_{2M}\ \mathbf{Q} = \mathbf{0} \tag{2}$$

where **Q** represents the displacement vector, and the frequency-dependent matrices **A** and **B** are derived from the mass and stiffness matrices of the waveguide discretized model. Solving equation 2 at each frequency ω, 2M eigenvalues ξ_m, and consequently, 2M eigenvectors are obtained. The eigenvalues correspond to the waves' wavenumbers, and the eigenvectors represent the M forward and the corresponding M backward vibrational mode shapes of the rail cross section. In general, the eigenvalues are pairs of complex conjugate numbers ($\pm \xi_{Re} \pm i\xi_{Im}$). For each wave, the phase velocity can be evaluated by $c_{ph}=\omega/\xi_{Re}$ and its attenuation, in Nepers per meter, by ξ_{Im}; the energy velocity can be calculated as defined by Castaings and Hosten (2003). The rail considered had the following properties: density ρ = 7,932 kg/m^3, longitudinal bulk wave velocity c_L = 5,960 m/s, shear bulk wave velocity c_T = 3,260 m/s, longitudinal and shear bulk wave attenuation coefficients, respectively, κ_L = 0.003 Np/wavelength, and κ_T = 0.008 Np/wavelength. The rail cross section had a complex geometry with one vertical axis of symmetry. The mesh used 351 nodes for 632 triangular elements with linear interpolation displacement functions (Figure 2.1). Only the rail head and the upper part of the web were modeled, because experimental measurements showed that the loading considered in this context will induce low or no energy in the foot. The results are shown first for a frequency range up to 50 kHz. Phase velocity and energy velocities dispersion curves are plotted in Figures 2.2(a) and 2.2(b), respectively.

The eight lowest-order modes were labeled according to their waveshape symmetry (S_n) or antisymmetry (A_n) with respect to the *y*-axis. The unforced results for the entire cross section have been published elsewhere (Hayashi et al., 2003; Bartoli et al., 2005; Hesse and Cawley, 2006) in which a larger number of modes were present in the same frequency range because of a larger section of the waveguide. The plots of the phase and group velocities up to 500 kHz are also shown, respectively, in Figures 2.3 and 2.4. The plotted curves reveal the complexity of the propagation scenario at these frequencies.

a)

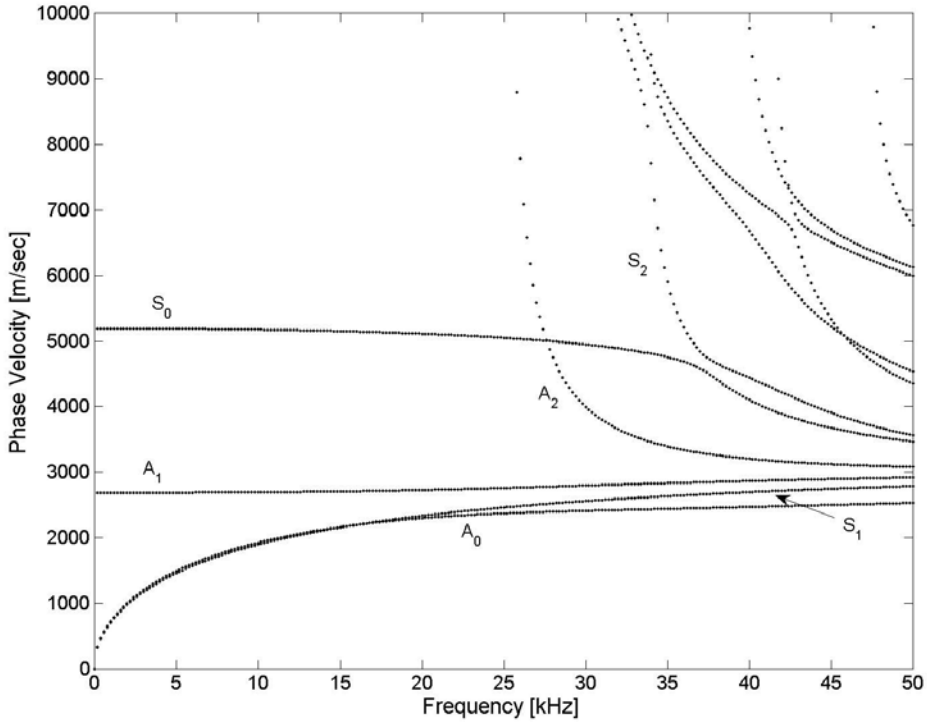

b)

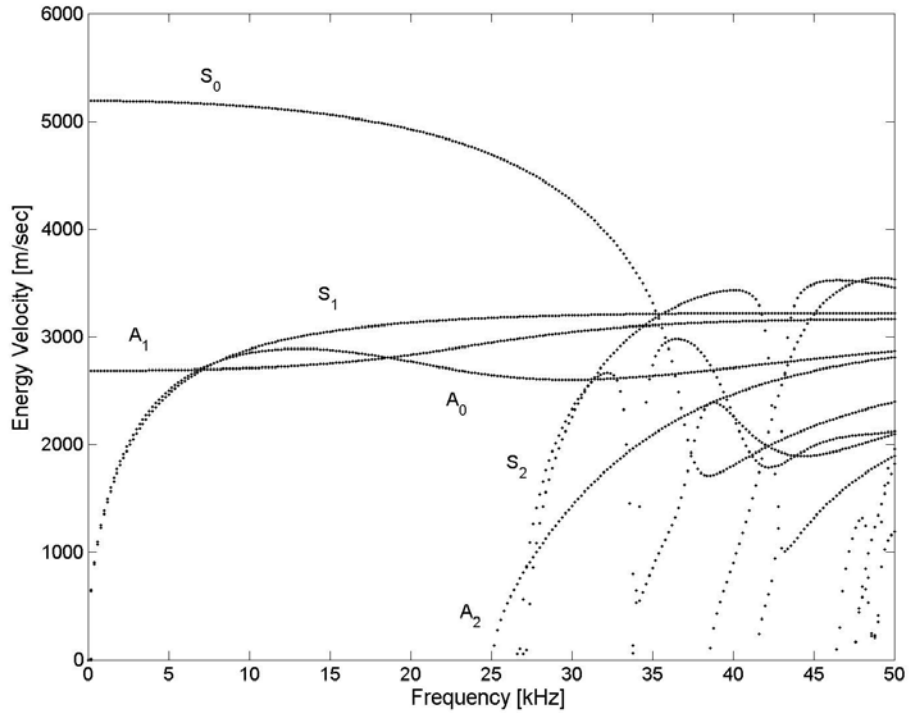

Figure 2.2. Phase Velocity (a) and Energy Velocity (b) Dispersion Curves

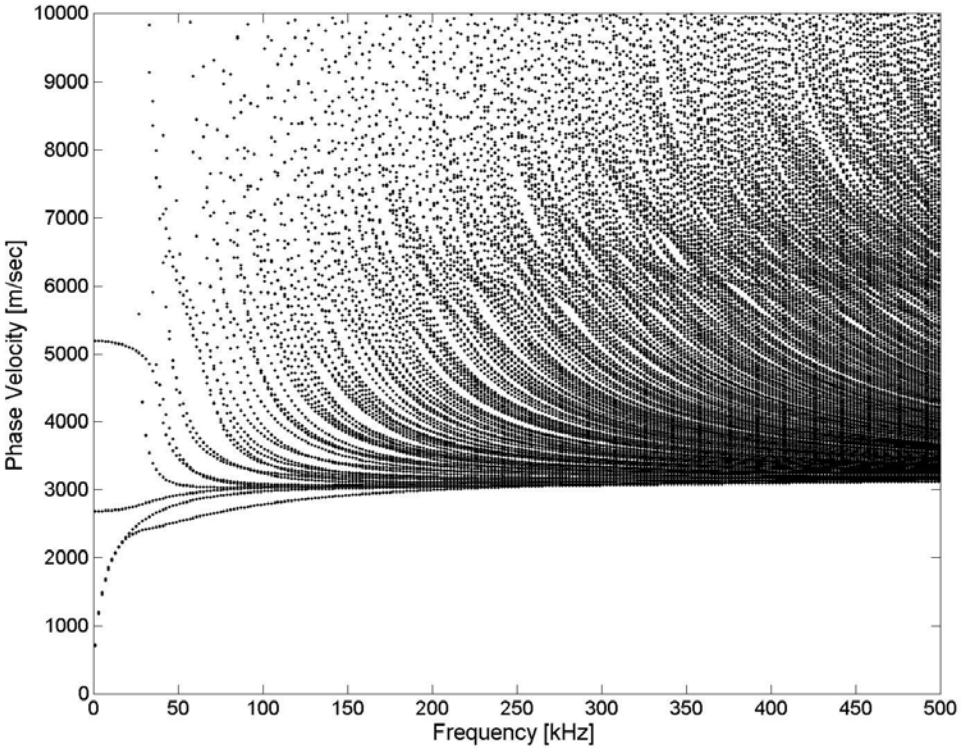

Figure 2.3. Phase Velocity Dispersion Curves of 115-Pound AREMA Rail Head

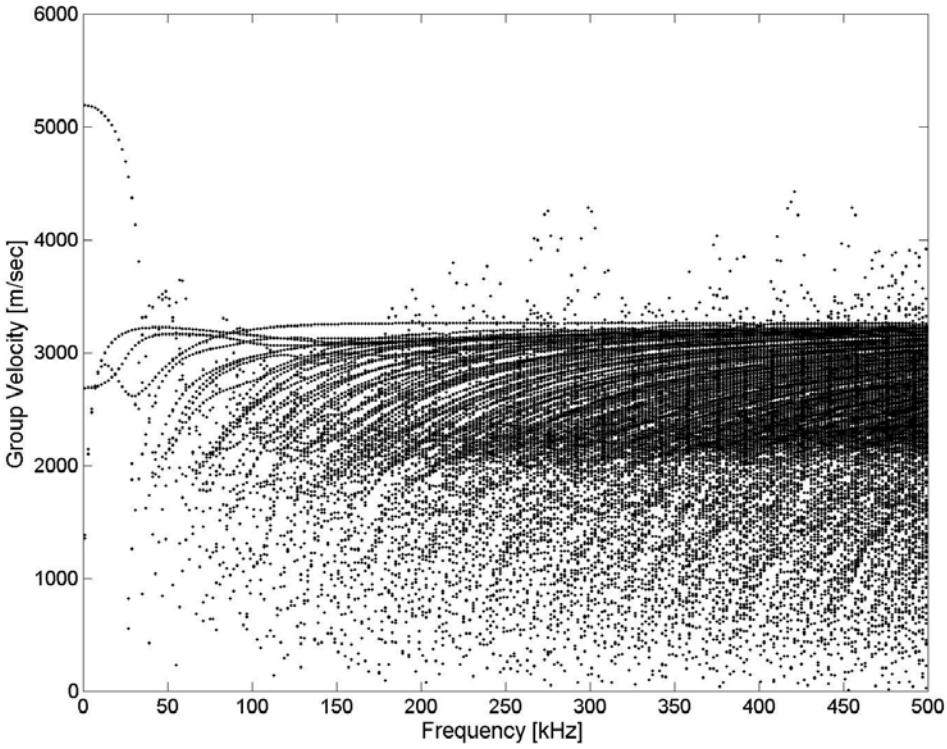

Figure 2.4. Group Velocity Dispersion Curves of 115-Pound AREMA Rail Head

To study the forced solution, the contribution of the potential of a harmonic external load has to be added to the Hamiltonian of the waveguide (Rose, 1999).

Following the algebra from Hayashi et al. (2003), the forced solution can be obtained by solving the following system:

$$\left[\mathbf{A} - \xi \mathbf{B}\right]_{2M} \mathbf{Q} = \hat{\mathbf{p}} \tag{3}$$

$\hat{\mathbf{p}}$ being the forcing term. The solution of equation 3 can be expressed as a linear combination of the right and left eigenvectors $\mathbf{\Phi}_m^{\mathbf{R}}$ and $\mathbf{\Phi}_m^{\mathbf{L}}$, respectively :

$$\mathbf{Q} = \sum_{m=1}^{2M} Q_m \mathbf{\Phi}_m^{\mathbf{R}} \tag{4}$$

where

$$Q_m = - \frac{\mathbf{\Phi}_m^{\mathbf{L}} \hat{\mathbf{p}}}{(x - x_m) B_m} \quad , \qquad B_m = \mathbf{\Phi}_m^{\mathbf{L}} \mathbf{B} \mathbf{\Phi}_m^{\mathbf{R}} \tag{5}$$

The displacements at $x > x_s$ can be defined by the following expression (Rose, 1999):

$$Q(x, y, z, t) = \frac{1}{2\pi} \int_{-\infty}^{+\infty} \sum_{m=1}^{M} -\alpha_m \mathbf{\Phi}_m^{\mathbf{R}up} e^{i[\xi_m (x - x_s)]} e^{i\omega t} d\omega \tag{6}$$

where $\mathbf{\Phi}_m^{\mathbf{R}up}$ is the upper part of $\mathbf{\Phi}_m^{\mathbf{R}}$, and α_m is the modal participation factors of the M forward propagating modes, defined as:

$$\alpha_m = -\frac{\mathbf{\Phi}_m^{\mathbf{L}} \hat{\mathbf{p}}}{B_m} \tag{7}$$

and x_s is the position of the excitation. If $x < x_s$, the included modes need to be replaced by the M backward-propagating ones. The vector $\hat{\mathbf{p}} = \hat{\mathbf{p}}(x_s, y, z, \omega)$ contains the spectral amplitudes of the applied nodal loads.

2.2 Response of the Rail Head to a Pulsed Laser Excitation

The forced response theory was applied to the 115-pound AREMA rail previously studied, and the same mesh was considered for the cross section. The applied load was chosen to simulate the effect of a pulsed laser generator with a 1-microsecond pulse duration. A focused optical element was used to deliver the laser pulse on the top of the rail head.

The frequency and time domain nodal responses of any section at arbitrary distance *x* along the propagation direction were obtained from the normal solutions of equation 6. The response of a node on the top of the rail head, in a cross section located at 4 in (~102 millimeters (mm)) from the load source was calculated. The numerical forced solution was then compared with measurements. An air-coupled transducer was positioned on the rail at 4 in from the excitation, which was provided by a rail-head–wide pulsed laser line; the air-coupled lift-off was approximately 1.5 in (~38 mm). The sensor used was a broadband, capacitive air-coupled transducer (40 kHz to 2.25 megahertz (MHz)). The excitation was provided by a Q-Switched laser generator at 300 megajoules and a 30-hertz repetition rate. The experimental signal was high-pass-filtered at 40 kHz in the amplification stage, and a experimental and numerical results were compared in the time and frequency domains. No

averaging was used in the measurements. The displacements along the *y* direction have been compared in Figure 2.5(a), after appropriately delaying the experimental response to account for the travel time in air. The SAFE-predicted response is consistent with the measurements: the first arrival is reproduced, whereas the scattered peaks that follow are caused by other phenomena such as multiple reflections within the rail section that are not captured by the analysis. Another source of the discrepancy is that the sensor's angle effectively filters selected phase values (Rose, 1999). Figure 2.5(b) shows the comparison between simulated and experimental responses in the frequency domain. The frequency content shows a similar trend in both cases. The simulated response contains two outlier peaks at approximately 30 and 40 kHz, corresponding to cutoff frequencies of two lower-order propagating modes. In the undamped SAFE model, in fact, it is known that modes may have a resonance-type behavior in proximity of the cutoff frequency, showing an erroneously large amount of energy.

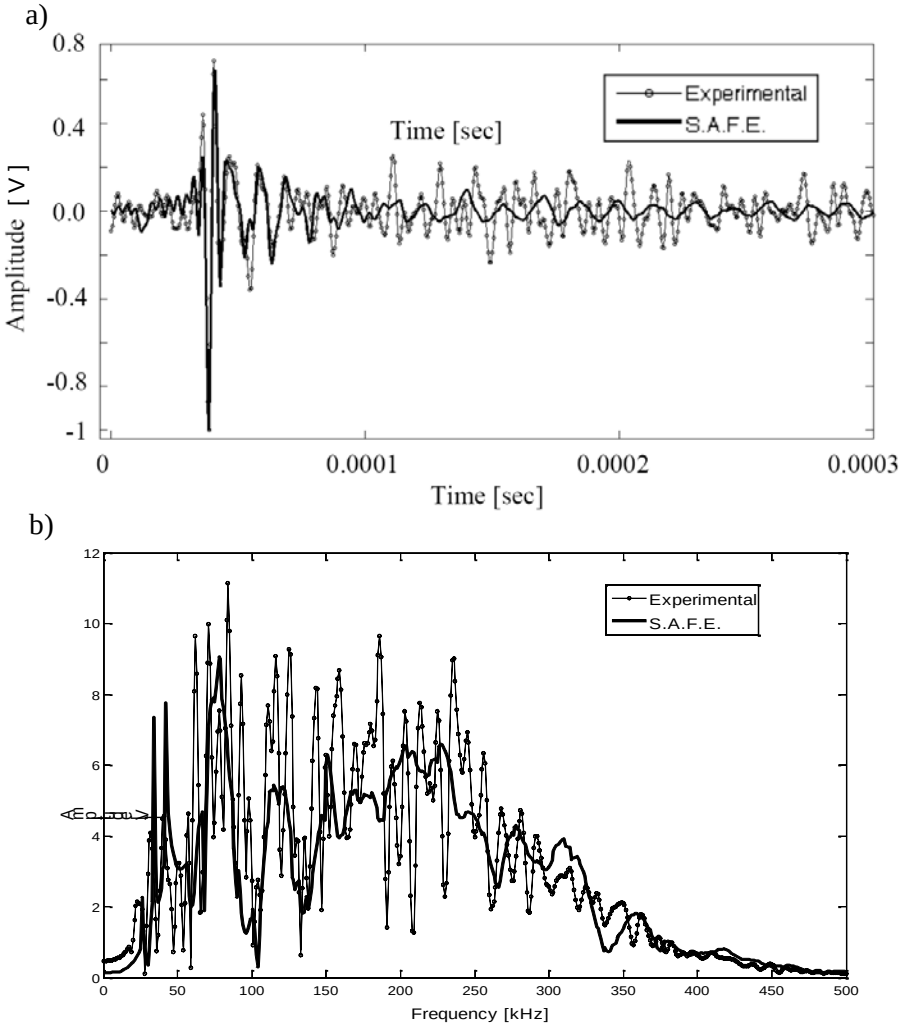

Figure 2.5. Comparison between Experimental and SAFE Results of Forced Response of the Rail Displacements along the *y* Direction in the Time Domain (a) and Spectral Domain (b)

This drawback does not appear in SAFE responses calculated by modeling the waveguide as a damped structure and considering appropriate attenuation thresholds. In the unforced case, damping was not considered for computational reasons; in fact, to ideally reconstruct the response, a large number of frequencies needs to be considered in the inverse Fast Fourier Transform.

2.3 In-Plane Strain Energy in the Rail Head

Critical to the selection of ultrasonic guided modes for defect detection is the distribution of strain energy in the rail cross section. Because the most critical defects are usually located in the rail head, it is important to excite modes whose energy concentrates there. This process requires several steps. Initially, a mode-tracking algorithm needs to be applied to isolate each propagating mode (Loveday, 2009) so that the forced response process can be launched separately for each mode. Plotting the cross-sectional strain energy will then provide a description of the different rail defect-sensitive areas for each of the considered modes. Once the strain energy calculation is limited to the in-plane strain (*y*-*z*), the expression of the *e-th* element energy is the following:

$$\frac{1}{4}\hat{\boldsymbol{\varepsilon}}^{(e)\mathrm{T}}\hat{\mathbf{C}}_e\,\hat{\boldsymbol{\varepsilon}}^{(e)} \tag{8}$$

where $\hat{\boldsymbol{\varepsilon}}^{(e)}$ and $\hat{\mathbf{C}}_e$ represent, respectively, the expressions of element strain and constitutive matrix, reduced to the in-plane coordinates *y* and *z*. The reduced strain reads:

$$\hat{\boldsymbol{\varepsilon}}^{(e)} = \begin{bmatrix} \varepsilon_y \\ \varepsilon_z \\ \gamma_{yz} \end{bmatrix}^{(e)} = \frac{1}{2A^{(e)}} \begin{bmatrix} z_k - z_j & 0 & z_i - z_k & 0 & z_j - z_i & 0 \\ 0 & y_j - y_k & 0 & y_k - y_i & 0 & y_i - y_j \\ y_j - y_k & z_k - z_j & y_k - y_i & z_i - z_k & y_i - y_j & z_j - z_i \end{bmatrix}^{(e)} \begin{bmatrix} u_i \\ v_i \\ u_j \\ v_j \\ u_k \\ v_k \end{bmatrix}^{(e)} \tag{9}$$

where $(y,z)_{(i,j,k)}$, $(u,v)_{(i,j,k)}$ are, respectively, the in-plane coordinates and displacements of the *i*-th , *j*-th, and *k*-th nodes; $A^{(e)}$ is the area of the *e-th* triangular element. Figure 2.6 shows four low-order propagating modes, along with their modeshapes and in-plane cross-sectional strain energy distributions, calculated at certain frequencies.

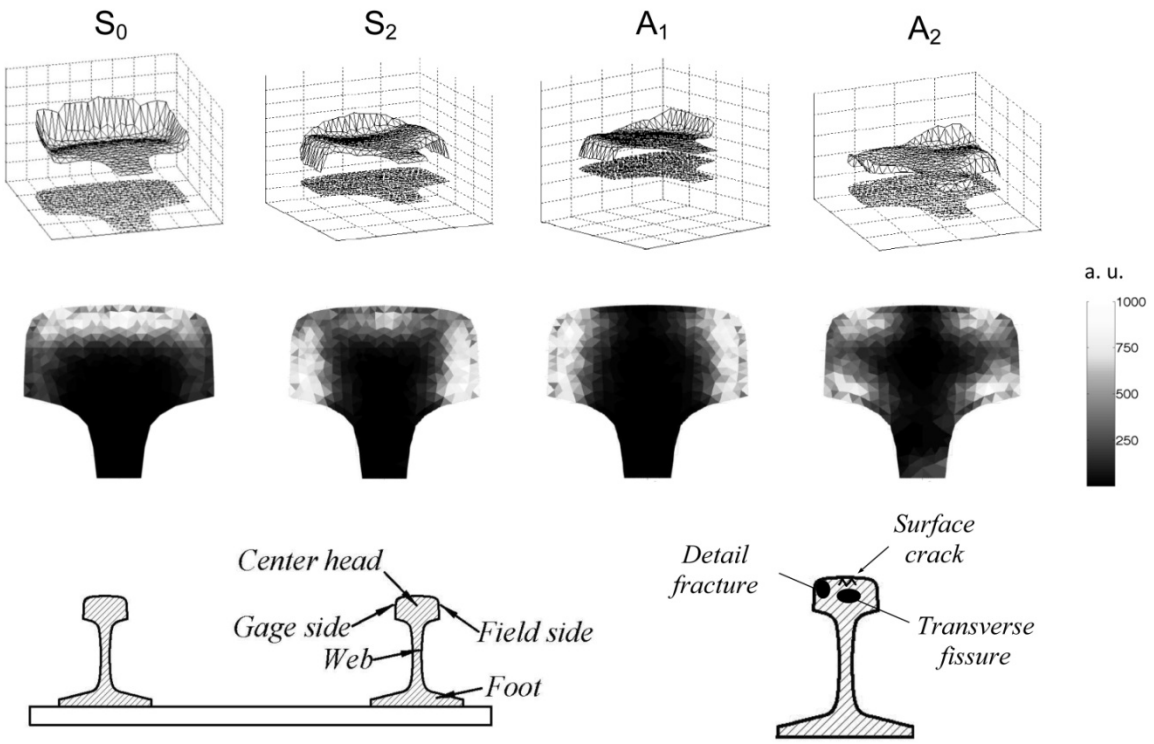

Figure 2.6. Modeshapes and Strain Energy Distributions of Modes S_0, S_2, A_1, and A_2 Computed at Specific Frequencies; at the Bottom, Different Areas of a Common Rail Section with Typical Rail-Head Defects

2.4 Mode Selection for Defect Detection

The energy plots of Figure 2.6 show that mode S_0 is a good candidate for the detection of surface cracks, chips, or shallow IDs, located anywhere within the width of the rail head. Modes S_2 and A_1 are good probes for surface cracks, chips, or shallow IDs located, respectively, in the center and in the gage/field sides of the rail head; both modes also induce energy deeper in the gage and field sides of the head and are hence sensitive to deep IDs; they are well suited for detection of DFs and TFs. Mode A_2 focuses its energy at the corners of the gage and field sides of the rail head. Modes A_0 and S_1, not included in the plots, are unsuitable to rail-head inspection, because they carry energy along the rail web; as it will be shown later, those modes are almost unexcited by the laser load, acting on the top of the head. Once the strain energy distribution for each mode is analyzed, it can be deduced that modes S_0 and A_1, respectively, are the best suited for surface and ID detection. This analysis also leads to the conclusion that an antisymmetrical excitation would be needed to inspect both the gage and field sides of the rail head for IDs, whereas a symmetric excitation should be preferred to detect surface flaws.

2.5 Influence of the Loading Pattern on the Mode Excitability

Symmetric and nonsymmetric excitation patterns were applied to the SAFE model of the rail (Figure 2.7). The load amplitude was adjusted so that, in both cases, the same amount of energy was transferred to the rail. The influence of a different pattern excitation on the response of the rail was analyzed by plotting the mode excitability curves, which are modal participation factor functions of the frequency. With increasing frequency, the complexity of the modes is clear; 152 forward-propagating modes are found at 500 kHz. When the excitability plots are studied, it is evident that few lowest-order modes are dominant in most of the spectrum. A focused analysis of four low-order mode excitabilities is performed here to determine the influence of the loading pattern on the response.

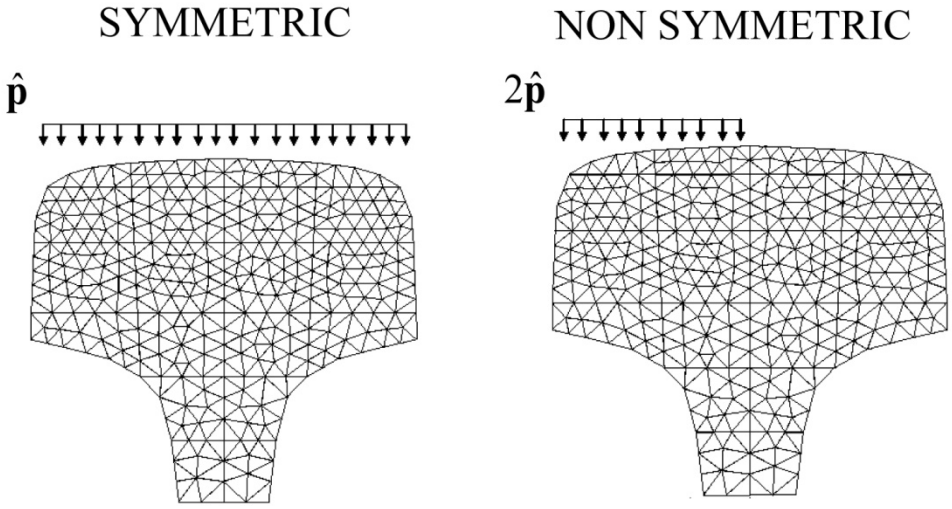

Figure 2.7. Symmetric and Nonsymmetric Excitation Patterns on the Meshed Rail Section

Figure 2.8 shows the excitability of S_0, A_0, A_1, and S_2 modes for the two load cases (symmetric and nonsymmetric excitations). In the following discussion, the nonsymmetric load was considered as the sum of a symmetric and an antisymmetric pattern. In both loading cases, mode S_0 is the most effective in terms of excitation across the spectrum; this is because its modeshape has maximum displacements in the area where the load is applied. In the nonsymmetric load case, mode A_1 is excited as well, because of the antisymmetric contribution of the load. It is clear from the plots that symmetric load patterns transmit most of the energy to symmetric modes; in nonsymmetric cases, instead, symmetric and antisymmetric modes are both excited. Mode A_0 is never excited, because it transfers energy mainly through the rail web, whereas mode S_2 shows medium excitability for the symmetric case.

Including all the propagating modes up to 500 kHz, the rail response was obtained for the two excitation patterns. When several modes are excited, modulation between them can be experienced (Hesse and Cawley, 2006), meaning that the received amplitude can be position dependent as a result of the different energy velocities. Because of this factor, the forced

response was calculated at different distances from the source (2 and 4 in) for both the symmetric and nonsymmetric load cases. As shown in Figure 2.9, the distribution of the in-plane strain energy along the cross section is slightly different, but it still reflects the symmetry (or nonsymmetry) of the load.

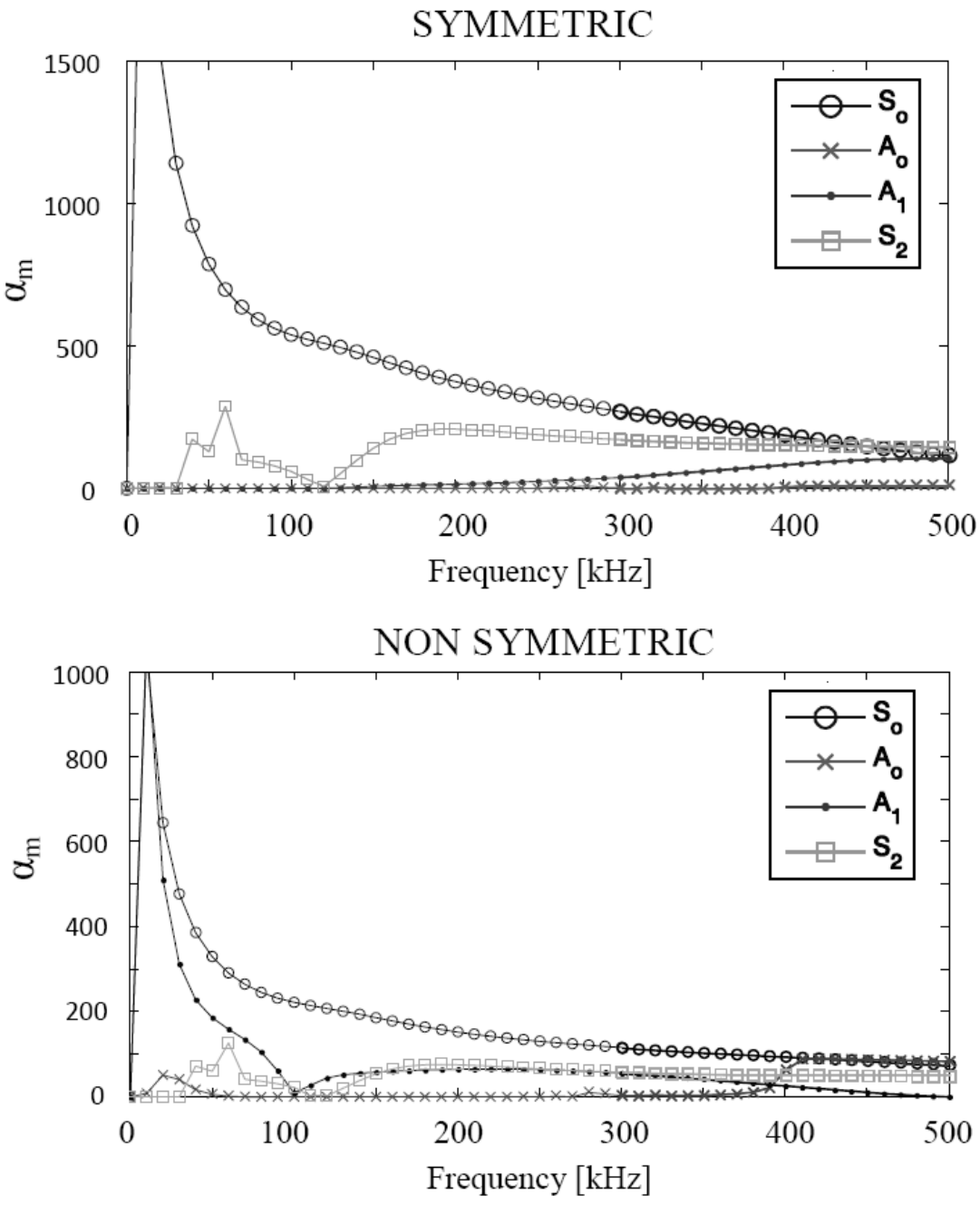

Figure 2.8. S_0, A_0, A_1, and S_2 Mode Excitability Curves for a Symmetric and a Nonsymmetric Excitation of the Rail Head

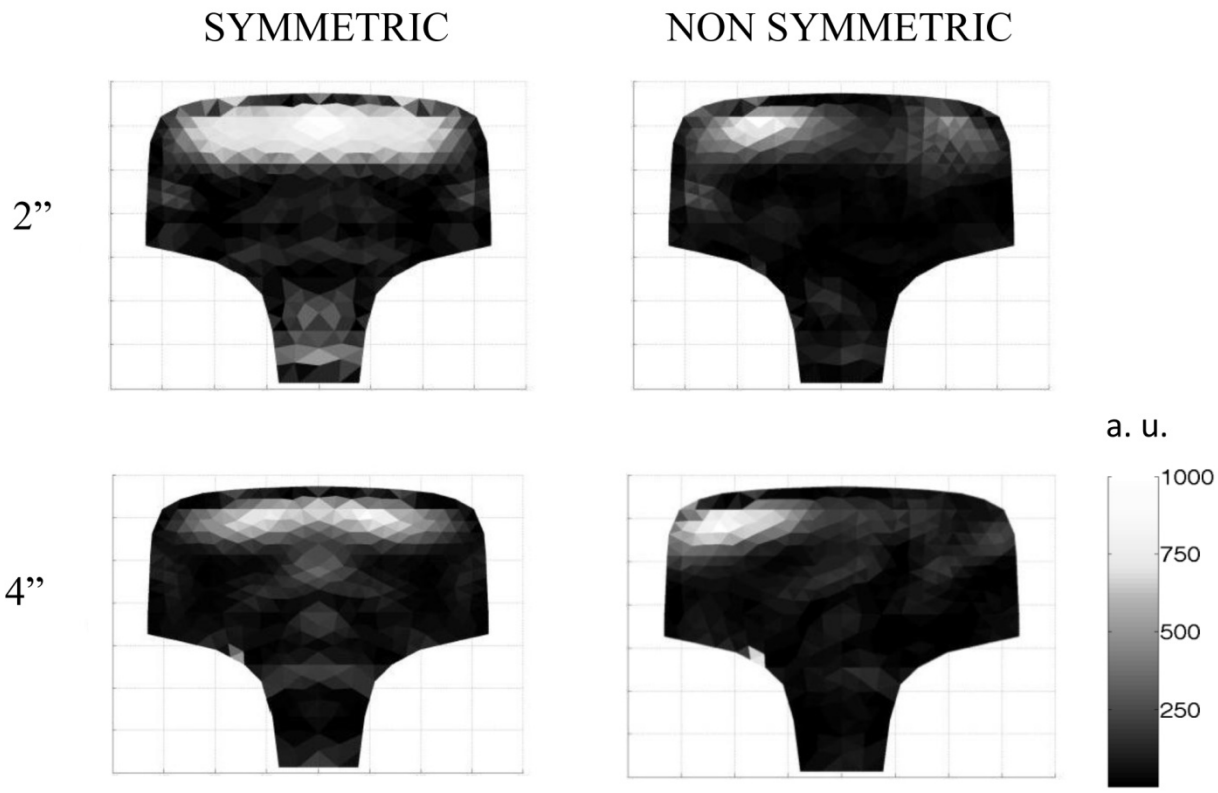

Figure 2.9. In-Plane Cross-Sectional Strain Energy Distributions for a Symmetric and a Nonsymmetric Excitation (2 and 4 in from the source)

Note: ***a.u.*** is “arbitrary units,” meaning to within an arbitrary multiplication constant.

2.6 Effect of Frequency Content on the Guided Wave Penetration Depth

A mode *j* propagating with phase velocity c_{ph}^{j} at the circular frequency ω_k will develop a penetration depth of the order of its wavelength λ_j.

The mode wavelength can be expressed as the ratio of phase velocity and frequency:

$$\lambda_j = \frac{c_{ph}^{j}}{f_k} \tag{10}$$

Assuming that only the lowest-order modes are contributing to the response, because they carry the highest amount of energy, and considering that for frequencies higher than 100 kHz those modes have already converged to the Rayleigh wave velocity (c_{ph} = 2,900 meters per second for steel), it can be expected that for high frequency the penetration depth of the modeled guided waves in the rail is inversely dependent on the frequency. A similar result was obtained by Hesse and Cawley (2006). The plot of the cross-sectional in-plane strain energy obtained by the SAFE model for the case of symmetric pattern excitation at different frequency ranges confirmed the above consideration. As shown in Figure 2.10, the in-plane cross-sectional strain energy computed from the rail response, after applying a third-order Butterworth high-pass filter (high-frequency range), is confined to a surface depth of

approximately 10 mm; instead, the in-plane cross-sectional strain energy of the response after applying another third-order Butterworth band-pass filter (low-frequency range) is distributed in the rail head up to a depth of 25 mm. Other authors proved that high frequencies guided waves (above 100 kHz) were highly sensitive to surface damage such as rail shelling, whereas lower frequencies were unaffected (Lee et al., 2009).

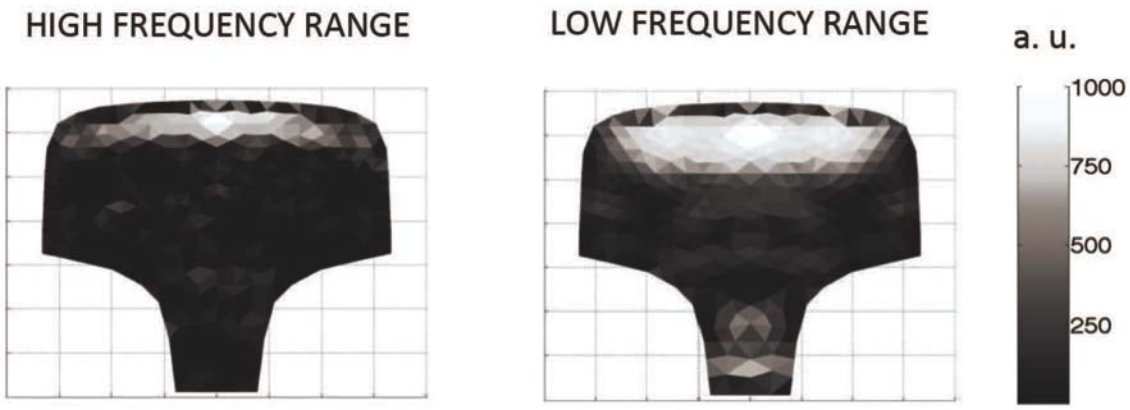

Figure 2.10. In-Plane Cross-Sectional Strain Energy Distributions for a Symmetric Excitation, Obtained by Filtering the Response with a Third-Order Butterworth High-Pass Filter (high-frequency range) and a Third-Order Butterworth Band-Pass Filter (low-frequency range)

Note: A.U. is "arbitrary units," meaning to within an arbitrary multiplication constant.

2.7 Conclusions of the Numerical and Experimental Study

The unforced and forced solutions of guided waves in rails were obtained with the SAFE method and validated by experimental results. Damping was included in the model for the unforced response solution; however, because of its high computational demand, it was neglected in the forced response case. A reasonably good match between theoretical and experimental results was shown in terms of time and frequency domains of the rail response to a broadband excitation on the rail head.

A symmetric excitation pattern on the top of the rail develops symmetric cross-sectional strain energy, with maxima close to the top of the head: A nonsymmetric pattern, instead, generates energy at the sides of the head. The analysis of modeshapes and in-plane cross-sectional strain energy can help in choosing certain modes for specific defects. Among the lowest-order modes, S_0 was shown to be effective for surface defect detection anywhere within the width of the rail head, whereas A_1 and A_2 proved to penetrate deeper, being more suitable for the detection of internal rail flaws. Mode S_2, instead, showed potential for both surface and ID detection.

3. Prototype Development

3.1 Defect Detection Scheme

Before the first field tests, a number of laboratory tests were conducted on 115-pound AREMA rail sections donated by the San Diego Trolley with simulated surface defects of increasing depths. Two 139-pound sections with internal TDs were also tested.

The scheme that was found most effective was based on "transmission," rather than "reflection," measurements. In the "transmission mode," a defect is detected by monitoring the attenuation of the ultrasonic wave as it travels past the flaw. In its simplest implementation, two air-coupled sensors must be used as shown in Figure 3.1. In the prototype, a damage index (D.I.) is calculated in real time as the ratio between certain features of the signal detected by the sensor closer to the laser source, *Fsens1*, over the same features from the sensor further from the laser source, *Fsens2*

$$\text{D.I.} = \frac{F_{sens1}}{F_{sens2}} \tag{11}$$

If a defect is located in the section of rail between the two sensors, *Fsens2* will be smaller than *Fsens1*, and the D.I. will increase compared with its normal, defect-free value (nominally one). The D.I. in eq. 11 is also expected to grow with increasing defect size or percent head area (% H.A.) reduction.

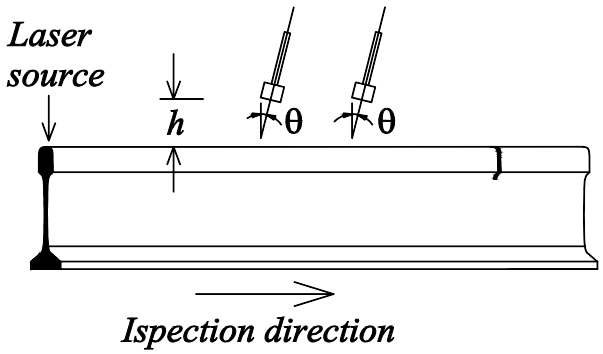

Figure 3.1. Defect Detection Scheme in "Transmission Mode" with a Pair of Air-Coupled Sensors

The first field testing of the prototype was conducted with the FRA equipment and technical support of ENSCO, FRA's technical support contractor. ENSCO's support consisted of the design and construction of a cart hosting the prototype elements, the use of the FRA's hy-railer with positioning system, and the coordination with the owners of the test bed on a siding of the Gettysburg and Northern Railroad (GET), near Gettysburg, PA, in March 2006, in April 2007, and subsequently in March 2008.

3.2 The Prototype: Hardware and Software

The prototype had to be well isolated from vibrations, had to guarantee a constant lift-off distance between the air-coupled sensors and the rail head (~2.5 in), and had to keep at minimum the relative displacement between the laser head and the optical lenses used to

focus the light onto the rail surface. The cart housed the laser head vertically and held four air-coupled sensors with their preamplifiers. Ruggedness, low source power requirements, and vertical mounting capability of the laser head are the main features of the chosen laser generator. A sequence of two optical elements was used to route the light emission from the laser port to the rail head. The first element was a planoconcave lens that transforms a collimated light beam into a divergent beam. The second element was a cylindrical lens that focuses the diverged light into a line perpendicular to the rail running direction. Broadband air-coupled sensors were chosen to acquire the ultrasonic signals traveling along the rail. Ruggedness and large bandwidth are the dominant features of the chosen air-coupled sensors.

The unit control and data acquisition unit chosen for the prototype was a National Instruments (NI) PXI chassis running under LabVIEW©. The hardware layout is described in Figure 2.2. A laptop was used in conjunction with the PXI unit to form a client-server Ethernet-linked platform.

The server (the PXI unit) controls the laser operation and the acquisition, processing and display of the measurements by the air-coupled sensors. Data from the proprietary onboard positioning system installed on the FRA hy-railer was constantly acquired by the server. From the serial port (RS-232) the server is able to trigger the laser to start the data acquisition.

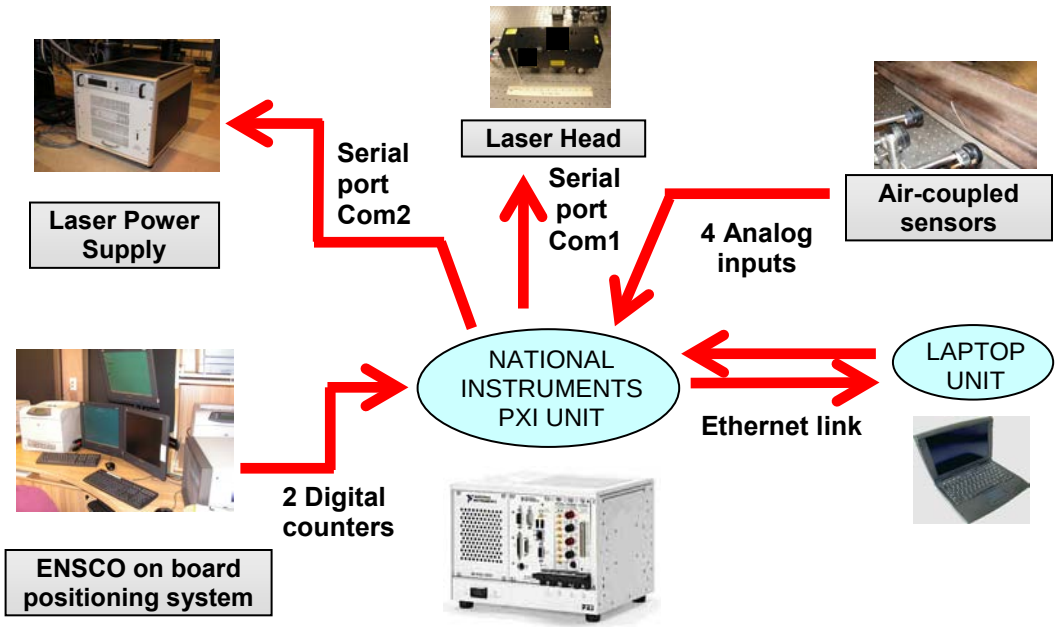

Figure 3.2. Hardware Layout of the Rail Defect Detection Prototype

The ultrasonic signals detected by the air-coupled sensors are digitized through the analog input boards, processed, and logged into the server. On the client end (laptop), the user is able to start and stop the acquisition, adjust the laser power, change the firing frequency, modify the ultrasonic and signal processing settings, monitor the results in real time, and display a report window.

3.3 The Prototype: User Interface and Operational Tasks

Figure 3.3 shows a snapshot of the software user interface. Box 1 controls the firing frequency (i.e., the number of laser shots per second). The maximum frequency is 30 Hz, and it is limited by the laser power supply. From Box 2, the user can select the laser power output; 100 percent laser power means a laser beam of maximum power with a duration of approximately 20 nanoseconds. The laser status is constantly monitored in box 3 through a series of indicators that are the response to a query that is periodically sent through the serial port Com 2. Box 4 allows opening/closing the laser head shutter and starting/stopping firing. Box 5 allows starting either the calibration task or the testing task (see below); the latter can only be activated once "Shutter" is in the "Open" position, and the "FIRE" button is on the "Fire ON" position. In addition, Box 5 contains three leds associated with the PXI (server) status.

The "CALIBRATION" button in Box 5 opens the calibration window, shown in Figure 3.4. Box 6 displays both the raw ultrasonic measurements from a pair of air-coupled sensors and the de-noised signals after processing. The D.I. is also plotted as a function of position.

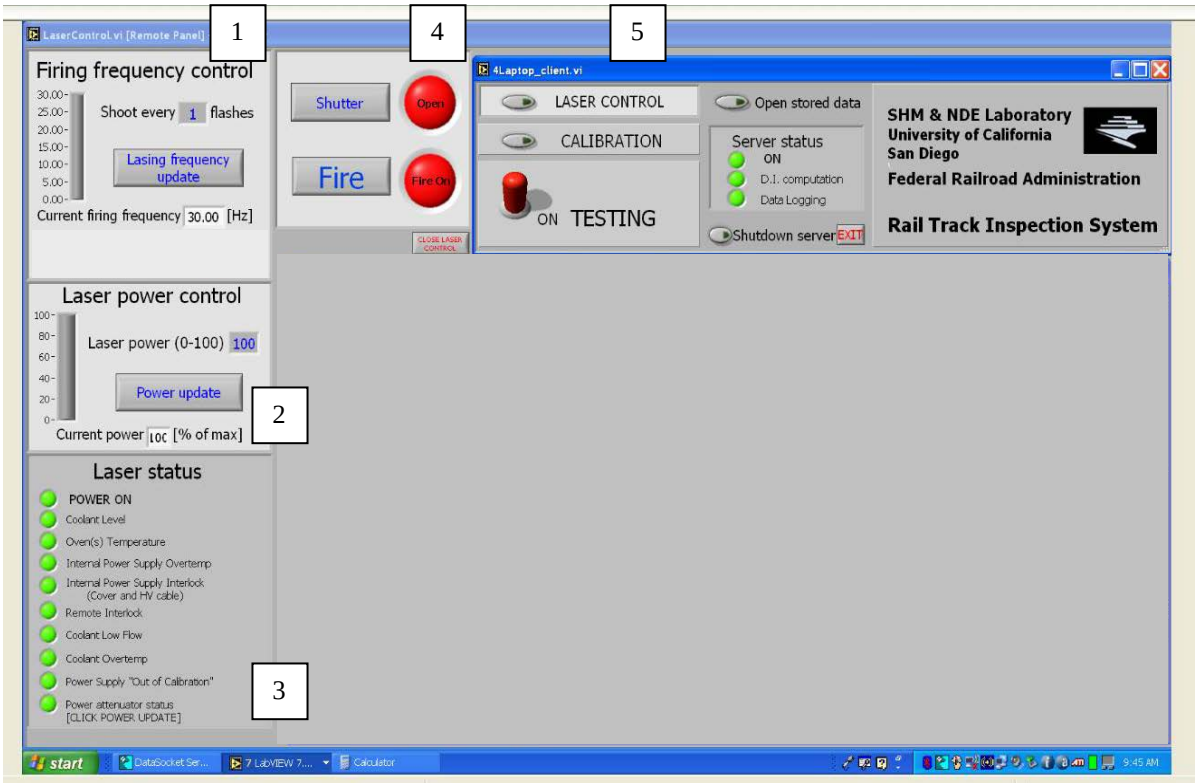

Figure 3.3. Snapshot of the LaserControl.vi That Controls the Laser and Allows Opening of the Calibration Task and the Testing Task

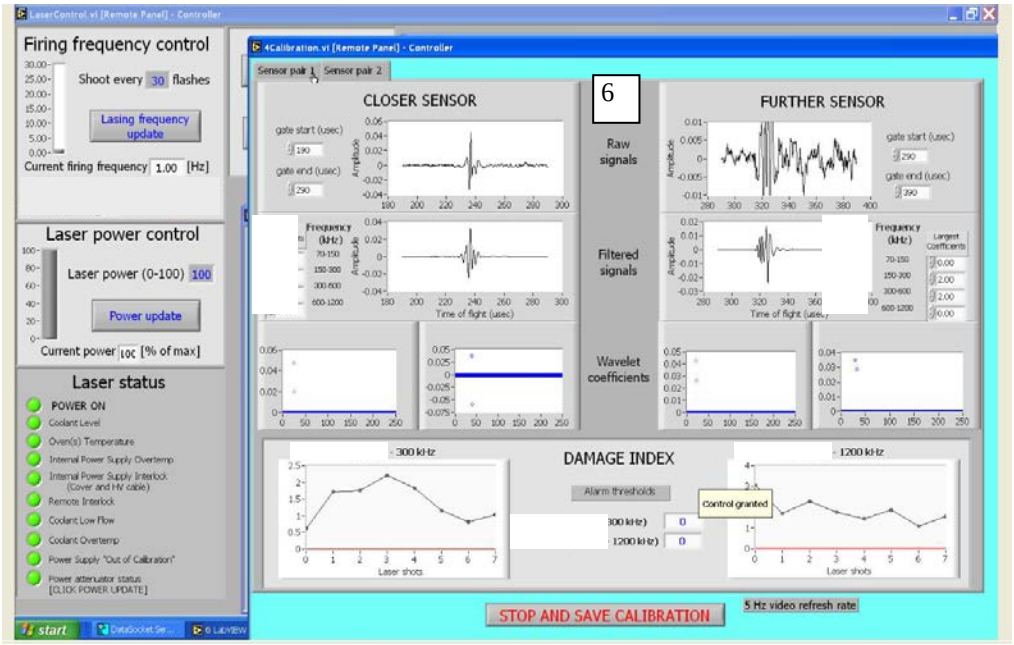

Figure 3.4. Snapshot of the 4Calibration.vi for the Calibration Task; the LaserControl.vi Is Still Visible in the Background

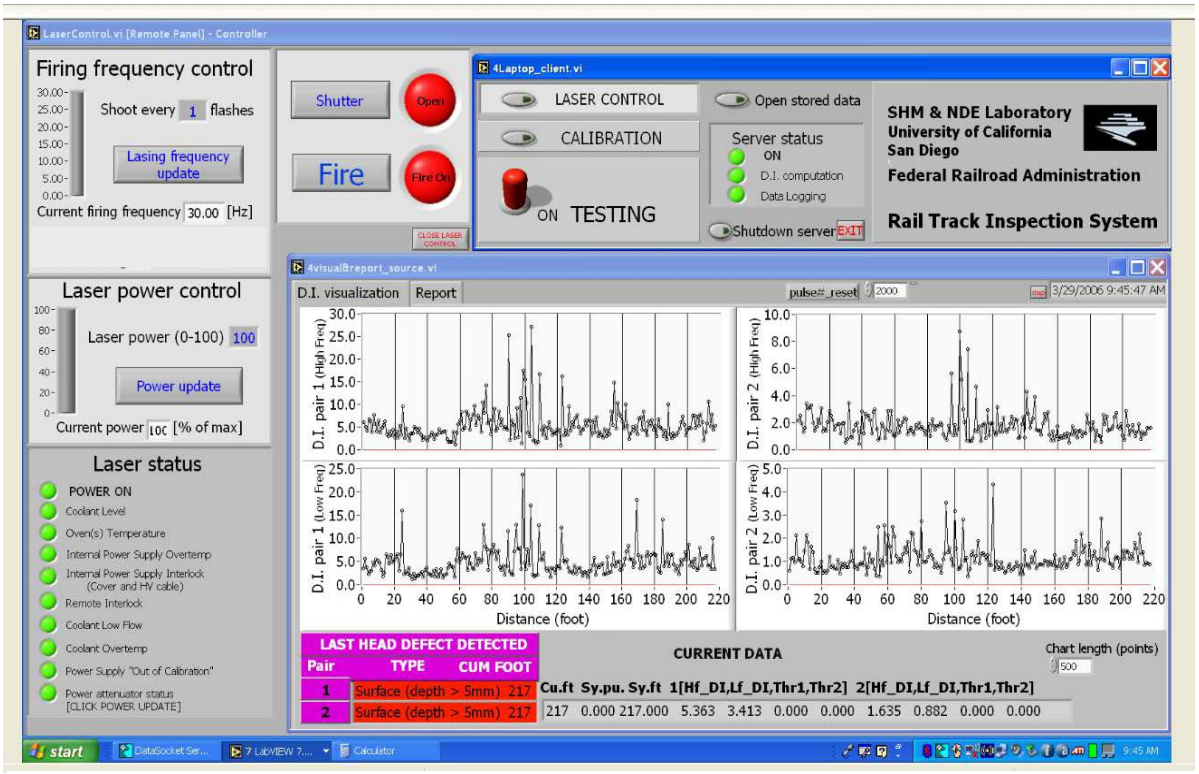

Figure 3.5. Snapshot of the 4visula&report.vi When the Testing Task Is Activated; the LaserControl.vi Is Still Visible in the Background

Shown in Figure 3.4, the D.I. is calculated in two frequency bandwidths to discriminate small surface defects (<8% H.A. reduction) from large surface defects (>8% H.A. reduction) and IDs. The D.I. associated with higher frequencies is hereafter indicated as H.F.-D.I. The D.I. associated to lower frequencies is hereafter indicated as L.F.-D.I.

Once the calibration phase is completed, the user saves the settings and closes the calibration window by clicking the button "STOP AND SAVE CALIBRATION." The front panel appears again as in Figure 3.3. Now the operator is ready to start the inspection by switching the "TESTING" command to the "ON" position. The front panel will appear as in Figure 3.5.

The testing window shows two tabs: D.I. visualization in real-time and Report. The D.I. visualization tab displays, in real-time, four plots (two plots per sensor pair) of the D.I. as a function of the track position (foot). Starting from top left and going clockwise, the window displays the H.F.-D.I. of sensor pair 1, the H.F.-D.I. of sensor pair 2, the L.F.-D.I. of sensor pair 2, and the L.F.-D.I. of sensor pair 1. The window also includes the "Chart length (points)" control to select the desired length of the plots, the "CURRENT DATA" indicator to display the values of the last acquisition, the "LAST HEAD DEFECT DETECTED" indicator with the type, and the position of the last defect detected.

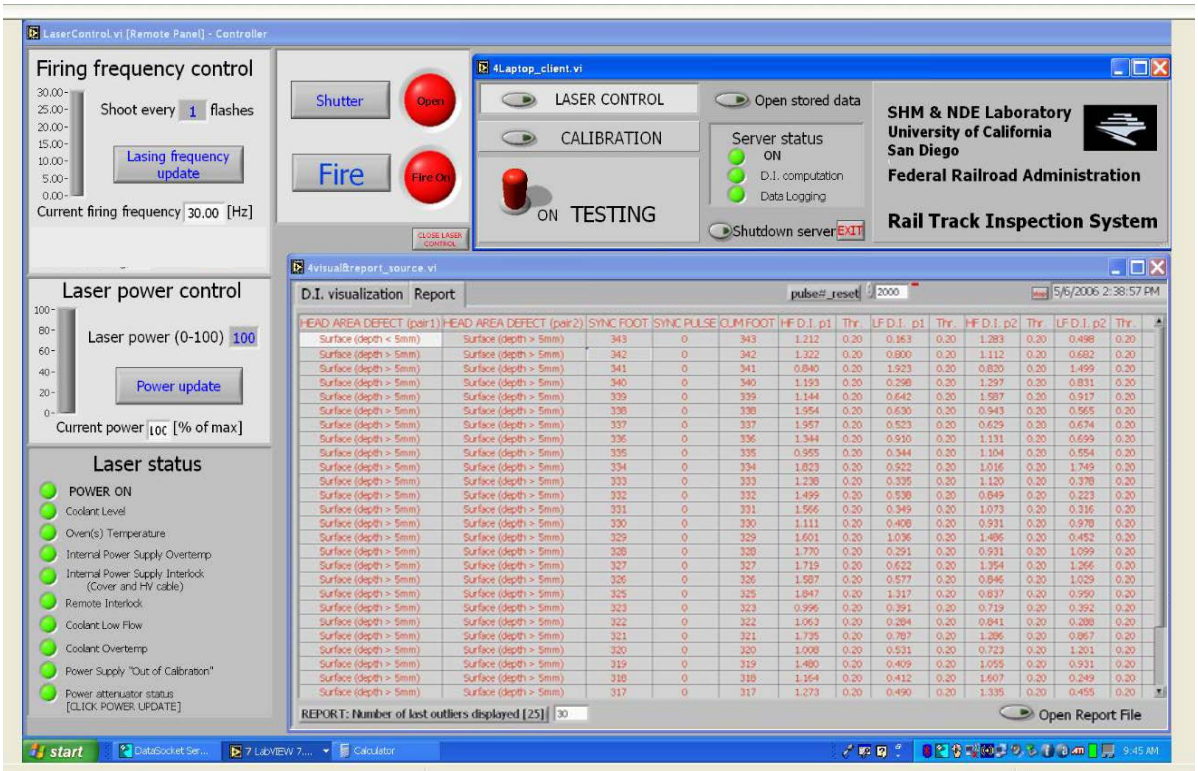

Figure 3.6. Snapshot of the 4visual&report.vi with the Test Report; the LaserControl.vi Is Still Visible in the Background

After the Report tab is selected, the front panel will appear as in Figure 3.6. Whenever a defect is detected, the top row of the report is updated. The report shows the type of defect and its position, along with the associated defect detection settings.

The current version of the software classifies three types of head defects: "small" surface defects, "large" surface defects, and IDs (the meaning of "small" and "large" depend on the filtering bandwidth selected during the calibration phase). The same information contained in the Report window is stored as an .xls file that can be opened by clicking on the button "Open Report File" placed in the bottom right corner of the window. A control placed in the bottom left corner of the window allows selecting the number of rows simultaneously visible in the report screen. The current time is displayed in the top right.

4. First Field Test (Gettysburg, PA, March 2006)

4.1 Test Site Layout

The test site (Figure 4.1) was located on a siding owned by GET, near Gettysburg, PA, at crossing #593-381c. In the picture, the location of the railroad crossing and the side of the inspected track are outlined. A track segment 200 ft long with known defects was surveyed and established as a baseline for repeat testing.

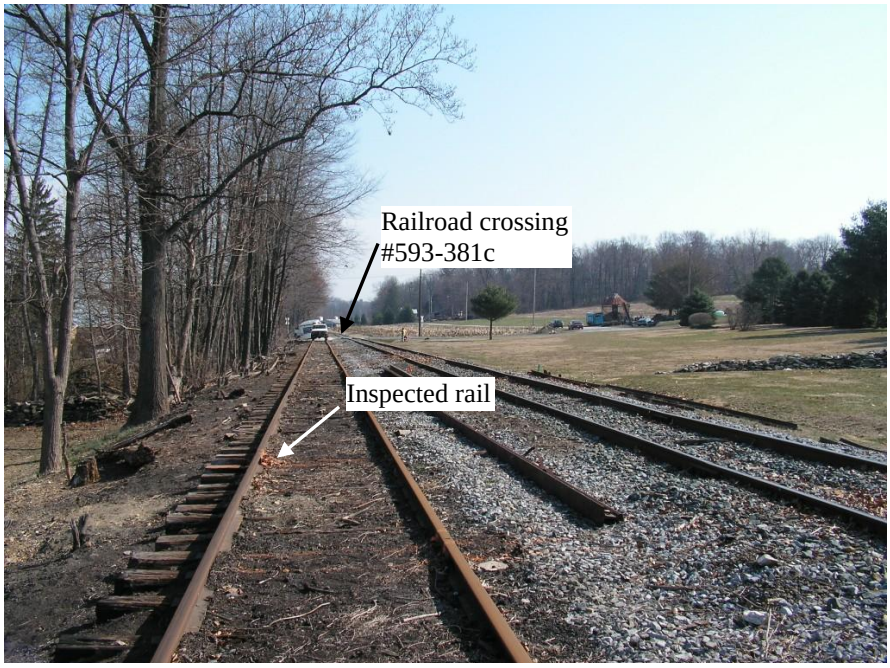

Figure 4.1. Test Site near Gettysburg, PA

Details of the site layout are presented in Table 4.1. The most significant discontinuities, along with their locations (distance from the start of the test zone), are listed. Ten joints were present with some gaps as large as 0.5 in between two rail sections.

Three, 6-foot-long, 139-pound AREMA sections with known IDs in the head were inserted in the inspected portion of rail and fixed by joint bars. From ultrasonic hand mapping before the tests, the sizes of the three IDs were determined to be, respectively, for 80 percent (location 13 in Table 4.1), 10 percent (location 18 in Table 4.1), and 40 percent (location 21 in Table 4.1) of the H.A., respectively.[1] All IDs were believed to be primarily transverse to the rail running direction. Photos of the rail sections containing the IDs are shown in Figures 4.2 and 4.3. The estimated location of the defects (indicated in the photos with the acronym TDD) is marked by a vertical line.

[1] Note that such sizes were shown incorrect following re-mapping of the internal defects conducted during the second field test in April 2007 (see Section 5, Table 5.1).

Two surface cuts (SCs) were also introduced at locations 9 and 10, respectively, using a 4-inch disc grinder. The defects were machined perpendicular to the rail running direction causing 5% and 2% H.A. reductions, respectively. A photo of the SCs is shown in Figure 4.4.

Two oblique (45° inclination from the running direction) SCs were also added at locations 20 and 22, respectively; each cut corresponding to a reduction of approximately 3.5% H.A. As shown in Figure 4.5, the oblique cuts were created close to two joints at locations 19 and 23, respectively.

Table 4.1. Test Site Layout*

Gettysburg Test Site Lay-out (ENSCO/UCSD Rail Flaw Detection - March/29-30/2006)

Location	Foot	Inches	Description
1	0	0	Start of Test Zone
2	13	3	Joint
3	32	0	Chip on gage side of rail head
4	46	3.5	Joint - Orange paint
5	52	5	Large chip (6" long) on gage side of rail head
6	56	2	Large chip (6" long) on gage side of rail head
7	78	9	Flaking on gage side of rail head
8	79	3.5	Joint - flaking on gage side of rail head at joint
9	81	7	Cut surface transverse notch 4mm depth, 50 mm length (~5% H.A)
10	82	7.5	Cut surface transverse notch 2mm depth, 25 mm length (~2% H.A)
11	84	5	Joint - Rail head change 1/2in gap
12	85	6	1st High joint bar (trolley wheel rides up)
13	86	4	Internal transverse defect w/surface head checks (80% HA)
14	87	3.5	Beginning 2nd high joint bar (trolley wheel rides up)
15	88	2	Welded ramp to match rail sizes
16	88	9.5	Joint
17	90	3.5	End 2nd high joint bar (trolley wheel rides up)
18	91	3.5	Internal transverse defect (10% HA)-possibly close to surface
19	93	10	Joint - 1/2 in gap
20	95	1	Cut surface oblique (+45deg) notch 3mm depth, 30mm length (~3.5% H.A) (ADDED LATER)
21	96	4	Internal transverse defect (40% HA)
22	97	8	Cut surface oblique (-45deg) notch 3mm depth, 30mm length (~3.5% H.A) (ADDED LATER)
23	98	9	Joint - Rail head change 1/2in gap
24	99	5	Flaking on gage side of rail head
25	103	0	Chip on gage side of rail head
26	106	7	Flaking chip on field side of rail head
27	112	3	Joint
28	121	0	Flaking chip on field side of rail head
29	126	8	Flaking chip on field side of rail head
30	145	3	Joint (double check) and
31	146	4	Beginnin flaking (severe) on gage side of rail head (continuous)
32	161	0	End flaking (severe) on gage side of rail head (continuous)
33	174	8	Flaking chip on field side of rail head
34	178	3.5	Joint
35	179	0	Flaking chip on field side of rail head
36	191	6	Flaking on gage side of rail head
37	200	0	Finish of test zone

* Remapping of the IDs conducted during the second field test in April 2007 (see Section 5, Table 5.1) revealed that defect sizes provided originally by the contractor were inaccurate.

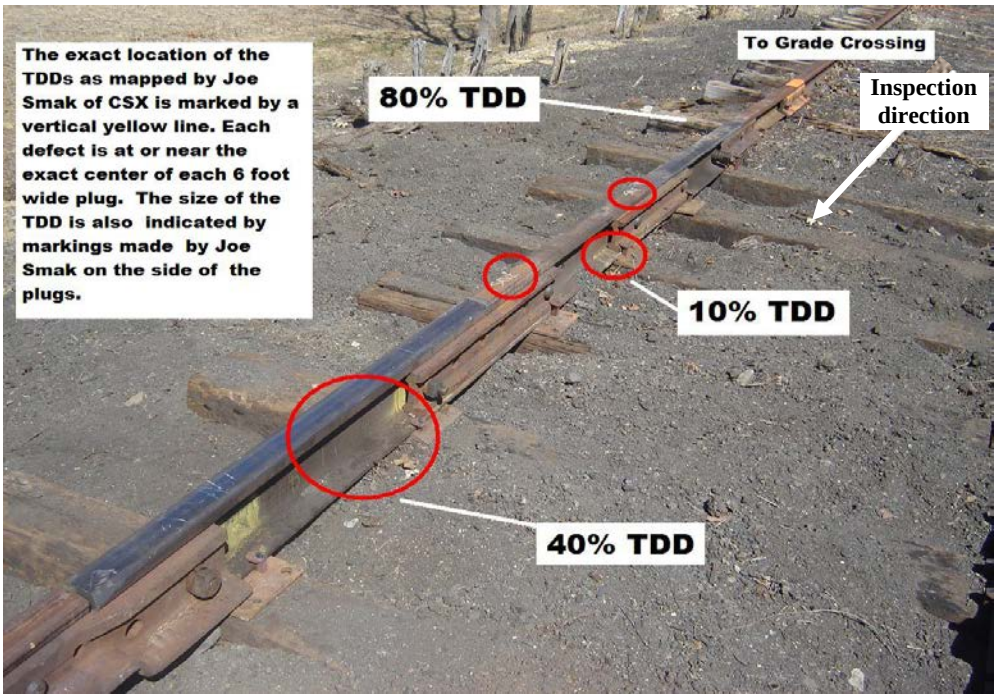

Figure 4.2. Rail Sections with Internal Defects Plugged in the Railroad

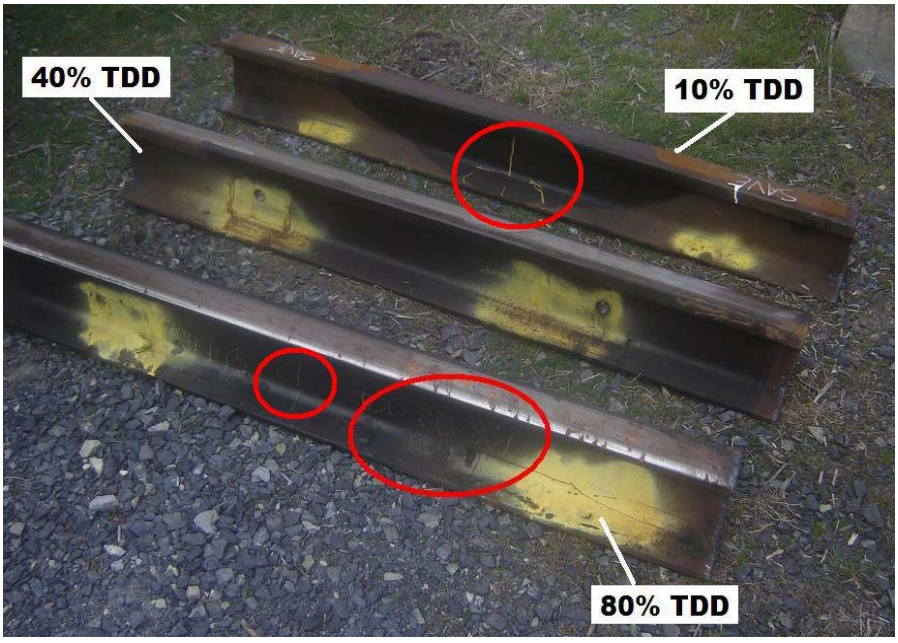

Figure 4.3. Unplugged Rail Sections with Internal Defects

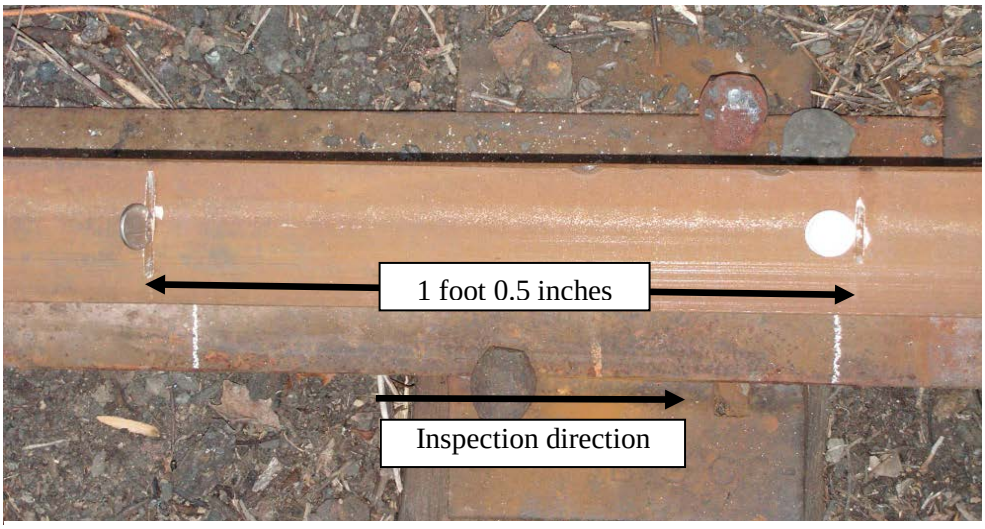

Figure 4.4. Particular of the Surface Transverse Cuts

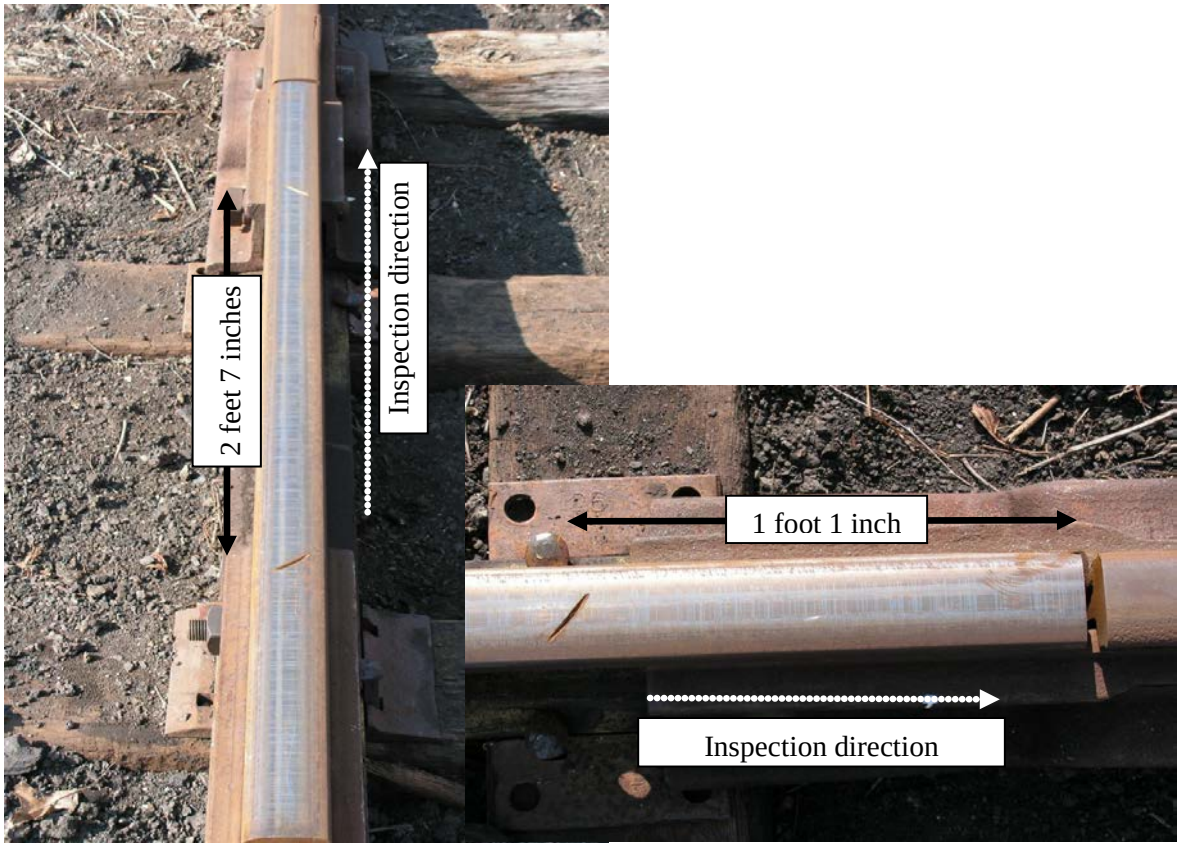

Figure 4.5. Details of the Oblique SCs Added Later

4.2 Prototype Deployment

Pictures of the laser- and air-coupled sensors installed on the cart are shown in Figures 4.6 and 4.7. The cart was designed and constructed by ENSCO under an FRA University-support task. The black metallic box was devised to protect the laser head and the lenses from accidental impacts and dust; in addition, the box prevents accidental reflections of the laser beam.

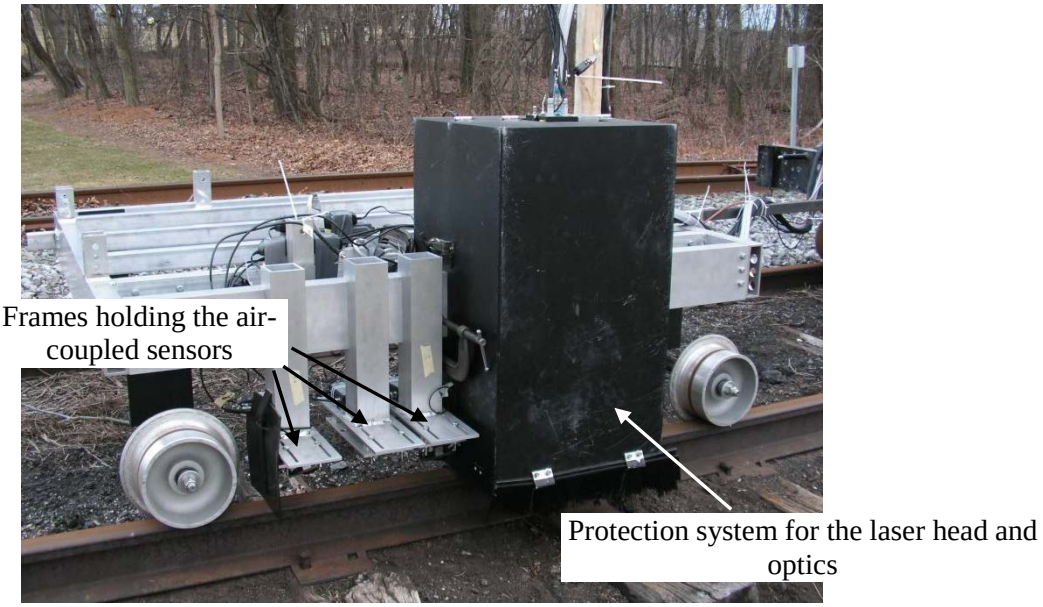

Figure 4.6. Laser Head and Sensors on ENSCO's Cart during First Field Tests

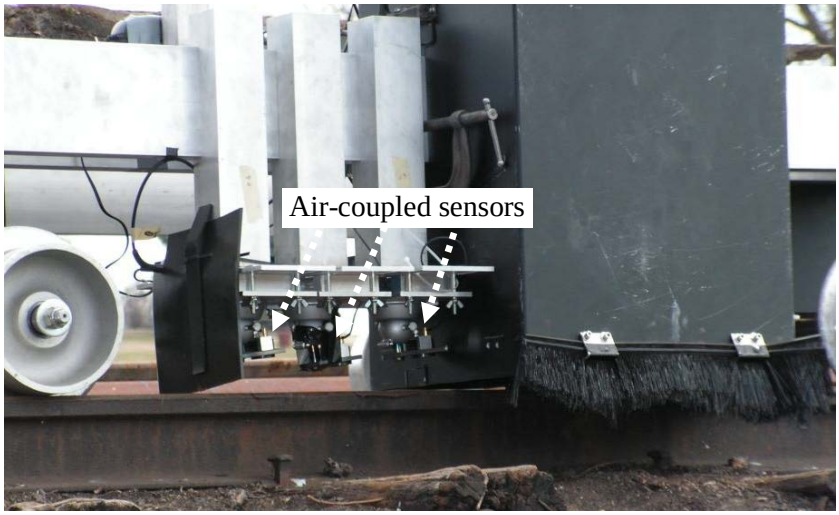

Figure 4.7. Detail of the Air-Coupled Sensors

Figure 4.8 is a schematic of the field test sensor layout. The minimum distance between the first sensor (#1) and the laser was chosen so as to avoid superposition between the air shock and the ultrasound waves traveling in the rail (Lanza di Scalea et al., 2005a). The angle θ was optimized manually by monitoring the amplitude of the detected waveforms.

Sensors #1 and #3 formed the first pair, hereafter indicated as sensor pair 1 (s.p.1); sensors #2 and #4 formed sensor pair 2 (s.p.2). The sensor lift-off distance *h* was maintained at 2.5 in.

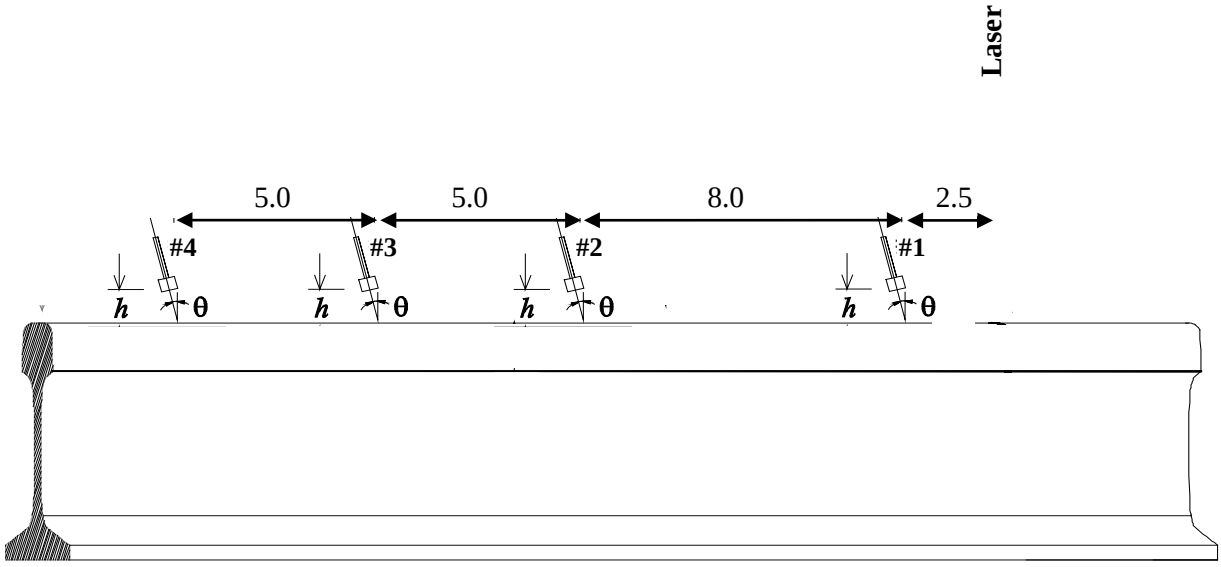

Figure 4.8. Laser/Air-Coupled Sensor Layout for the Field Tests (dimension in inches; drawing not to scale)

The inspection prototype towed by the hy-railer is shown in Figure 4.9. The back end of the truck housed the laser power supply, the PXI unit, and the laptop client. A 1,200-watt generator was used to power all equipment.

Figure 4.9. The Inspection Prototype Towed by the FRA Hy-Railer Managed by ENSCO during the First Field Test

4.3 Test Results

In these first field tests, a total of 32 tests were conducted in 2 days and recorded along the 200-foot rail test site described in Table 4.1. A summary of all test conditions is provided in Table 4.2. The testing sessions started and ended slightly before and slightly after the monitored rail segment, as indicated in the fourth and fifth columns of the table. Tests 1 through 10 and 23 through 26 were performed under "dry" conditions (i.e., ultrasound was generated by the laser pulse irradiating a dry surface of the rail head). In the remaining tests, the rail was wetted by using a water pressure sprayer.

Two different combinations of the signal processing (filtering) parameters were used as indicated in the last column of the table. This was done to test the effect of these parameters on the defect detection reliability.

As schematized in Figure 4.8, the gage length of s.p.1 (i.e., the distance between sensors #1 and #3 (s.p.1)) was maintained at 13 in, and the distance between sensors #2 and #4 (s.p.2) was maintained at 10 in. The lasing repetition rate was set at 30 Hz throughout the tests.

Figures 4.10 and 4.11 illustrate the recordings from tests 1 and 2, respectively. The results are shown for the portion of the rail between the 76- and 120-foot points, where the IDs and the SCs were located. Each figure displays the D.I.s recorded as a function of position (foot) by the two sensor pairs and for two different filtering bandwidths, namely (top to bottom) a) H.F.-D.I. s.p.1, b) L.F.-D.I. s.p.1, c) H.F.-D.I. s.p.2, and d) L.F.-D.I. s.p.2.

Table 4.2. Summary of Test Conditions

Test conditions (Rail flaw detection)			Gettysburg Test Conditions (ENSCO/UCSD Rail Flaw Detection - March/29-30/2006)							
Test num	Date	Time (PST)	Position before start point (0 ft)	Position after finish point (200 ft)	Water (Y/N)	Movie file (Y/N)	Firing freq / /overlap	Sensor gage (pair 1)	Sensor gage (pair 2)	DWT coeff. @ freq bands
1	3/29/2006	9:26	12' 7"	8' 4"	N	Y	30Hz / 50%	13"	10"	0/2/2/0
2	3/29/2006	9:44	10' 5"	9' 7"	N	Y	30Hz / 50%	13"	10"	0/2/2/0
3	3/29/2006	9:52	7' 8"	8' 6"	N	Y	30Hz / 50%	13"	10"	0/2/2/0
4	3/29/2006	10:29	10' 4"	5' 1"	N	Y	30Hz / 50%	13"	10"	0/2/2/0
5	3/29/2006	10:37	16' 3"	7' 8"	N	Y	30Hz / 50%	13"	10"	0/2/2/0
6	3/29/2006	10:45	11' 9"	4' 9"	N	Y	30Hz / 50%	13"	10"	0/2/2/0
7	3/29/2006	10:50	12' 0"	6' 6"	N	Y	30Hz / 50%	13"	10"	0/2/2/0
8	3/29/2006	10:56	12' 3"	6' 9"	N	Y	30Hz / 50%	13"	10"	0/2/2/0
9	3/29/2006	11:01	12' 3"	8' 10"	N	Y	30Hz / 50%	13"	10"	0/2/2/0
10	3/29/2006	11:08	12' 2"	7' 8"	N	Y	30Hz / 50%	13"	10"	0/2/2/0
11	3/29/2006	12:44	11' 5"	10' 2"	Y (1/2 wet)	Y	30Hz / 50%	13"	10"	0/2/2/0
12	3/29/2006	12:51	9' 1"	9' 4"	Y	Y	30Hz / 50%	13"	10"	0/2/2/0
13	3/29/2006	12:56	9' 10"	7' 7"	Y	Y	30Hz / 50%	13"	10"	0/2/2/0
14	3/29/2006	1:06	7' 10"	7' 10"	Y	Y	30Hz / 50%	13"	10"	0/2/2/0
15	3/29/2006	1:48	6' 2"	8' 7"	Y	Y	30Hz / 50%	13"	10"	0/2/2/0
16	3/29/2006	1:54	10' 7"	9' 6"	Y (50% wet)	Y	30Hz / 50%	13"	10"	0/2/2/0
17	3/29/2006	2:18	10' 10"	7' 5"	Y	Y	30Hz / 50%	13"	10"	0/2/2/0
18	3/29/2006	2:23	10' 1"	8' 9"	Y	Y	30Hz / 50%	13"	10"	0/2/2/0
19	3/29/2006	2:33	5' 6"	10' 3"	Y	Y	30Hz / 50%	13"	10"	0/2/2/0
20	3/29/2006	2:38	4' 9"	8' 11"	Y	Y	30Hz / 50%	13"	10"	0/2/2/0
21	3/29/2006	2:46	defected area only		Y	Y	30Hz / 50%	13"	10"	0/2/2/0
22	3/29/2006	2:54	8' 7"	9' 7"	Y	Y (calibratior	30Hz / 50%	13"	10"	0/2/2/0
23	3/30/2006	7:31	11' 10"	8' 7"	N	Y	30Hz / 50%	13"	10"	0/2/2/0
24	3/30/2006	7:43	10' 6"	10' 6"	N	Y	30Hz / 50%	13"	10"	0/2/2/0
25	3/30/2006	7:49	9' 5"	10' 0"	N	Y	30Hz / 50%	13"	10"	0/2/2/0
26	3/30/2006	8:08	7' 5"	11' 7"	N	Y	30Hz / 50%	13"	10"	4/6/4/2
27	3/30/2006	8:13	10' 7"	6' 10"	Y	Y (very long	30Hz / 50%	13"	10"	4/6/4/2
28	3/30/2006	8:19	8' 4"	9' 8"	Y	Y	30Hz / 50%	13"	10"	4/6/4/2
29	3/30/2006	8:22	11' 01"	9' 0"	Y	Y (60% wet)	30Hz / 50%	13"	10"	4/6/4/2
30	3/30/2006	8:27	10' 6"	8' 2"	Y	Y	30Hz / 50%	13"	10"	4/6/4/2
31	3/30/2006	9:34	9' 7"	?	Y	?	30Hz / 50%	13"	10"	0/2/2/0
32	3/30/2006	9:12	defected area only		Y	?	30Hz / 50%	13"	10"	4/6/4/2

The bottom plot of Figures 4.10 and 4.11 is included to facilitate the visualization of the position of each of the salient discontinuities. In these plots, the joints are placed at ordinate 5, the transverse SCs at ordinate 4, the IDs at ordinate 3, and the flaking at ordinate 1. In the four D.I. plots, successfully detected joints (J), SCs, or IDs are highlighted with circles. Since the two sensor pairs and filtering bandwidths cover complementary regions of the rail head, a defect should be considered successfully detected if any of the four D.I. plots shows an index clearly above the defect free value. For example, Figure 4.11 for test 2 shows that all major defects, with the exception of the third ID, were detected by at least one of the four D.I. plots.

A summary of all test results with estimates of the probability of detection (POD) is shown in Table 4.3, which is discussed later in the report. The fact that the baseline D.I. values in the figures are not necessarily one as theoretically expected from equation 1 is simply due to the practical impossibility of obtaining the exactly same sensitivities from the two sensors in each pair. This, however, does not constitute a problem since only *relative* changes in D.I. from the baseline value are monitored to detect a potential defect.

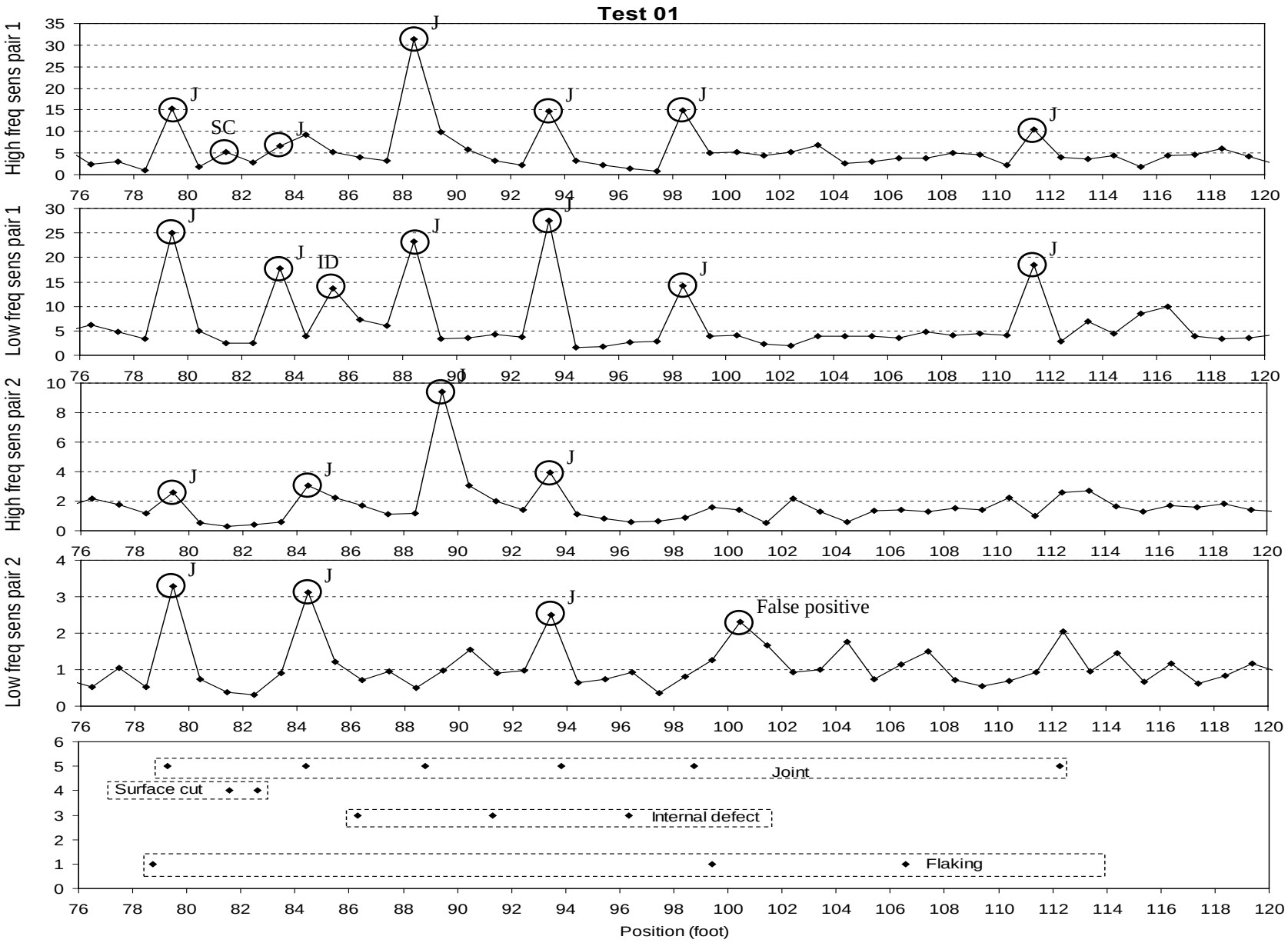

Figure 4.10. Results of Test 01

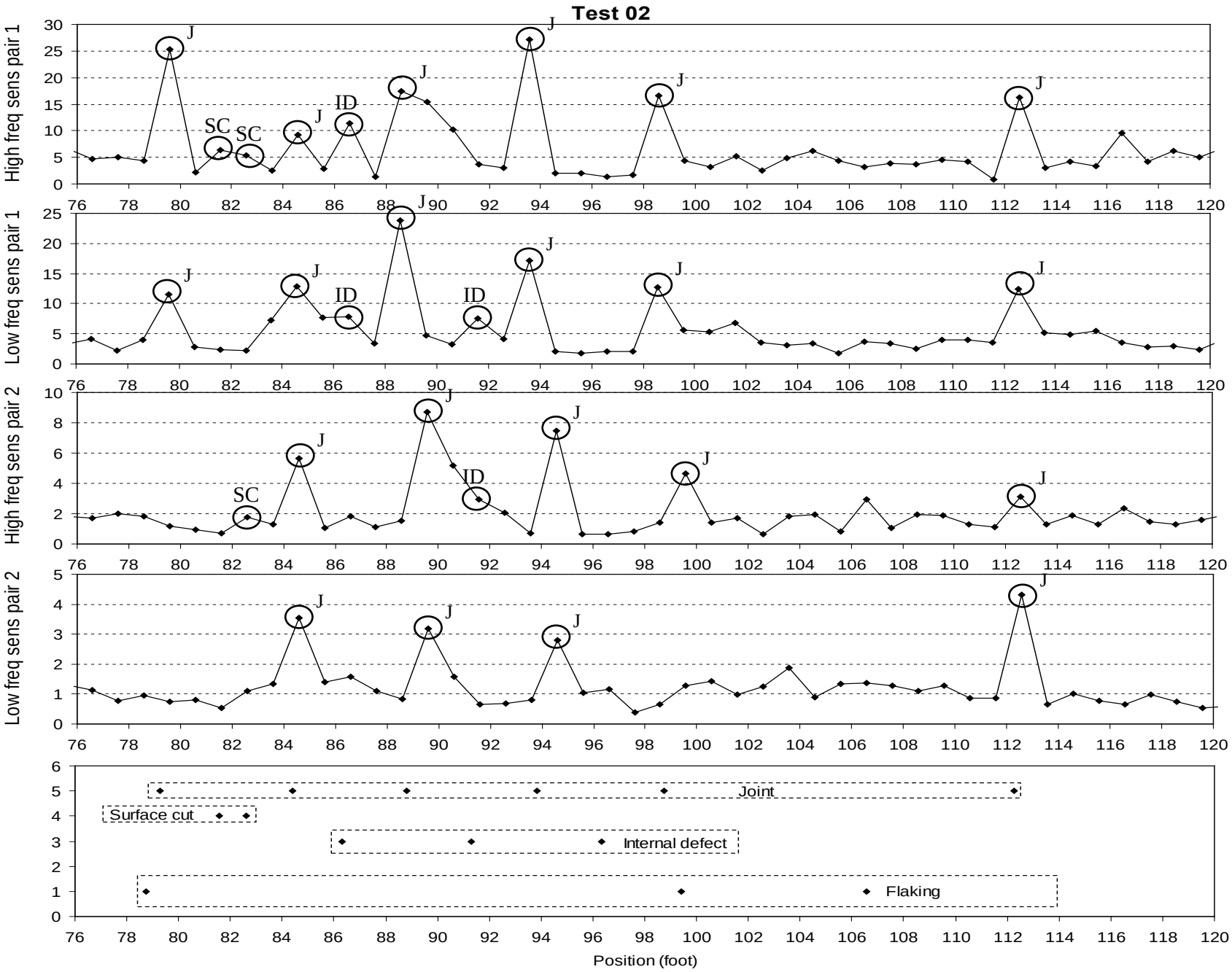

Figure 4.11. Results of Test 02

It can be noted in the figures that the same discontinuity can be detected at position *j* by s.p.1 and at position *j+1* by s.p.2. This is the case, for example, of the joint at location 16 (Table 4.1), measured position 88 9.5/12 ft in Figure 4.11. This is simply due to the longitudinal offset of the two sensor pairs.

4.4 Summary of First Field Test Results

The results of all tests shown earlier are summarized in Table 4.3. In the first column, the test number is indicated along with the dry or wet condition of the rail. The second through eighth columns indicate whether the seven defects were detected (with the *1* symbol) or not (no symbol). It should be noted that the oblique SCs in columns six and eight were created only after test 16, and thus, a N/A indication is shown for the preceding tests.

In the last row, the POD estimated from all relevant tests is indicated for each of the seven defects. As discussed earlier, a defect was considered successfully detected if at least one of the four D.I.s (H.F.-D.I. s.p.1, L.F.-D.I. s.p.1, H.F.-D.I. s.p.2, or L.F.-D.I. s.p.2.) was activated. In this row, the most sensitive of the four D.I.s is also shown in italic for each of the defects.

The following conclusions can be drawn from the first field tests:

1) Overall, the system performed very well in detecting the two SCs, two of the three IDs, and the second oblique SC. The detection performance was poor for the third ID and the first oblique SC.

2) The fact that the SCs 1 and 2 (5% and 2% H.A., respectively) were successfully detected demonstrates the ability of the system to target defects well below the 10% H.A. limit commonly used by railroad owners to consider removing the rail from service.

3) The fact that the IDs 1 and 2 were successfully detected demonstrates the ability of the system to achieve the 10% H.A. detectability limit also for the internal flaws.

4) It is unclear why ID 3 was seldom detected. Hand remapping of this flaw was scheduled to verify its dimensions before the second field test (see Section 5). A possible reason is the fact that the flaw was located too deep into the rail head. Modifications to the prototype have been made in the laboratory to ensure coverage of the entire head cross section.

5) A possible reason for the unsatisfactory performance in detecting oblique cut 1 is the fact that this small discontinuity (3.5% H.A.) was located closer to the joint than allowed by the spatial resolution of the system.

6) Wetting the rail surface increased the POD for all defects (with the exception of oblique SC 2). The improvement from wetting, although significant, was not dramatic. In the end, a compromise must be struck between the burden of carrying a water supply and an acceptable level of POD.

7) As expected, the SCs were predominantly detected by the H.F.-D.I.s mostly sensitive to surface features. Similarly, ID 1 was predominantly detected by the L.F.-D.I.s mostly sensitive to features deeper into the rail head. The fact that ID 2 was primarily detected by the H.F.-D.I.s suggests that the flaw was very close to breaking the surface. This

hypothesis is consistent with the independent findings of the prior hand mapping for this defect.

Table 4.3. Summary of Gettysburg First Field Test Results

Test number	Wet/dry	Surface cut 1 (~5% H.A.)				Surface cut 2(~2% H.A.)				Internal defect 1 (80%HA)				Internal defect 2 (10%HA)				Oblique surf cut 1 (~3.5% H.A.)				Internal defect 3 (40%HA)				Oblique surf cut 2 (~3.5% H.A.)			
		HF1	LF1	HF2	LF2	HF1	LF1	HF2	LF2	HF1	LF1	HF2	LF2	HF1	LF1	HF2	LF2	HF1	LF1	HF2	LF2	HF1	LF1	HF2	LF2	HF1	LF1	HF2	LF2
1	dry	1				1					1							N/A	N/A	N/A	N/A					N/A	N/A	N/A	N/A
2	dry	1				1				1	1				1		1	N/A	N/A	N/A	N/A					N/A	N/A	N/A	N/A
3	dry	1		1		1				1	1	1				1		N/A	N/A	N/A	N/A					N/A	N/A	N/A	N/A
4	dry	1				1					1	1				1		N/A	N/A	N/A	N/A					N/A	N/A	N/A	N/A
5	dry																	N/A	N/A	N/A	N/A					N/A	N/A	N/A	N/A
6	dry	1	1			1	1				1		1	1		1		N/A	N/A	N/A	N/A					N/A	N/A	N/A	N/A
7	dry	1		1		1		1			1		1	1				N/A	N/A	N/A	N/A					N/A	N/A	N/A	N/A
8	dry										1		1		1		1	N/A	N/A	N/A	N/A					N/A	N/A	N/A	N/A
9	dry									1	1							N/A	N/A	N/A	N/A					N/A	N/A	N/A	N/A
10	dry	1				1						1				1		N/A	N/A	N/A	N/A					N/A	N/A	N/A	N/A
11	wet	1				1						1				1		N/A	N/A	N/A	N/A					N/A	N/A	N/A	N/A
12	wet	1		1	1	1		1	1	1	1		1			1	1	N/A	N/A	N/A	N/A					N/A	N/A	N/A	N/A
13	wet	1				1				1	1	1	1		1	1	1	N/A	N/A	N/A	N/A					N/A	N/A	N/A	N/A
14	wet	1	1			1	1			1	1	1	1			1		N/A	N/A	N/A	N/A					N/A	N/A	N/A	N/A
15	wet	1		1	1	1		1	1	1	1		1	1	1	1		N/A	N/A	N/A	N/A				1	N/A	N/A	N/A	N/A
16	wet	1				1				1	1	1		1	1	1		N/A	N/A	N/A	N/A					N/A	N/A	N/A	N/A
17	wet			1				1		1	1	1		1		1		1		1									
18	wet	1				1				1	1			1		1		1								1		1	
19	wet	1				1					1		1			1	1												
20	wet										1		1	1		1										1			
23	dry									1	1		1			1									1			1	1
24	dry	1	1	1	1	1	1	1	1		1		1		1	1	1				1					1	1		
25	dry										1		1	1	1	1											1		1
PROB. OF DETECTION		**Surface cut 1 (~5% H.A.)**				**Surface cut 2 (~2% H.A.)**				**Internal defect 1**				**Internal defect 2**				**Oblique surf cut 1 (~3.5% H.A.)**				**Internal defect 3**				**Oblique surf cut 2 (~3.5% H.A.)**			
dry conditions		**61.5% (over 13 tests)**				**61.5% (over 13 tests)**				**92.3% (over 13 tests)**				**76.9% (over 13 tests)**				**33.3% (over 3 tests)**				**7.7% (over 13 tests)**				**100% (over 3 tests)**			
wet conditions		**90% (over 10 tests)**				**90% (over 10 tests)**				**100% (over 10 tests)**				**100% (over 10 tests)**				**50% (over 4 tests)**				**10% (over 10 tests)**				**50% (over 4 tests)**			
Most sensitive parameter		*High freq. sensor pair 1*				*High freq. sensor pair 1*				*Low freq. sensor pair 1*				*High freq. sensor pair 2*				*High freq. sensor pair 1*				*Low freq. sensor pair 2*				*High freq. sensor pair 1*			

Notes: HF1= high-frequency parameter of sensor pair 1
LF1 = low-frequency parameter of sensor pair 1
HF2 = high-frequency parameter of sensor pair 2
LF2 = low-frequency parameter of sensor pair 2
1 = defect detected
N/A = not applicable (defect not present during test)
For calculation of POD, defect is considered detected if any of the four parameters (HF1, LF1, HF2, or LF2) is activated in a given test.
Sizes of IDs reported here were shown incorrect following remapping of these defects during the second field test in April 2007 (see Section 5, Table 5.1).

5. Second Field Test (Gettysburg, PA, April 2007)

This section discusses the second field tests performed in April 2007, again with the technical support of ENSCO, FRA's technical support contractor. The test site was the same as the first field test site on a siding at Starner's crossing (#593-381c) of the GET near Gettysburg, PA, with known rail flaws.

The details of the modifications made to the prototype for the second tests follow in the next sections. In summary:

1) The number of sensors was increased from four to six to constitute three sensing pairs;
2) The bi-directionality of the laser ultrasound source was exploited;
3) The data acquisition software was changed to allow for subfoot spatial resolution so as to increase the detectability of defects closely spaced between them or close to a joint;
4) The signal processing software was rewritten to increase the speed of computation of H.F.-D.I. and L.F.-D.I.; this upgrade allowed testing at the sub-foot spatial resolution without loss of data; and
5) A new cart was designed by ENSCO with greater stability than that of the first test.

The same total length of 200 ft of track was tested. The three IDs were hand mapped before testing. The mapping was done by the UCSD team under FRA supervision using ultrasonic search unit, which was purchased prior to the tests. A classical pulse-echo, ultrasonic wedge inspection was carried out for the mapping. As customary in TDD defect mapping, a 2.25-megahertz transducer was used with a 70° wedge. The orientation of each defect was determined from the inspection direction; the size of each defect was determined by hand scanning and computing the appropriate conversions between the position of the transducer and the extent of the reflector (defect). Three independent mappings were conducted for each defect to extract a statistically meaningful size.

All defects were predominantly oriented at 20° from the vertical to the rail head, as is common in TDDs (Figure 5.1). ID 1 (location 13 in Table 5.1) was inclined away from the running direction; it was located in the head gage side, and its average size from three measurements was 3.6% H.A. ID 2 (location 18 in Table 5.1) was oriented toward the running direction, also in the gage side, and its average size was 34.6% H.A. ID 3 (location 21 in Table 5.1) was oriented as the previous defect, but it was located in the center head; its size was measured at 12.4% H.A. These results differ substantially from what was assumed in the first field test (Table 4.1, Figures 4.1 and 4.2). It is clear that in the previous test the sizes of these defects were generally overestimated, which consequently improves the performance of the prototype as reported in Table 4.3. The defect sizes assumed in the first field test came from a consultant's independent mapping, which was neither performed nor controlled by the UCSD team. Miscommunications in labeling the different test sections may have also occurred at the time of the first test mapping.

The other defects present at the site were unchanged from the first field test. These included the following: the two SCs (5% and 2% H.A.), which were machined at locations 9 and 10 perpendicular to the rail running direction in the center head; and the two oblique cuts (3.5% H.A.) at locations 20 and 22, also machined in central locations of the rail head. Table 5.4 shows the site layout updated in light of the new mapping of the three IDs.

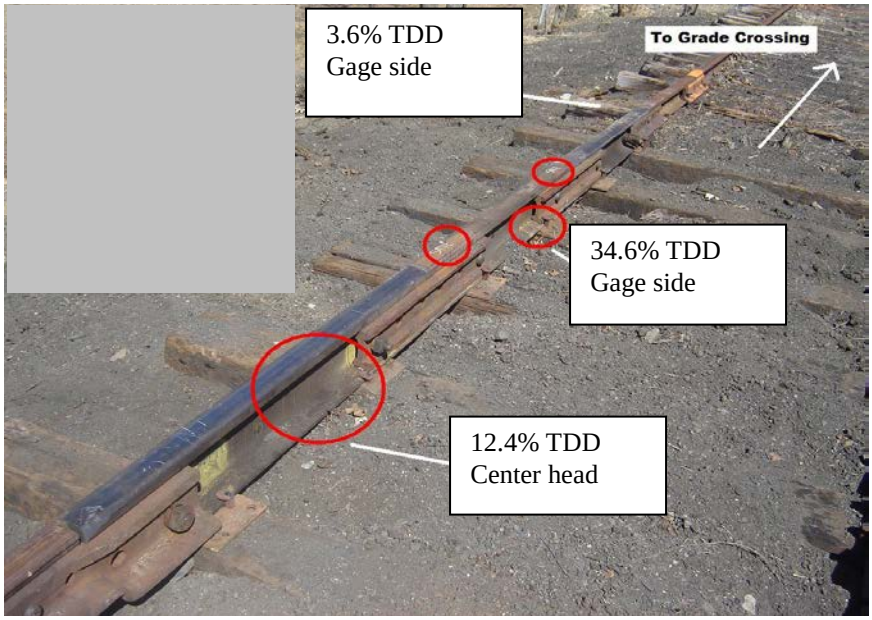

Rail head area: 75mm*180mm=2,625mm^2

INTERNAL TRANSVERSE DEFECT 1

Location: *gage side(Detail Fracture)*

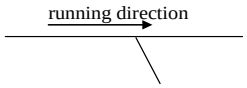

1st measurement:	2nd measurement:	3rd measurement
Defect depth : 5.4 mm	Defect depth : 9 mm	Defect depth : 4.3 mm
Defect width: 10mm	Defect width: 17 mm	Defect width: 18 mm
2% H.A.	**5.8% H.A.**	**3% H.A.**

AVERAGE OF 3 MEASUREMENTS: 3.6% H.A.

INTERNAL TRANSVERSE DEFECT 2

Location: *gage side(Detail Fracture)*

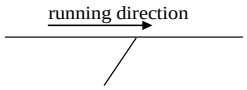

1st measurement:	2nd measurement:	3rd measurement
Defect depth : 25.2 mm	Defect depth : 21.6 mm	Defect depth : 38.8 mm
Defect width: 38mm	Defect width: 37.5 mm	Defect width: 25.4 mm
36% H.A.	**31% H.A.**	**37% H.A.**

AVERAGE OF 3 MEASUREMENTS: 34.6% H.A.

INTERNAL TRANSVERSE DEFECT 3

Location: *center head (Transverse Fissure)*

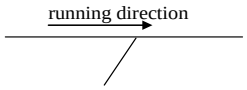

1st measurement:	2nd measurement:	3rd measurement
Defect depth : 18 mm	Defect depth : 17.6 mm	Defect depth : 20.5 mm
Defect width: 15mm	Defect width: 16 mm	Defect width: 22.2 mm
10.3% H.A.	**10% H.A.**	**17% H.A.**

AVERAGE OF 3 MEASUREMENTS: 12.4% H.A.

Figure 5.1. ID Mapping (2.25-megahertz ultrasonic transducer with 70° wedge)

Table 5.1. Updated Site Layout for Second Field Test following Hand Remapping of TDDs

Gettysburg Test Site Lay-out (ENSCO/UCSD Rail Flaw Detection - April/24-25-26/2007)

Location	Foot	Inches	Description
1	0	0	Start of Test Zone
2	13	3	Joint
3	32	0	Chip on gage side of rail head
4	46	3.5	Joint - Orange paint
5	52	5	Large chip (6" long) on gage side of rail head
6	56	2	Large chip (6" long) on gage side of rail head
7	78	9	Flaking on gage side of rail head
8	79	3.5	Joint - flaking on gage side of rail head at joint
9	81	7	Cut surface transverse notch 4mm depth, 50 mm length (~5% H.A)
10	82	7.5	Cut surface transverse notch 2mm depth, 25 mm length (~2% H.A)
11	84	5	Joint - Rail head change 1/2in gap
12	85	6	1st High joint bar (trolley wheel rides up)
13	86	4	Internal transverse defect w/surface head checks (~4% HA)
14	87	3.5	Beginning 2nd high joint bar (trolley wheel rides up)
15	88	2	Welded ramp to match rail sizes
16	88	9.5	Joint
17	90	3.5	End 2nd high joint bar (trolley wheel rides up)
18	91	3.5	Internal transverse defect (~35% HA)-possibly close to surface
19	93	10	Joint - 1/2 in gap
20	95	1	Cut surface oblique (+45deg) notch 3mm depth, 30mm length (~3.5% H.A) (ADDED LATER)
21	96	4	Internal transverse defect (~12% HA)
22	97	8	Cut surface oblique (-45deg) notch 3mm depth, 30mm length (~3.5% H.A) (ADDED LATER)
23	98	9	Joint - Rail head change 1/2in gap
24	99	5	Flaking on gage side of rail head
25	103	0	Chip on gage side of rail head
26	106	7	Flaking chip on field side of rail head
27	112	3	Joint
28	121	0	Flaking chip on field side of rail head
29	126	8	Flaking chip on field side of rail head
30	145	3	Joint (double check) and
31	146	4	Beginnin flaking (severe) on gage side of rail head (continuous)
32	161	0	End flaking (severe) on gage side of rail head (continuous)
33	174	8	Flaking chip on field side of rail head
34	178	3.5	Joint
35	179	0	Flaking chip on field side of rail head
36	191	6	Flaking on gage side of rail head
37	200	0	Finish of test zone

5.1 Computational Study of High-Frequency Ultrasonic Wave Propagation in the Rail Head by the SAFE Method

Before the results of the second field test are discussed in detail, Section 5.1 describes a parallel study performed using computational tools developed at UCSD (Bartoli et al., 2006) to better understand the properties of ultrasonic wave propagation in the rail head. The focus of this study was to examine ultrasonic frequencies as high as the ones used in the rail flaw detection prototype. Prior numerical studies of wave propagation in rails conducted at UCSD (Bartoli et al., 2005) examined low-frequency waves, below 40 kHz, in particular the vertical bending mode and its interaction with transverse head defects. At the low-frequency ranges, a commercial FE package, ABAQUS EXPLICIT, was found appropriate for the modeling.

To study the complete vibration solutions of rails, including higher frequencies, a SAFE was adopted more recently as a tool. SAFE methods, also referred to in the literature as spectral or waveguide FE methods, have emerged for modeling guided wave propagation numerically as an alternative to the "exact" methods based on the superposition of bulk waves, which include the popular matrix-based methods.

The general SAFE approach for extracting dispersive solutions uses a FE discretization of the cross section of the waveguide alone. The displacements along the wave propagation direction are conveniently described in an analytical fashion as harmonic exponential functions. Thus, only a bi-dimensional discretization of the cross section is needed, with considerable computational savings compared with a three-dimensional (3-D) discretization of the entire waveguide. The SAFE solutions are obtained in a stable manner from an eigenvalue problem and, thus, do not require the root-searching algorithms used in superimposition of bulk waves (SPBW) approaches. In addition, because polynomial approximation of the displacement field along the waveguide is avoided, the method is only applicable to predicting waves with very short wavelengths, where a traditional 3-D approximation may fail.

The SAFE method used at UCSD includes wave damping, which is important to predict those mode-frequency combinations that travel with minimal losses, thus allowing to maximize the inspection range. When accounting for damping, the exact energy velocity, rather than the conventional group velocity, is calculated along with the frequency-dependent attenuation of the modes.

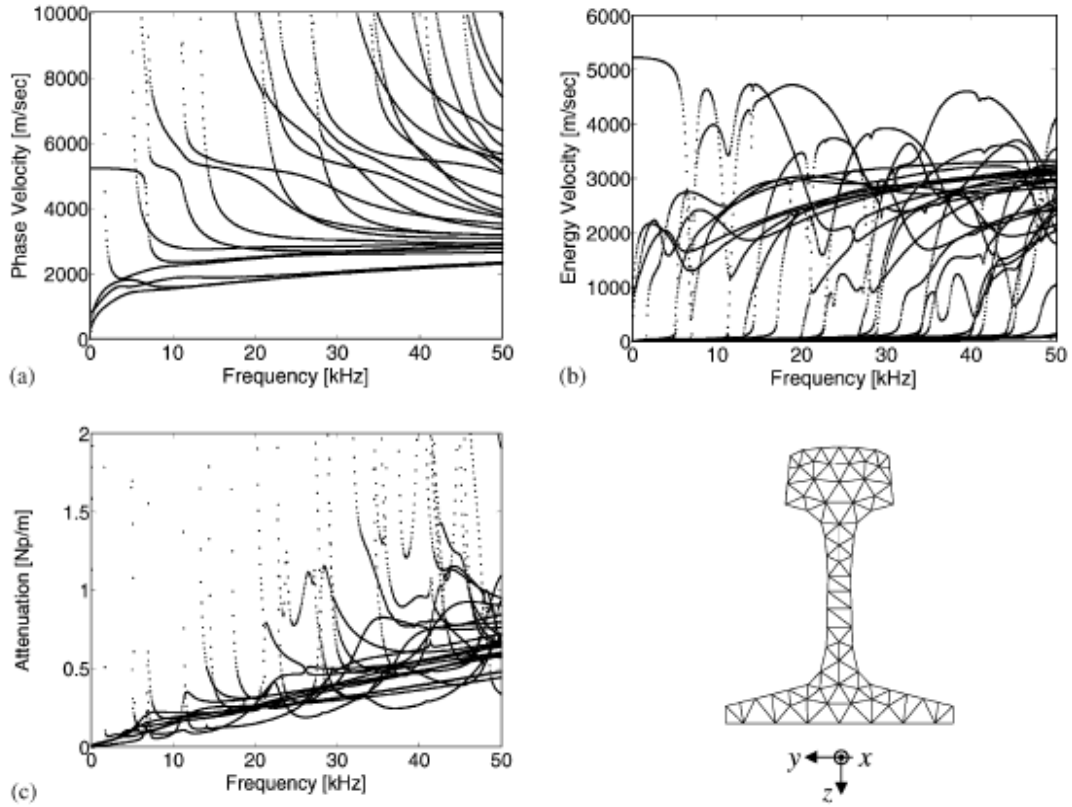

Figure 5.2. SAFE Modeling of High-Frequency Wave Propagation in Rails: Dispersion Results for a 115-Pound AREMA, Viscoelastic Rail for Waves Propagating along the Rail Running Direction: (a) Phase Velocity, (b) Energy Velocity, and (c) Attenuation (from Bartoli et al., 2006)

The rail considered in the recent analyses was a typical 115-pound AREMA section, modeled as an isotropic material with hysteretic damping, with the following properties: density ρ = 7,932 kg/m^3, bulk longitudinal velocity c_L = 5,960 m/s, bulk shear velocity c_S = 3,260 m/s, longitudinal attenuation k_L = 0.003 Np/wavelength, and shear attenuation k_T = 0.043 Np/wavelength. The rail cross section has a complex geometry with one vertical axis of symmetry. The mesh used 81 nodes for 106 triangular elements with linear interpolation displacement functions. According to the SAFE analysis, the mesh was performed on the cross section of the rail alone. The dispersion results, in terms of velocities and attenuation curves, are also shown in Figure 5.2 up to a frequency of 50 kHz. The complexity of the modes is evident in these plots.

It was of interest to investigate the strain energy density generated by certain modes across the rail head. In fact, the detectability of a head defect is generally proportional to the wave strain energy transmission or reflection by the discontinuity. Thus, higher energy at the surface of the head is more effective for detecting surface-breaking cracks; high energy beneath the surface of the head is desired for detecting internal cracks. The depth of penetration of the wave energy into the rail head is determined by the specific mode and, more importantly, by the associated frequency. As a general rule of thumb, surface (Rayleigh) waves penetrate into the surface for a depth equal to their wavelength, which is inversely proportional to their frequency. Hence, higher frequencies travel closer to the surface, whereas lower frequencies penetrate deeper into the surface. This frequency discrimination is used in the rail flaw detection prototype for defect classification, as discussed earlier in this report.

To predict strain energy densities at high frequency, a finer mesh was applied to the rail model analyzed by SAFE (Figure 5.3). Only the top half of the rail was modeled, because the frequencies considered of negligible energy travel into the web or base.

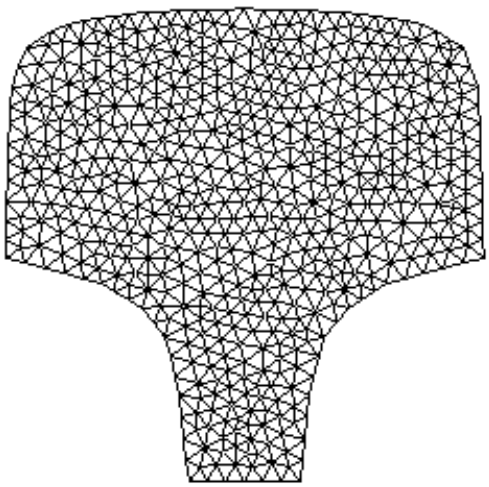

Figure 5.3. SAFE Mesh of the Rail Head for Predicting Cross-Sectional Distribution of the High-Frequency Ultrasonic Energy

Figure 5.4 shows the SAFE results of cross-sectional strain energy for four symmetric vibrational modes at specific propagation frequencies. It is clearly visible that the energy of the

selected modes is confined to a region with a depth of 10 mm from the top of the rail head. This is confirmed by independent results by a group in the United Kingdom obtained with an alternate method of analysis (Hesse and Cawley, 2006). This result confirms that the vibrational modes used in the rail flaw prototype are surface-wave type, thus allowing the frequency discrimination approach for defect classification. Knowledge of these energy distributions is also important to further refine the defect classification by purposely generating modes with energy concentrations in a given region of the rail head.

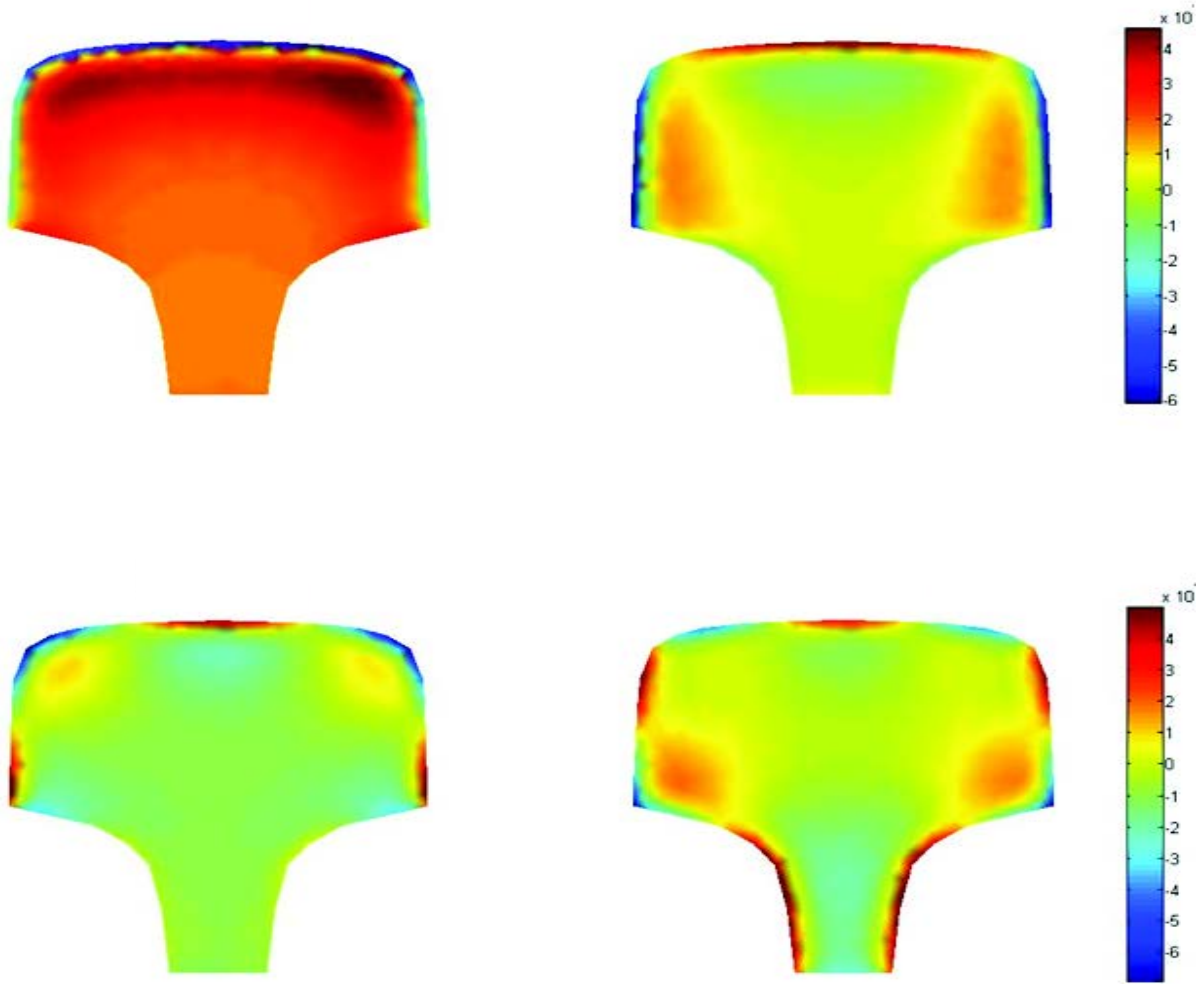

Figure 5.4. Strain Energy Distribution of Selected Symmetric Modes of Rail Vibrations at Specific Frequencies

5.2 The New Cart

The second test used a new cart completely redesigned and constructed by ENSCO to provide greater stability than the first version at sustained testing speed. The cart was designed to be stable at up to 30 mph, although the maximum speed allowed by the railroad at the test site was 15 mph.

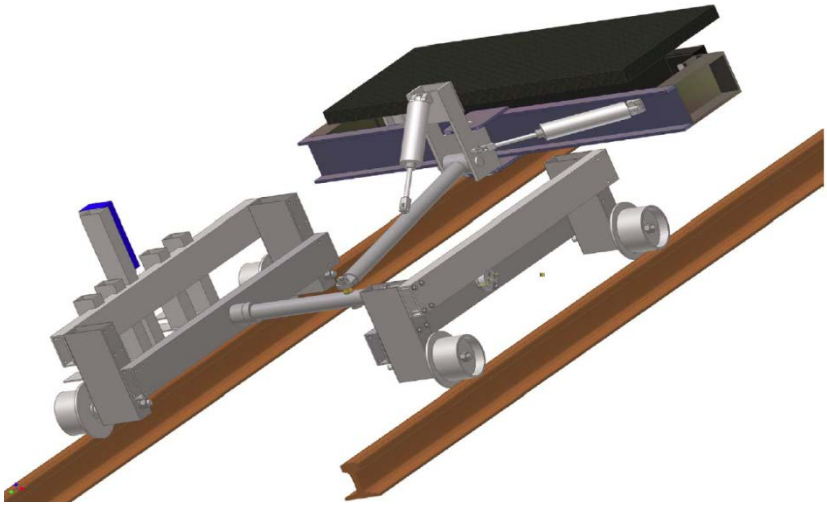

Figure 5.5. 3-D View of the Mechanical Model of the Upgraded Cart

A 3-D model of the upgraded cart is shown in Figure 5.5. As an improvement to the rigid-frame solution of the first cart, each side of the new cart is independent of the other to avoid intermittent stick-slip at sustained speeds. The side frames can rotate with respect to the center beam. Two pneumatic pistons apply forces laterally and vertically to provide, respectively, flanging ability with the gage side of the test track and overall stability of the cart.

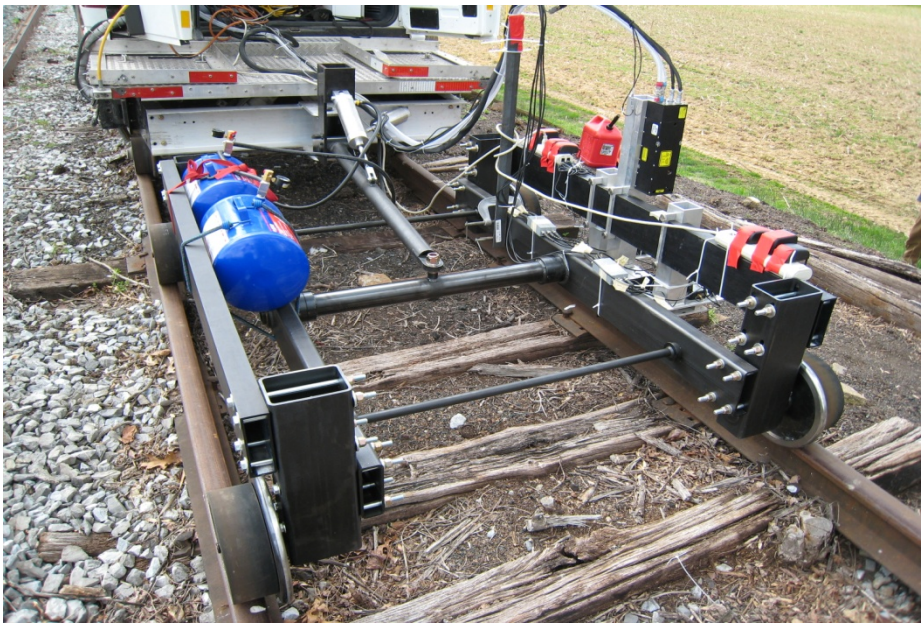

Figure 5.6. Rail Flaw Detection Prototype Installed on the Cart during Second Field Test

Compressed air tanks provide the air supply to the pistons. The connection between the swing arm and the center beam uses a spherical joint to allow for variations in cross level between the

cart and the towing vehicle. Rubber treads were installed on the wheels so as to have a smoother rolling of the cart, as well as to damp out shocks because of vertical misalignment present along the track at the joint connections. Figure 5.6 shows a picture of the prototype assembled and deployed on the track.

5.3 The New Sensor Arrangement

A new sensor arrangement was used by exploiting the bi-directionality of the laser ultrasound generation. Defect detection was achieved by computing a D.I., which was conceptually equivalent to that used previously (equation 11 in Section 3).

Another improvement consisted of the addition of two sensors to the original four to form a total of three sensing pairs (six sensors). Review of the plots showing the strain energy distribution for some propagating modes (Figure 5.4) suggests the usefulness of monitoring all sides of the head.

Besides the above three pairs, the D.I. was calculated for two extra pairs, named "cross-channel pairs." The cross channels provided additional defect detection paths that are oblique relative to the rail running direction increasing the overall head coverage. Figures 5.7 and 5.8 show the details of the three-sensor aluminum holder on one side of the laser generation. To allow for adjustments, the holder was connected to the main frame through a spherical joint; the holder also housed two lateral adjustable wings to provide the gage- and field-side sensors with an extra degree of freedom. The sensor lift-off distance was maintained at approximately 1.5 in throughout the tests.

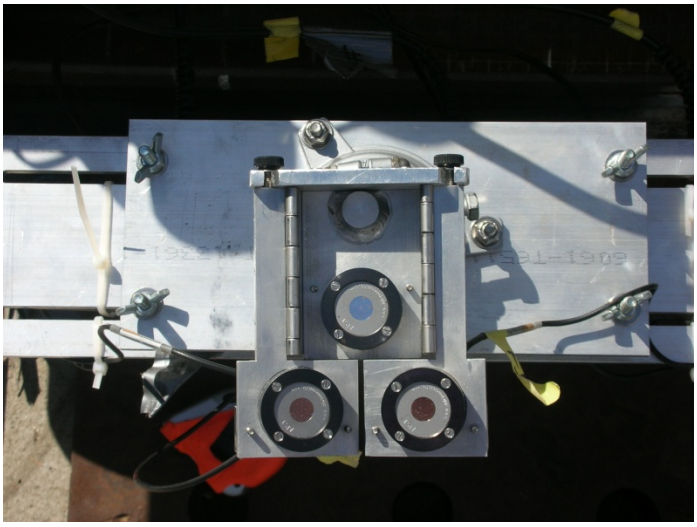

Figure 5.7. Holder for Air-Coupled Sensors Showing the Gage Side, the Center Head, and the Field Side Sensor

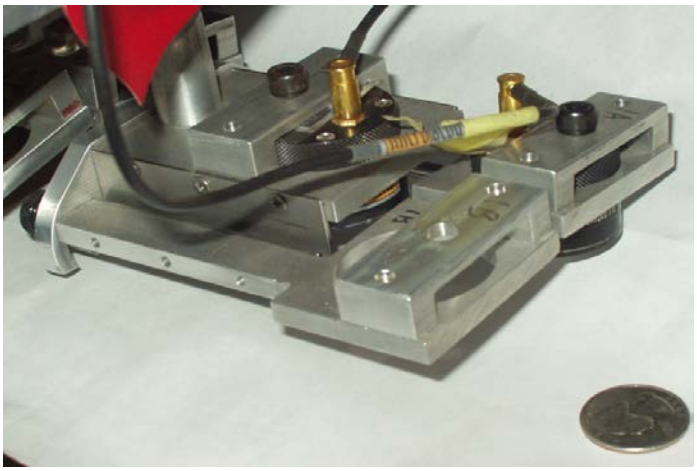

Figure 5.8. A Different View of the Sensor Holder

5.4 The Software Upgrade

A more efficient, frequency-domain filtering of the acquired signals was used through the implementation of better performing, real-time signal processing algorithms. Such improvement was needed to enable testing at subfoot spatial resolution (as low as 1 in) without loss of data. Butterworth band-pass digital filters were used to filter out unwanted noise, such as that generated by the air-shock due to the laser pulse, and other noise coming from the testing environment.

Figure 5.9 shows the block diagram of the LabView subVi performing the band-pass filtering of the measurements; on the left the input parameters, such as the low and high cutoff frequencies and the filter order, are set; on the right are filtered signals as output.

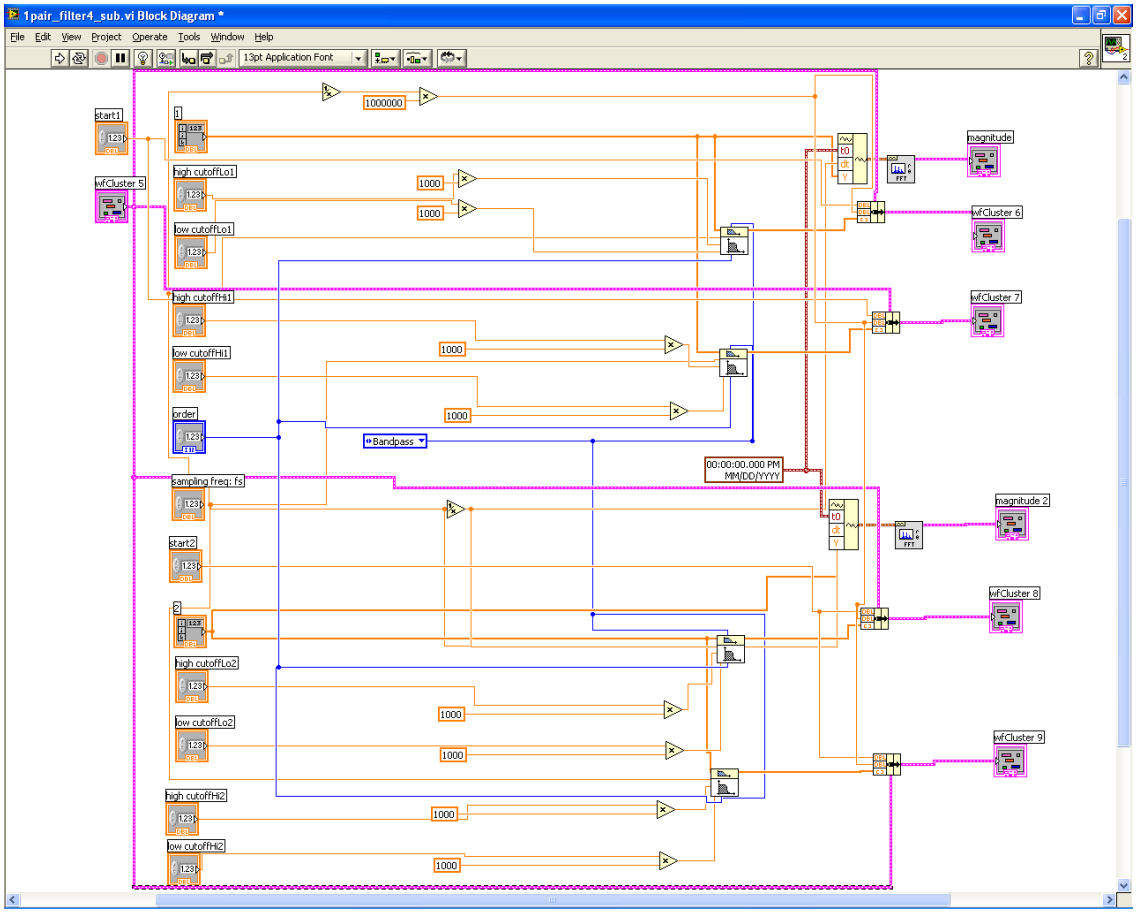

Figure 5.9. Layout of the Block Diagram of the Band-Pass Filtering subVi

Figure 5.10 shows a snapshot taken during the Calibration Session of one of the tests; the left and right sides of the screen refer, respectively, to the rear and the front sensors of a given pair (in this case one of the cross-channel pairs). For each sensor, the time-domain raw signal and its frequency content are shown; the user can set the limits of the time-domain gate and the low/high-frequency values of the band-pass filter. Two ranges of frequency can be set for the filtering, so as to allow the computation of the two L.F.-D.I. and H.F.-D.I. for defect classification.

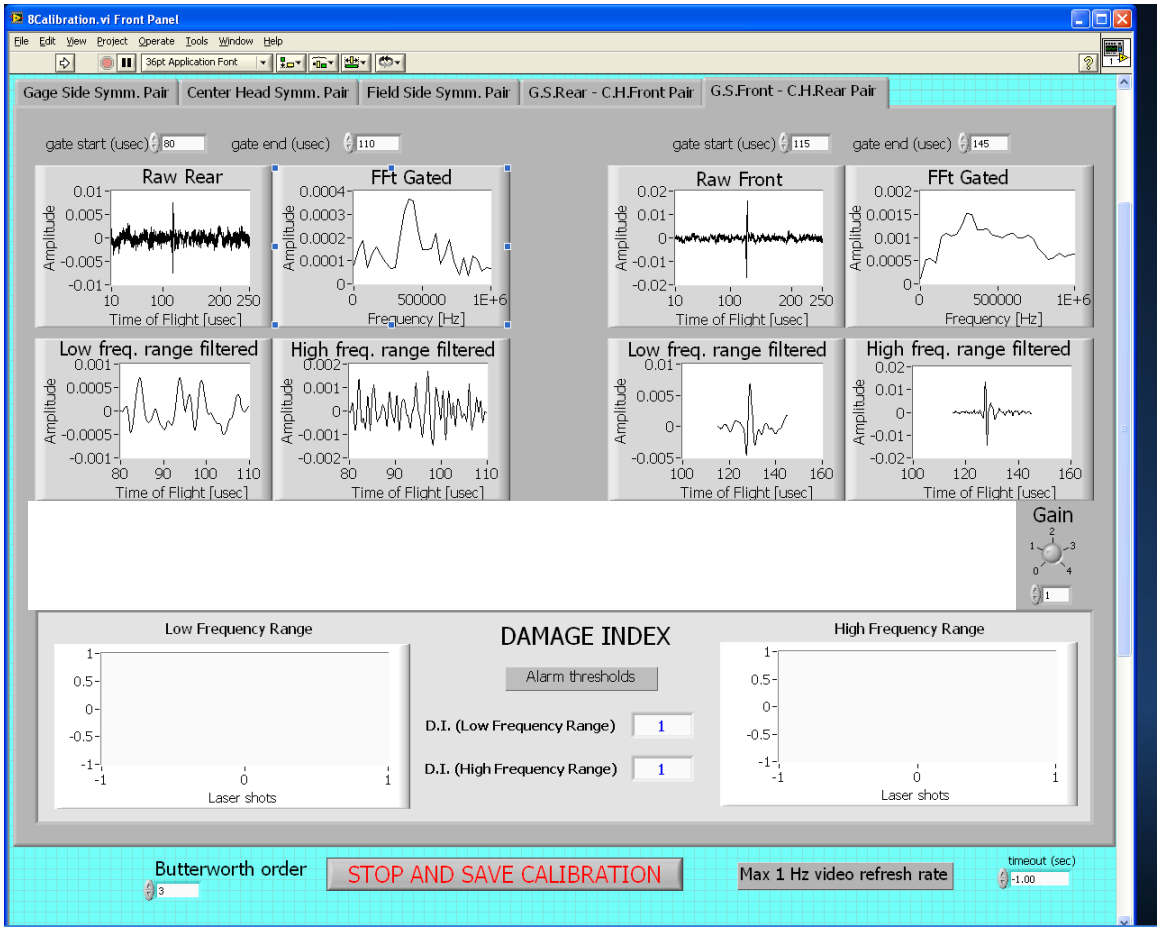

Figure 5.10. Snapshot of the Calibration Session Showing the Various Settings for the Digital Filtering of the Ultrasonic Measurements

("Raw Rear" and "Raw Front" refer to the raw waveforms acquired by the rear and front sensors, respectively.)

5.5 Summary of Second Field Test Results

The second field tests were performed during 3 days, April 24–26, 2007. Both D.I.s and raw data were collected during separate runs. The results summarized here are based only on the D.I. runs. The raw data runs were later analyzed to determine whether further signal processing routines can be beneficial to the defect detection performance of the prototype. The parameters that were varied during the tests are the following:

- condition of the rail head top surface (dry and wet);
- length of the laser line source of ultrasound (25.4, 35, and 38 mm); and
- testing speed (5, 10, and 15 mph).

Some of the recorded data was unusable due to the malfunctioning of the hy-railer track or tachometer system and partly due to the presence of an electrical interference on the signal lines. The chronology of the tests, including the description of the varied parameters, was the following:

April 24th:
Tests performed under dry conditions.
Hy-railer tack.
Total tests performed: 24
D.I. tests: 24
Raw data tests: 0
Usable damage index tests: 17
Nonusable tests: 7 due to hy-railer tack malfunctioning

April 25th:
Tests performed with under dry conditions.
Hy-railer tack.
Total tests performed: 38
D.I. tests: 38
Raw data tests: 23
Usable damage index tests: 11
Nonusable damage index tests: 7 due to hy-railer tack malfunctioning, 18 due to tack malfunctioning + electrical interference on sensors, and 3 due to check runs.

April 26th:
Tests performed with under both dry and wet conditions. UCSD tack (laser diode and reflective tape tags) used to replace hy-railer tack.
Total tests performed: 44
D.I. tests: 16
Raw data tests: 28
Usable damage index tests: 16
Nonusable damage index tests: 0

Comparing dry versus wet conditions, dry performed better. This was because the laser lens became dirty with water, and the lenses were not protected from water spraying.

The performance of the prototype was evaluated in terms of POD, as shown in Table 5.2. As with the analysis of results in the first field test (Table 4.3), the POD was calculated as the ratio between the number of runs in which a given defect was detected over the total number of applicable runs. The tests considered in this computation included only runs that (1) were "usable" (i.e., correct track or tachometer positioning and limited electrical interference) and (2) were conducted under dry conditions. Also, a defect was called detected if one of the five D.I.s was activated. A D.I. was called activated when the corresponding value was above a threshold level imposed on the measurements after the tests.

Table 5.2. Summary of Second Field Test Results (Gettysburg, PA, April 2007)

DEFECT	6" long gage chip	Surface cut (5% H.A.)	Surface cut (2% H.A.)	Internal defect (gage side, 3.6% H.A.)	Internal defect (gage side, 35% H.A.)	Oblique cut (3.5% H.A.)	Internal defect (center head, 12% H.A.)	Oblique cut (3.5% H.A.)
POSITION FROM START	56' 2"	81' 7"	82' 7.5"	86' 4"	91' 3.5"	95' 1"	96' 4"	97' 8"
POD (CUMULATIVE) *over 37 tests*	100%	84%	49%	100%	97%	58%	68%	70%
POD (5 MPH) *over 20 tests*	100%	90%	65%	100%	95%	63%	70%	90%
POD (10 MPH) *over 15 tests*	100%	80%	33%	100%	100%	60%	73%	53%
POD (15 MPH) *over 2 tests*	100%	50%	0%	100%	100%	0%	0%	0%

On the basis of these results, the following conclusions can be drawn:

1) At 5 and 10 mph, the system performed better than the walking speed tests of the first tests under the dry conditions (Table 3.3). This improvement was particularly pronounced for the IDs, all of which were detected with good rates (highest POD of 100 percent for ID 1, and lowest POD of 70 percent for ID 3).
2) Comparing 5 and 10 mph, the POD showed to be approximately independent of testing speed for almost all the defects, except for the SC 2 (2% H.A.) and the Oblique SC 2 (~3.5% H.A.) that were better detected at 5 mph.
3) At 15 mph, the gage chip and the first two IDs remained well detected, but other defects were missed. This was likely because blind spots existed at this speed because of the 8-inch gage length adopted for the sensors and the inherent 30-hertz repetition rate limit of the pulsed laser.
4) Of all defects, the second SC (2% H.A.) was the least detected probably because of its very small size and proximity to other defects.
5) Of the five sensor pairs, the field side pair gave the poorest results because of low signal-to-noise ratio of the measurements. This appeared to be the result of electrical interference at the field sensors, which was not experienced in the lab. However, the field pair was also the least relevant since all defects were located either at the center head or on the gage side.

6. Third Field Test (Gettysburg, PA, March 2008)

6.1 Prototype Upgrades

On the basis of the lessons learned in the second field test, the following upgrades were made to the prototype.

Hardware upgrades:

(a) selection of new air-coupled sensors of the "piezocomposite" type with improved ruggedness compared with the previous "capacitive" type. The piezocomposite sensors have no vibrating membrane (Figure 6.1);

(b) use of sensor arrays based on the new piezocomposite devices (Figure 6.2), which cover different frequency bands;

(c) improved compactness of the system, including electromagnetically shielded and water-tight boxes containing all sensor electronics (amplifiers, filters, etc.) and data acquisition unit (Figure 6.3-left); simplified covers for laser and sensors (Figure 6.3-right). The new covers also provided complete enclosure of the laser beam via an aluminum tube, which improved safety of standby personnel and minimized the need for wearing laser-protection glasses in close proximity to the system.

(d) rack-mounting of the laser power supply in the FRA hy-railer provided enhanced compactness and ease of use during the test.

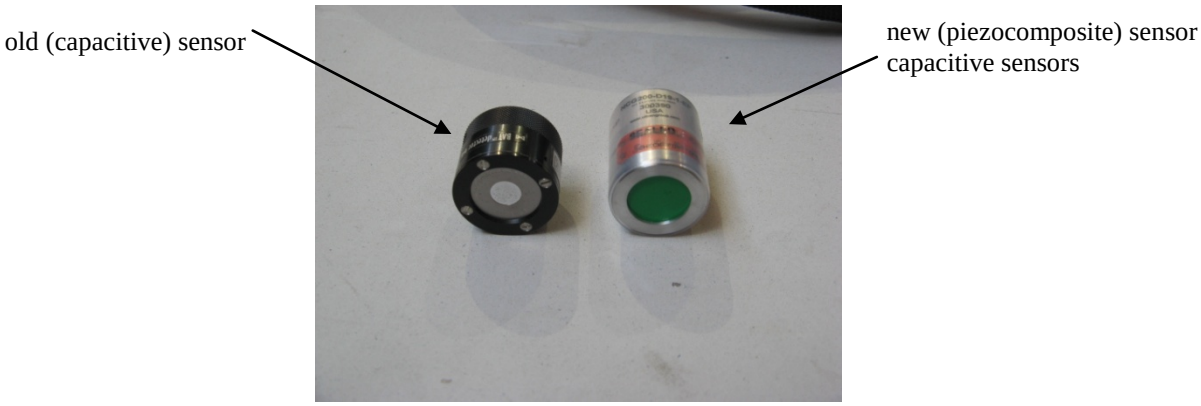

Figure 6.1. (left) Old Air-Coupled Sensor (capacitive, vibrating membrane, not waterproof); (right) New Air-Coupled Sensor (piezocomposite, no moving parts, waterproof)

Figure 6.2. Piezocomposite Sensors Arranged in an Array Configuration

Figure 6.3. (left) Water-Tight Steel Case Containing All Electronic Components Attached to the Sensing Lines; (right) Improved Covers for Laser and Sensors

Software upgrades:

(a) implementation of a statistical algorithm to analyze the ultrasonic data in place of the deterministic algorithm used previously for increased sensitivity to a defect;

(b) implementation of a defect classification routine that is based on two levels of classification. The first classification level identifies "discontinuities" in the track (including defects and joints). The second classification level flags each discontinuity as "joint," "surface defect," "ID," or "unclassified defect." The two-level classification

was implemented to minimize the chances of missing a defect (i.e., minimizing false negatives) and, at the same time, to provide the defect classification ("surface defect" vs. "ID") whenever possible. The classification algorithm relies on the analysis of the measurements at different frequency bands based on the theory of guided wave propagation;

(c) simplification of the software's user-interface, which features three different windows, namely a "Defect Detection" window with the discontinuities and classification results shown as color-coded points, an "Index Number" window with the index number plots for the high and the low frequencies, and a "Report" window with a table containing the type and position of the defects found. The results can also be saved as ASCII files for subsequent analysis. Figure 6.4 shows an example of the "Defect Detection" window during one of the test runs at the Gettysburg site.

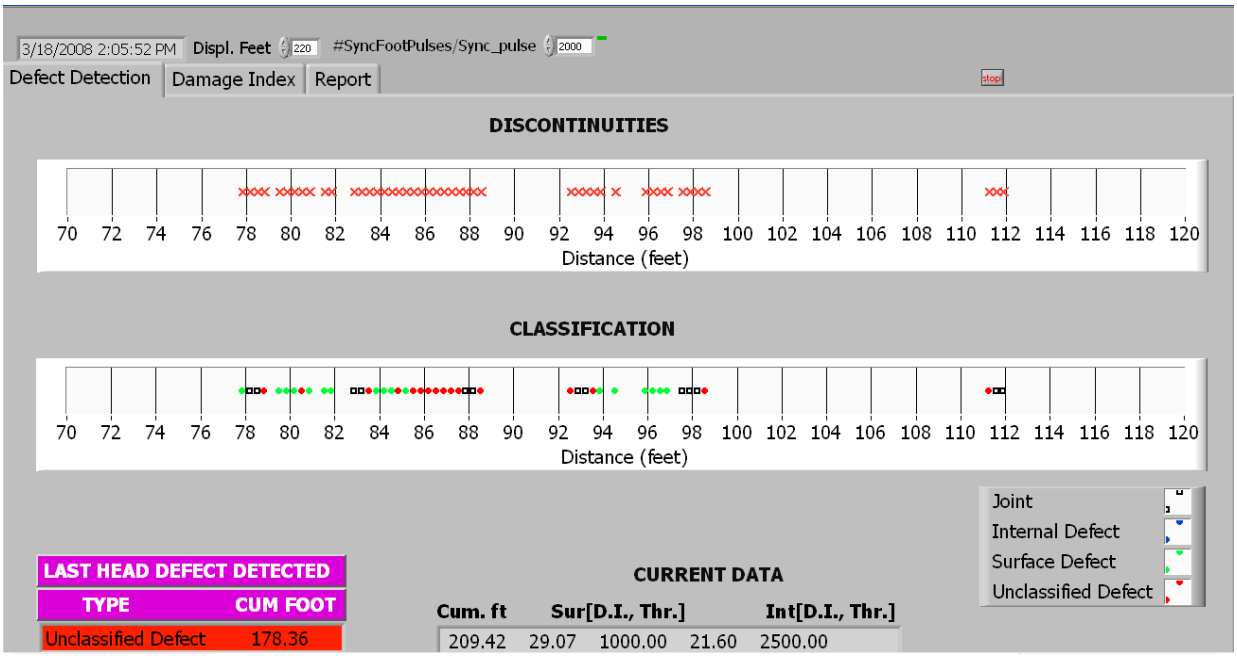

Figure 6.4. Snapshot of the "Defect Detection" Window of the Prototype Software Showing the "Discontinuities" Plot and the Color-Coded "Classification" Plot between Test Positions 70- and 120-Feet at the Gettysburg Site

6.2 Summary of the Third Field Test Results

The third field test was performed during 4 days, March 17–20, 2008. Table 6.1 describes the layout of the test site. An improvement over the previous two tests was the replacement of some of the joint bars with straps. The replaced joint bars were originally too high, causing the cart wheels to lose contact with the rail head.

Table 6.1. Gettysburg Site Layout for Third Field Test (March 2008)

Gettysburgh Test Site Lay-out (UCSD/FRA Rail Flaw Detection - 3/19/2008)

Location	Foot	Inches	Description
1	0	0	Start of Test Zone
2	13	3	Joint
3	32	0	Chip on gage side of rail head
4	46	3.5	Joint - Orange paint
5	52	5	Large chip (6" long) on gage side of rail head
6	56	2	Large chip (6" long) on gage side of rail head
7	78	9	Flaking on gage side of rail head
8	79	3.5	Joint - flaking on gage side of rail head at joint
9	81	7	Cut surface transverse notch 4mm depth, 50 mm length (~5% H.A)
10	82	7.5	Cut surface transverse notch 2mm depth, 25 mm length (~2% H.A)
11	84	5	Joint - Rail head change 1/2in gap
12	85	6	Beginning 1st high joint bar (height fixed)
13	86	4	Internal transverse defect (3.5% H.A.)
14	87	3.5	Beginning 2nd high joint bar (height fixed)
15	88	2	Welded ramp to match rail sizes
16	88	9.5	Joint
17	90	3.5	End 2nd high joint bar (height fixed)
18	91	3.5	Internal transverse defect (35% H.A.)
19	93	10	Joint - 1/2 in gap
20	95	1	Cut surface oblique (+45deg) notch 3mm depth, 30mm length (~3.5% H.A)
21	96	4	Internal transverse defect (12% H.A.)
22	97	8	Cut surface oblique (-45deg) notch 3mm depth, 30mm length (~3.5% H.A)
23	98	9	Joint - Rail head change 1/2in gap
24	99	5	Flaking on gage side of rail head
25	103	0	Chip on gage side of rail head
26	106	7	Flaking chip on field side of rail head
27	112	3	Joint
28	121	0	Flaking chip on field side of rail head
29	126	8	Flaking chip on field side of rail head
30	145	3	Joint
31	146	4	Beginnin flaking (severe) on gage side of rail head (continuous)
33	161	0	End flaking (severe) on gage side of rail head (continuous)

Both index numbers and raw data were collected for various runs. The results summarized here are only based on the index number runs. The raw data runs were analyzed to identify any further improvements to the signal processing algorithm. It was determined that the features used in the processing of the test runs were indeed optimized.

The parameters that varied during the tests include:

(a) weather conditions (calm, dry, wind, rain);
(b) condition of the rail head surface (dry and wet);
(c) laser power (50–70 percent of maximum power); and
(d) testing speed (5 and 10 mph).

The statistical processing algorithm proved robust against the changing parameters above. The presence of a mechanical noise was felt on the low-frequency sensors, and it was partially isolated during the last day of testing by using rudimentary rubber links. This noise seemed not to affect the high-frequency sensors. The results of two runs were discarded because of the loosening of an aluminum holder that caused a sensor array to move from its fixed position. The loose link was tightened for the remaining tests.

The test schedule was as follows:

March 17th:
Cloudy, dry conditions
Total tests performed: 4
Index number tests: 4
Usable index number test: 4
Raw data tests: 0

March 18th:
Cloudy, light rain, dry, and wet conditions
Total tests performed: 6
Index number tests: 6
Usable index number tests: 6
Raw data tests: 0

March 19th:
Rainy, wet conditions
Total tests performed: 12
Index number tests: 12
Usable index number tests: 12
Raw data tests: 0

March 20th:
Sunny and windy, dry conditions
Total tests performed: 41
Index number tests: 32
Usable index number tests: 30
Unusable index number tests: 2, because of loosening of a sensor holder
Raw data tests: 9

The performance of the prototype was evaluated in terms of POD and summarized in Table 6.2. The results are shown separately for the 5- and the 10-mile per hour testing speeds. The "cumulative" POD, obtained by considering all tests regardless of testing speed, is also shown.

As with the analysis of results in the 2007 field test, the POD was calculated as the ratio between the number of runs in which a given defect was detected over the total number of applicable runs. The tests considered in this computation included only the "usable" runs. A defect was considered detected when either one of the two statistical index numbers (low and high frequency) was activated. A statistical index number was called "activated" when the corresponding value was above a fixed threshold level.

Table 6.2. Defect Detection Reliability during Third Field Test (Gettysburg, PA, March 2008)

Defect	Surface cut (5% H.A)	Surface cut (2% H.A)	Internal defect (gage side, 3.6% H.A.)	Internal defect (gage side, 35% H.A.)	Oblique cut (3.5% H.A.)	Internal defect (center head, 12% H.A.)	Oblique cut (3.5% H.A.)	
POSITION FROM START	81'_7"	82'_7.5"	86'_4"	91'_3.5"	95'_1"	96'_4"	97'_8"	False positive %
POD (5 MPH)	**100.0**	**97.7**	**100.0**	**81.8**	**95.5**	**84.1**	**100.0**	0.8
POD (10 MPH)	**100.0**	**100.0**	**100.0**	**100.0**	**75.0**	**87.5**	**100.0**	2.9
POD (Cumulative)	**100.0**	**98.1**	**100.0**	**84.6**	**92.3**	**84.6**	**100.0**	1.1

The following conclusions can be drawn:

1) Comparing the POD values obtained in the third field tests to those obtained in the second field tests of April 2007, substantial reliability improvements were obtained for all of the defects listed. Noteworthy is the good performance in detecting all three IDs, particularly the 12% H.A. at 96'4", which proved harder to detect in the previous tests. Improvements were also seen in the other defects, including the 2% H.A. SC and the two 3.5% H.A. oblique cuts.

2) Comparing the results at 5- and 10-mile per hour testing speeds, except for one of the 3.5% H.A. oblique cuts, the performance was equal or better at the larger 10-mile per hour speed. This was the result of the mechanical noise being reduced by the rubber links.

3) The low false-positive indications (last column of Table 6.2) are also reassuring because false positives would require an inspector to manually verify the indication in the "stop and confirm" mode. The rate of false-positive indications was not shown in the second field test report. Here the false positives were calculated as the percentage ratio between the sum of false-positive detections over all the runs and the total number of the readings, excluding the ones related to the discontinuities (joints and defects).

4) It was also reassuring to determine that the high reliability of defect detection was maintained within the large range of environmental conditions encountered, including rain and wind. This enhanced stability was the result of the improved sensors and the new processing algorithm.

5) The mechanical noise affecting the low-frequency sensors was not completely eliminated during the tests. The final design of the system will have to incorporate vibration isolators to deal with this problem.

6) Under wet conditions, water splashing on the optical lenses was still an issue. The final design of the system will have to incorporate a small slit at the laser illumination point plus forced air circulation to prevent water from entering the lens housing.

7) Alignment of the sensors was still required during the tests. The final design will have to use a more compact platform with minimal adjustments.

Figures 6.5 and 6.6 show the processed data for two of the individual runs, separated into two plots, showing “Index Number” and “Discontinuity” traces. The top “Index Number” plot shows each statistical index number as a function of position. The joints and defects correspond to jumps in the index number plots. The joint jumps are much higher than the defects. For clarity of presentation, only the largest of the low-frequency index number and the high-frequency index number is plotted. The bottom “Discontinuities” plot separates the indications of the defects (vertical lines) from those of the joints (triangles). This separation is readily obtained from the statistical analysis because the index number for a joint is much larger than that for a defect.

Table 6.3 contains detailed data for each run, indicated separately for the 5- and the 10-mile per hour testing speeds.

Figure 6.5. Index Number and Discontinuity Plot Run #2

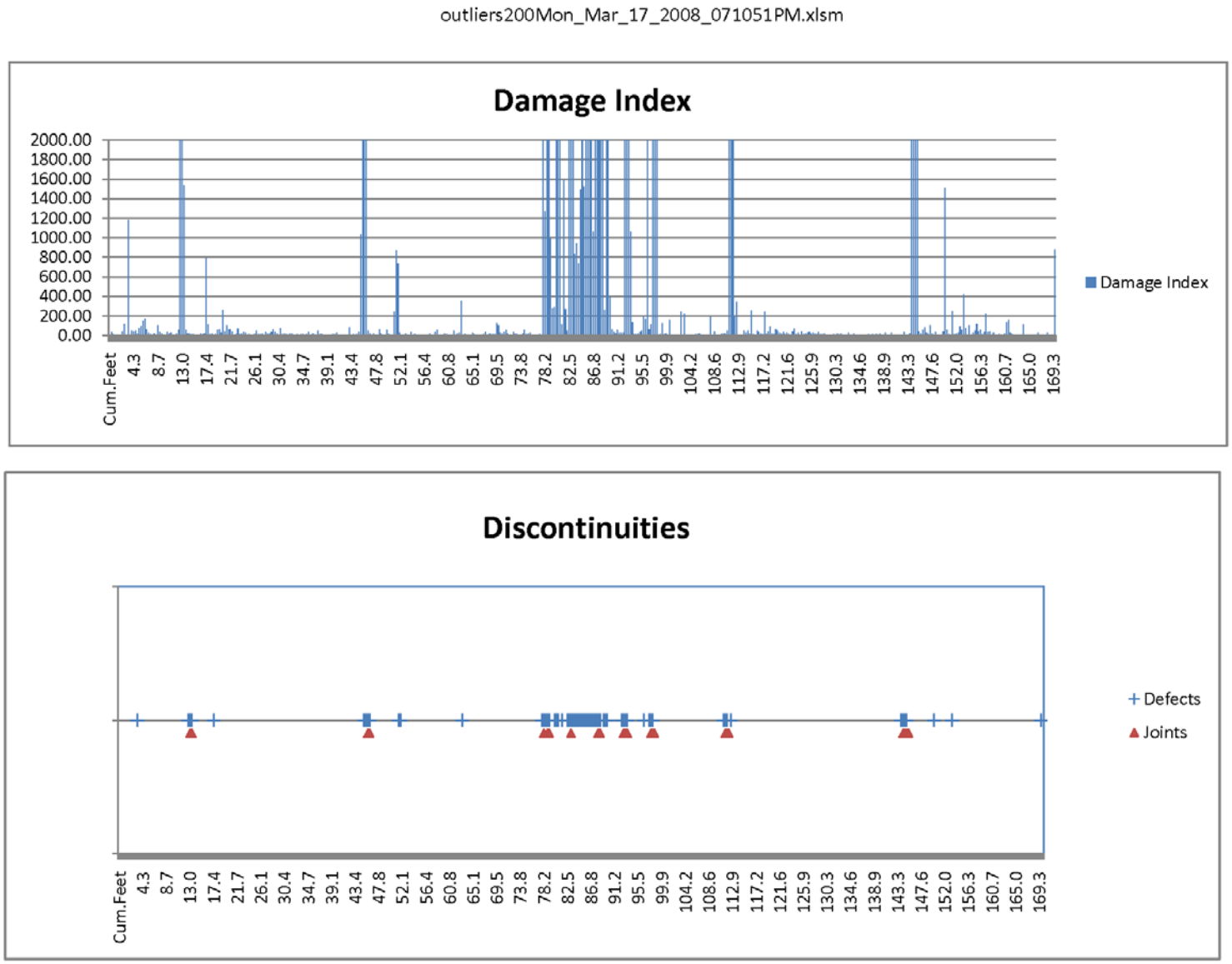

Figure 6.6. Index Number and Discontinuity Plot Run #3

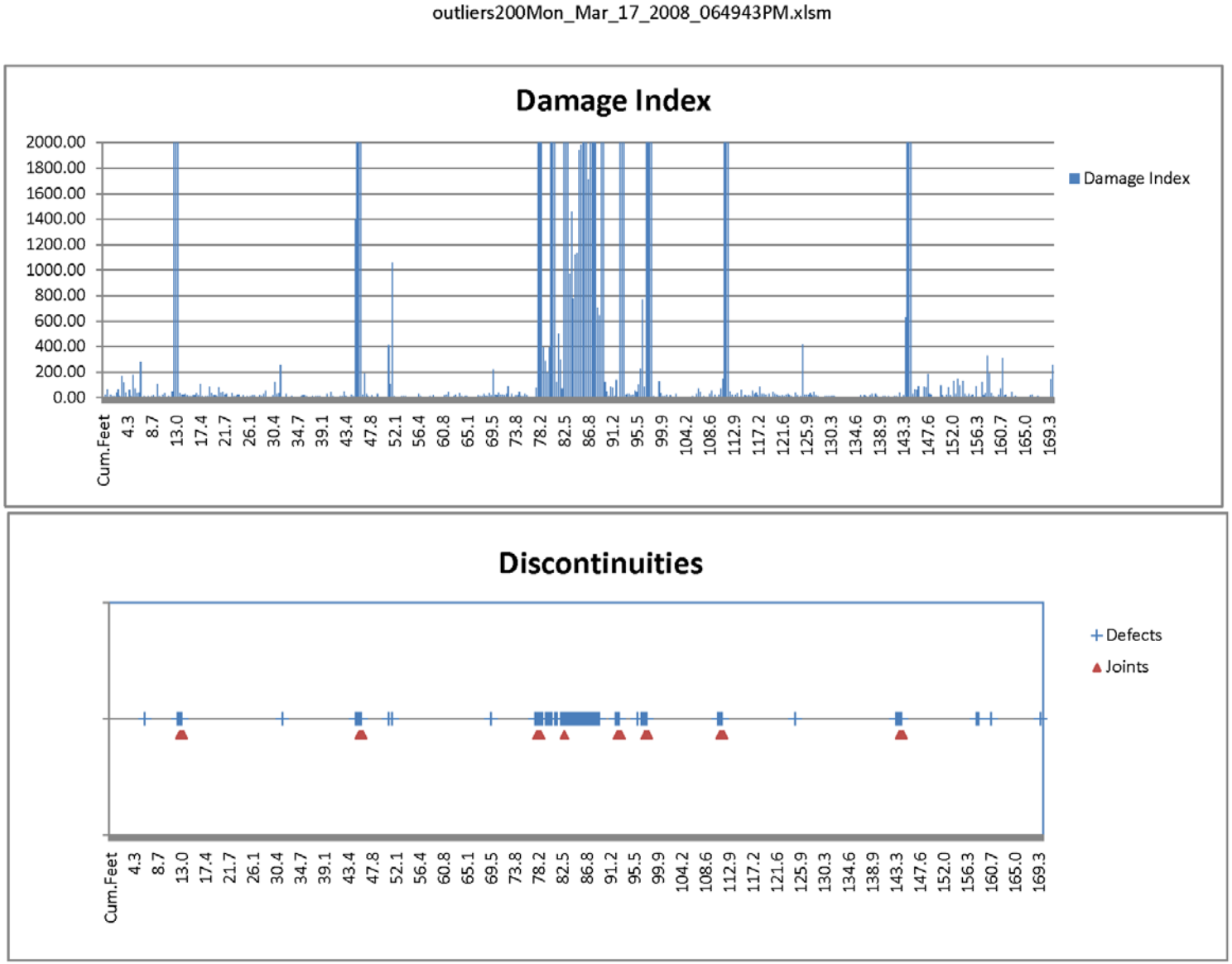

Table 6.3. Details of Third Field Test Runs (Gettysburg, PA, March 2008)

Inspection speed	5 MPH																			
Test#	Test name on file	Weather	L. Chip [32"]	L. Chip [52'_5"]	Chip [56'_2"]	S.C. 5% [81'_7"]	S.C. 2% [82'_7.5"]	I.D. 4% [86'_4"]	I.D. 35% [91'_3.5"]	O.C. 3.5% [95'_1"]	I.D. 12% [96'_4"]	O.C. 3.5% [97'_8"]	Chip [103']	Flaking [106'_7"]	Flaking [121']	Flaking [126'_8"]	S.C. <3% [158']	False positives	Joints
1	outliers200Mon_Mar_17_2008_064507PM.xls	Cloudy	1	1	1	1	1	1	1		1	1					1	2	9
2	outliers200Mon_Mar_17_2008_064943PM.xls	Cloudy	1	1		1	1	1	1			1				1	1	0	8
3	outliers200Mon_Mar_17_2008_071051PM.xls	Cloudy		1	1	1	1	1	1	1	1	1	1	1			1	6	9
4	outliers200Mon_Mar_17_2008_071812PM.xls	Cloudy		1	1	1	1	1	1	1		1					1	3	9
5	outliers200Tue_Mar_18_2008_010758PM.xls	Cloudy				1	1	1	1	1	1	1	1	1			1	5	9
6	outliers200Tue_Mar_18_2008_015711PM.xls	Cloudy	1	1		1	1	1	1	1	1	1	1	1		1	1	4	9
7	outliers200Tue_Mar_18_2008_021933PM.xls	Light Rain	1	1	1	1	1	1	1	1	1	1	1		1	1	1	8	9
8	outliers200Tue_Mar_18_2008_033828PM.xls	Light Rain		1		1	1	1	1	1	1	1	1				1	5	9
9	outliers200Tue_Mar_18_2008_034429PM.xls	Light Rain	1			1	1	1	1	1	1	1	1			1	1	7	9
10	outliers200Tue_Mar_18_2008_035848PM.xls	Light Rain	1			1	1	1	1	1	1	1	1				1	1	9
11	outliers200Wed_Mar_19_2008_032053PM.xls	Rain	1			1	1	1	1	1	1	1						3	9
12	outliers200Wed_Mar_19_2008_060107PM.xls	Rain	1	1		1	1	1	1	1	1	1	1					2	9
13	outliers200Wed_Mar_19_2008_060434PM.xls	Rain				1	1	1	1	1	1	1						1	9
14	outliers200Wed_Mar_19_2008_060650PM.xls	Rain		1		1	1	1	1	1	1	1						0	9
15	outliers200Wed_Mar_19_2008_061309PM.xls	Rain				1	1	1	1	1	1	1						0	9
16	outliers200Wed_Mar_19_2008_061504PM.xls	Rain			1	1	1	1	1	1	1	1						1	9
17	outliers200Wed_Mar_19_2008_061908PM.xls	Rain		1		1	1	1	1	1	1	1						1	9
18	outliers200Wed_Mar_19_2008_062130PM.xls	Rain		1		1	1	1	1	1	1	1						1	9
19	outliers200Wed_Mar_19_2008_062411PM.xls	Rain		1		1	1	1	1	1	1	1						2	9
20	outliers200Wed_Mar_19_2008_062557PM.xls	Rain		1		1	1	1	1	1	1	1						0	9
21	outliers200Wed_Mar_19_2008_063105PM.xls	Rain		1		1	1	1	1	1	1	1						1	9
22	outliers200Wed_Mar_19_2008_063421PM.xls	Rain		1		1		1	1	1	1	1						2	9
23	outliers200Thu_Mar_20_2008_010950PM.xls	Sunny+Gusty wind				1	1	1	1	1	1	1			1			1	9
24	outliers200Thu_Mar_20_2008_011458PM.xls	Sunny+Gusty wind	1			1	1	1	1	1	1	1		1	1			1	9
25	outliers200Thu_Mar_20_2008_012111PM.xls	Sunny+Gusty wind	1	1		1	1	1		1	1	1				1		1	9
26	outliers200Thu_Mar_20_2008_013309PM.xls	Sunny+Gusty wind	1			1	1	1	1	1	1	1	1		1			5	9
27	outliers200Thu_Mar_20_2008_021157PM.xls	Sunny+Gusty wind				1	1	1	1	1	1	1			1			4	9
28	outliers200Thu_Mar_20_2008_021546PM.xls	Sunny+Gusty wind	1	1		1	1	1		1	1	1					1	2	9
29	outliers200Thu_Mar_20_2008_022149PM.xls	Sunny+Gusty wind		1		1	1	1	1	1	1	1				1		3	9
30	outliers200Thu_Mar_20_2008_022732PM.xls	Sunny+Gusty wind	1	1		1	1	1	1	1	1	1				1		3	9
31	outliers200Thu_Mar_20_2008_023232PM.xls	Sunny+Gusty wind	1			1	1	1	1	1	1	1		1	1	1		3	9
32	outliers200Thu_Mar_20_2008_024110PM.xls	Sunny+Gusty wind	1			1	1	1	1	1	1	1		1				3	9
33	outliers200Thu_Mar_20_2008_035121PM.xls	Sunny+Gusty wind	1			1	1	1		1		1		1	1	1		5	9
34	outliers200Thu_Mar_20_2008_035452PM.xls	Sunny+Gusty wind	1	1		1	1	1	1	1	1	1			1	1		5	9
35	outliers200Thu_Mar_20_2008_035942PM.xls	Sunny+Gusty wind	1	1		1	1	1	1	1	1	1				1		2	9
36	outliers200Thu_Mar_20_2008_042129PM.xls	Sunny+Gusty wind		1		1	1	1		1	1	1				1		7	9
37	outliers200Thu_Mar_20_2008_042324PM.xls	Sunny+Gusty wind	1	1	1	1	1	1		1	1	1			1	1		6	9
38	outliers200Thu_Mar_20_2008_042553PM.xls	Sunny+Gusty wind	1	1	1	1	1	1	1	1		1		1	1	1		9	9
39	outliers200Thu_Mar_20_2008_045130PM.xls	Sunny+Gusty wind	1	1		1	1	1		1		1			1	1		2	9
40	outliers200Thu_Mar_20_2008_051151PM.xls	Sunny+Gusty wind				1	1	1		1	1	1	1		1	1		7	9
41	outliers200Thu_Mar_20_2008_051840PM.xls	Sunny+Gusty wind	1			1	1	1	1	1	1	1			1	1		3	9
42	outliers200Thu_Mar_20_2008_052232PM.xls	Sunny+Gusty wind			1	1	1	1	1	1		1	1	1	1	1		9	9
43	outliers200Thu_Mar_20_2008_052442PM.xls	Sunny+Gusty wind	1			1	1	1		1		1			1	1		4	9
44	outliers200Thu_Mar_20_2008_052654PM.xls	Sunny+Gusty wind	1	1		1	1	1	1	1	1	1		1	1	1		4	9
		Tot.	24	26	8	44	43	44	36	42	37	44	11	10	16	20	11	144	395
		POD	**54.5**	**59.1**	**18.2**	**100.0**	**97.7**	**100.0**	**81.8**	**95.5**	**84.1**	**100.0**	**25.0**	**22.7**	**36.4**	**45.5**	**25.0**	**3.3**	**99.7**
																	FP	**0.008**	
Inspection speed	**10 MPH**																		
Test#	**Test name on file**	**Weather**	**L. Chip [32"]**	**L. Chip [52'_5"]**	**Chip [56'_2"]**	**S.C. 5% [81'_7"]**	**S.C. 2% [82'_7.5"]**	**I.D. 4% [86'_4"]**	**I.D. 35% [91'_3.5"]**	**O.C. 3.5% [95'_1"]**	**I.D. 12% [96'_4"]**	**O.C. 3.5% [97'_8"]**	**Chip [103']**	**Flaking [106'_7"]**	**Flaking [121']**	**Flaking [126'_8"]**	**S.C. <3% [158']**	**False positives**	**Joints**
45	outliers200Thu_Mar_20_2008_025001PM.xls	Sunny+Gusty wind	1		1	1	1	1	1	1	1	1			1	1	1	0	9
46	outliers200Thu_Mar_20_2008_025652PM.xls	Sunny+Gusty wind	1			1	1	1	1	1	1	1			1	1	1	5	9
47	outliers200Thu_Mar_20_2008_025953PM.xls	Sunny+Gusty wind	1	1	1	1	1	1	1		1	1	1	1	1		1	9	9
48	outliers200Thu_Mar_20_2008_030112PM.xls	Sunny+Gusty wind	1			1	1	1	1	1	1	1	1		1	1	1	6	9
49	outliers200Thu_Mar_20_2008_030343PM.xls	Sunny+Gusty wind	1		1	1	1	1	1	1	1	1		1		1	1	19	9
50	outliers200Thu_Mar_20_2008_030729PM.xls	Sunny+Gusty wind	1		1	1	1	1	1	1	1	1	1	1		1	1	11	9
51	outliers200Thu_Mar_20_2008_034833PM.xls	Sunny+Gusty wind	1	1		1	1	1	1	1	1	1			1	1		4	9
52	outliers200Thu_Mar_20_2008_052045PM.xls	Sunny+Gusty wind	1	1	1	1	1	1	1			1	1	1				2	9
		Tot.	8	3	5	8	8	8	8	6	7	8	4	4	5	6	6	56	72
		POD	**100.00**	**37.50**	**62.50**	**100.00**	**100.00**	**100.00**	**100.00**	**75.00**	**87.50**	**100.00**	**50.00**	**50.00**	**62.50**	**75.00**	**75.00**	**7.00**	**100.00**
																	FP	**0.029**	
		Cumulative POD	**61.54**	**55.77**	**25.00**	**100.00**	**98.08**	**100.00**	**84.62**	**92.31**	**84.62**	**100.00**	**28.85**	**26.92**	**40.38**	**50.00**	**32.69**	**3.846**	**99.79**
																	FP	**0.011**	

7. Fourth Filed Test (Gettysburg, PA, December 2008)

7.1 Prototype Upgrades

The following upgrades were made to improve the prototype in light of the results of the third field test:

1) A higher performing laser model was procured, potentially capable of achieving testing speeds in excess of 40 mph.
2) The software was fully migrated from a regular NI LabVIEW environment to an NI LabVIEW "Real-time" environment to satisfy the computational requirements of the higher inspection speed.
3) The system was packaged into a compact shoe, with one mounting point for a holder mechanism on a test car. The shoe mount consists of a main holder for the laser head, optical elements, and an air knife plus transducer holders. The purpose of the air-knife device is to force a constant airflow through the laser beam path to prevent water, dirt, and dust from reaching the optical elements. The shoe itself was connected to its supporting arm through mechanically isolating cup-mount holders.

The electronic components were housed in a metal box positioned on the outdoor deck of R-4. The system included a breakout box, which connected the shielded multichannel cable coming from the metal box to the acquisition unit located inside the Hy-Railer. The breakout box is depicted in Figure 7.1, along with the PXI unit, which hosted the software for the real-time acquisition and processing of the ultrasonic signals.

Figure 7.1. Breakout Box and PXI Unit; the Box Is Connecting the Sensor Lines to the PXI Data Acquisition Unit

The laser beam path is currently fully enclosed by the prototype cover, shown in Figure 7.2, eliminating laser irradiation to the surrounding environment as a safety precaution.

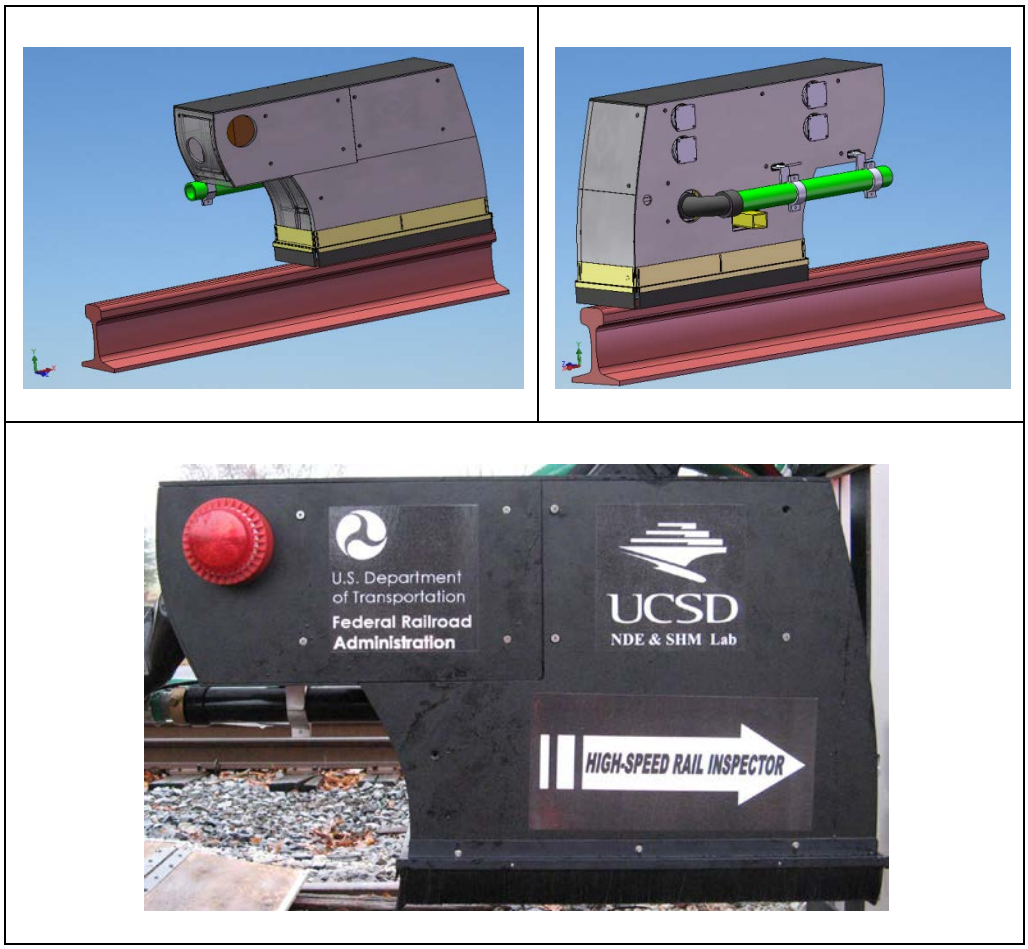

Figure 7.2. (top) 3-D Models of the Prototype Cover; (bottom) Prototype Cover, Containing Laser Head and Optical Components and Fully Enclosing the Laser Beam from the Exterior; a Flashing-Buzzing Warning Device Is Activated during Inspection Operations

4) A servo-controlled mount (Figure 7.3) was designed by ENSCO to keep the prototype at a constant position relative to the rail head.

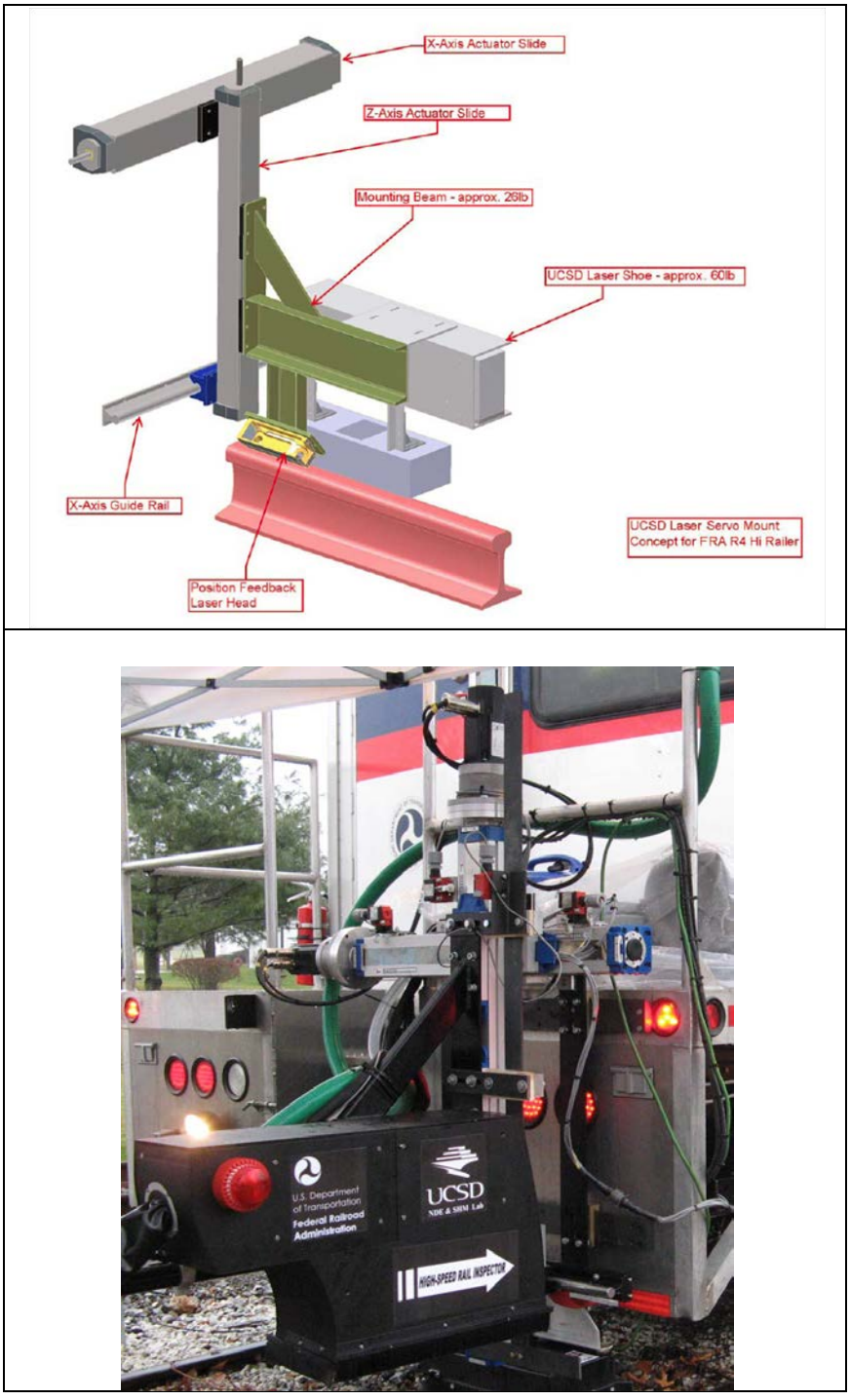

Figure 7.3. (top) 3-D Model of the Servo-Arm Designed by ENSCO; (bottom) Servo-Arm Installed on R-4, Supporting the Shoe-Prototype

The specifications of the servo-motors are summarized in Tables 7.1 and 7.2, as reported by ENSCO.

Table 7.1. Technical Specification of Slides and Guide of the Servo-Mechanism

Axis	Drive Type	Guide Type	Drive Size [in]	Speed [ft/s]*	Resolution [in]	Repeatability [in]
X (actuated)	Ball Screw	Ball	Ø: 1in Lead: 1in/rev	1.24	0.008	0.004
X (guide rail)	N/A	Ball	Ø: 1in	See above	N/A	N/A
Z (actuated)	Ball Screw	Ball	Ø:0.787in Lead: 0.787in/rev	1.24	0.008	0.002

*-Speed based on servo motors. Max. speed of slides is 16ft/s.

Table 7.2. Load Bearing Capacities of Slides and Guides of the Servo-Mechanism

Axis	Max. Normal Load F_Y [lbs]	Max. Thrust F_a [lbs]	Max. Torque M_a [lbf.in]	Max. Torque M_x [lbf.in]
X (actuated)	1100	1100	3540	477
X (guide rail)	1500	1500 (Side Load)	-	-
Z (actuated)	660	550	3317	159

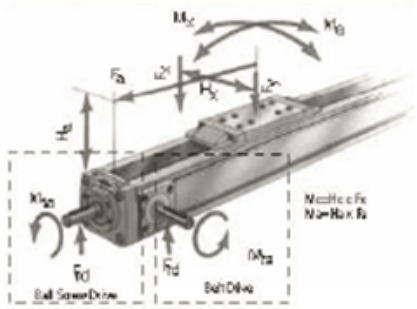

These specifications were to fulfill the requirements of not exceeding a maximum tolerance of 1/8 inch in the horizontal and vertical displacement of the arm.

7.2 Summary of Fourth Field Test Results

The fourth field test was performed between December 4 and 13, 2008, for a total of 10 days. The first 6 days were spent at ENSCO in Springfield, VA, addressing hardware problems of the

shoe-prototype interfacing the servo-arm. The last 4 days were spent in the field at the Gettysburg testing location. During the initial days spent in Springfield, VA, UCSD and ENSCO personnel worked at troubleshooting the problems encountered while interfacing the shoe with the servo-arm. Power issues, electromechanical limitations of the servo-mechanism, and electrical noise problems did not allow for any *Defect Detection* runs during the field test.

On the last day spent in Gettysburg, several *Raw Data Test* runs were performed, with the servo-arm enabled only for the horizontal direction, with no vertical adjustment. Useful information was extracted by the analysis of the *Raw Data Test* run, which are reported here in detail. The outcome of the tests is summarized below as a bullet-point list, identifying UCSD, ENSCO, and collaborative action items:

UCSD responsibility items:

- Optical components (laser + lenses) in the new design of prototype shoe performed as designed.
- Air-coupled transducer components and mounts performed as designed. Particularly comforting was the successful mitigation of mechanical vibrations owing to new mounts for sensor holders.
- The real-time processing software performed as designed.
- The air-knife system performed well in keeping the lenses clean from dirt and water ejected from laser irradiation of the rail head.
- The sensor electrical lines and electrical junction box were not sufficiently shielded to isolate the system from external electrical noise sources (common ground was used across all lines). Electrical noise was picked up by the system both at the sensor lines and at the positioning sync-pulse lines.

ENSCO responsibility items:

- The servo-motor was successfully operated for horizontal adjustment. The servo-log data containing information on the servo-positioning precision showed that the 1/8-inch tolerance was maintained at walking speed on a straight path of the rail, whereas "outliers" were detected at 5 and 10 mph on a straight path and at walking speed along a curved path. Since the sensor determining the servo-arm position was located on R-4 frame, this tolerance value was deducted arithmetically considering the relative position of the arm and R-4, as provided by the servo-encoder.
- The servo-motor for vertical adjustment could not be operated because of electromechanical problems.
- The arm on which the prototype shoe was mounted had too much play in the horizontal direction while it looked stable on the vertical direction.
- Electrical elements driving the servo-motors (amplifiers) were causing a high electromagnetic interference (EMI), which was picked up by the air-coupled sensors. Part of the EMI was present on the power line, and part was transmitted through the air with motors acting as "transmitting antennas."

- The electronic board handling the sync-pulse positioning line was not sufficiently shielded.

UCSD and ENSCO joint-responsibility items:

- Testing of the new laser (for ~40 mph speed) was not possible because the correct supply power to this laser was not available. Attempts to power this new laser with an external generator plus phase converter (laser requires three-phase supply) caused electrical components in laser power supply to blow up. The new laser was later repaired by the manufacturer.
- UCSD and ENSCO provided different specific components to the system; at this level of the design, interfacing the different parts together was challenging, but many lessons were learned in the process.

Because of the troubleshooting efforts indicated above, Ultrasonic Data Acquisition Runs were only collected during the day of December 12 with the following specifics:

December 12:
Cloudy, dry conditions
Total tests performed: 13
Raw Data tests: 13
Damage Index tests: 0
Usable Raw Data Test: 11

Details of the runs are reported in Table 7.3.

Table 7.3. Details of Fourth Field Test Runs

Test Progressive Number	Date - Time	Power Laser [%]	Speed [MPH]	Air knife	Horizonal Motor [Volt]	Vertical Motor [Volt]	Sync-foot resolution [in]	Notes	Tac-system	Notes
1	12/12/2009 14:12	100	Walking Speed	Off	110	Off	12	Servo Calibration	N/A	
2	12/12/2009 14:22	100	Walking Speed	Off	110	Off	12	Servo Calibration	N/A	
3	12/12/2009 14:32	100	Walking Speed	Off	110	Off	12	Servo Calibration	N/A	
4	12/12/2009 14:48	100	Walking Speed	Off	110	Off	12	Waveform acquisition (190)	Ok	
5	12/12/2009 14:57	100	5	Off	110	Off	12	Waveform acquisition (228)	Ok	
6	12/12/2009 15:48	100	5	Off	110	Off	12	Waveform acquisition (0)	Ok	Stopped earlier. No data saved
7	12/12/2009 15:51	100	5	Off	110	Off	12	Waveform acquisition (264)	Ok	265-360 ft, only servodata recorded going back
8	12/12/2009 16:02	100	Walking Speed	Off	110	Off	12	Waveform acquisition (98)	Ok	
9	12/12/2009 16:10	100	10	Off	110	Off	12	Waveform acquisition (660)	Electrical noise	~400 ft at 10 MPH ~260 ft at walking speed
10	12/12/2009 16:19	100	Walking Speed	Off	110	Off	12	Waveform acquisition (132)	Ok	Starting point is the end of previous test
11	12/12/2009 16:30	100	10	Off	110	Off	12	Waveform acquisition (321)	Electrical noise	
12	12/12/2009 17:08	100	5	On	110	Off	12	Waveform acquisition (218)	Ok	
13	12/12/2009 17:13	100	5	On	110	Off	12	Waveform acquisition (0)	Ok	Stopped earlier. No data saved
14	12/12/2009 17:21	100	5	On	110	Off	12	Waveform acquisition (244)	Ok	
15	12/12/2009 17:26	100	10	On	110	Off	12	Waveform acquisition (245)	Ok	
16	12/12/2009 17:37	100	10	Off	110	Off	12	Waveform acquisition (166)	Electrical noise	

Different tests were run at walking speed, 5 and 10 mph; samples of waveforms acquired at the different speeds are reported in Figures 7.4–7.7. Once the time-domain windows of the acquired waveforms were analyzed, it was determined that the new isolating sensor holders were performed as designed by keeping the sensors completely free from mechanical noise at the three different testing speeds. Run #15 was conducted with the air-knife device active; a very low level of noise, not adversely affecting the data, was generated by the air-knife blower and picked up by the sensors responding at the lowest frequency, as depicted in the top graph of Figure 7.6 (small ripples are visible on the left of the wave packets). According to the sensor responding at the highest frequency in the bottom graphs of Figures 7.4–7.7, the EMI generated by the servo-device is clearly visible; this interference was definitely affecting the inspection results, indicative of the need to be addressed before subsequent tests.

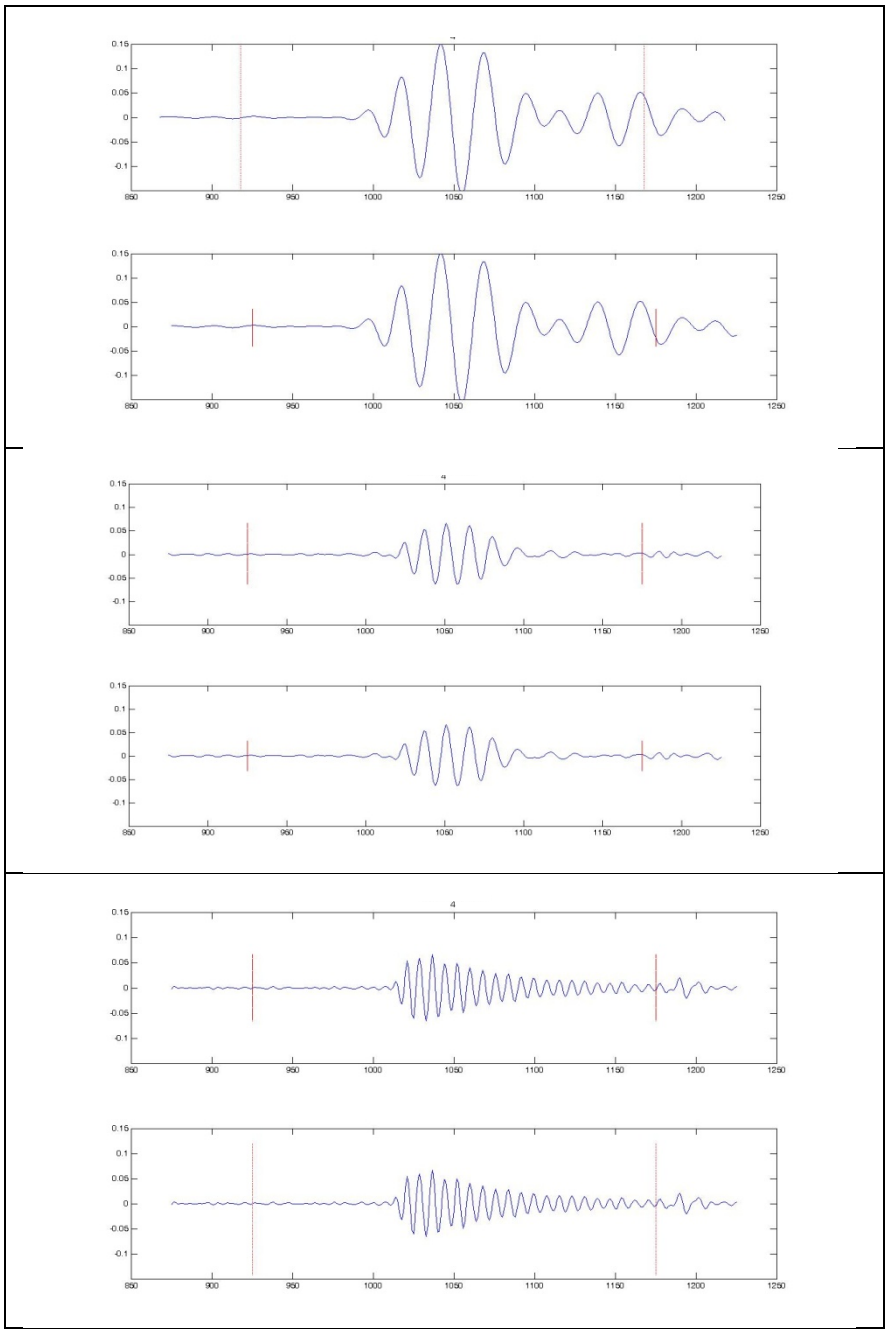

Figure 7.4. Samples of Raw Waveforms Extracted from Various Sensors in Run #4, Acquired at Walking Speed

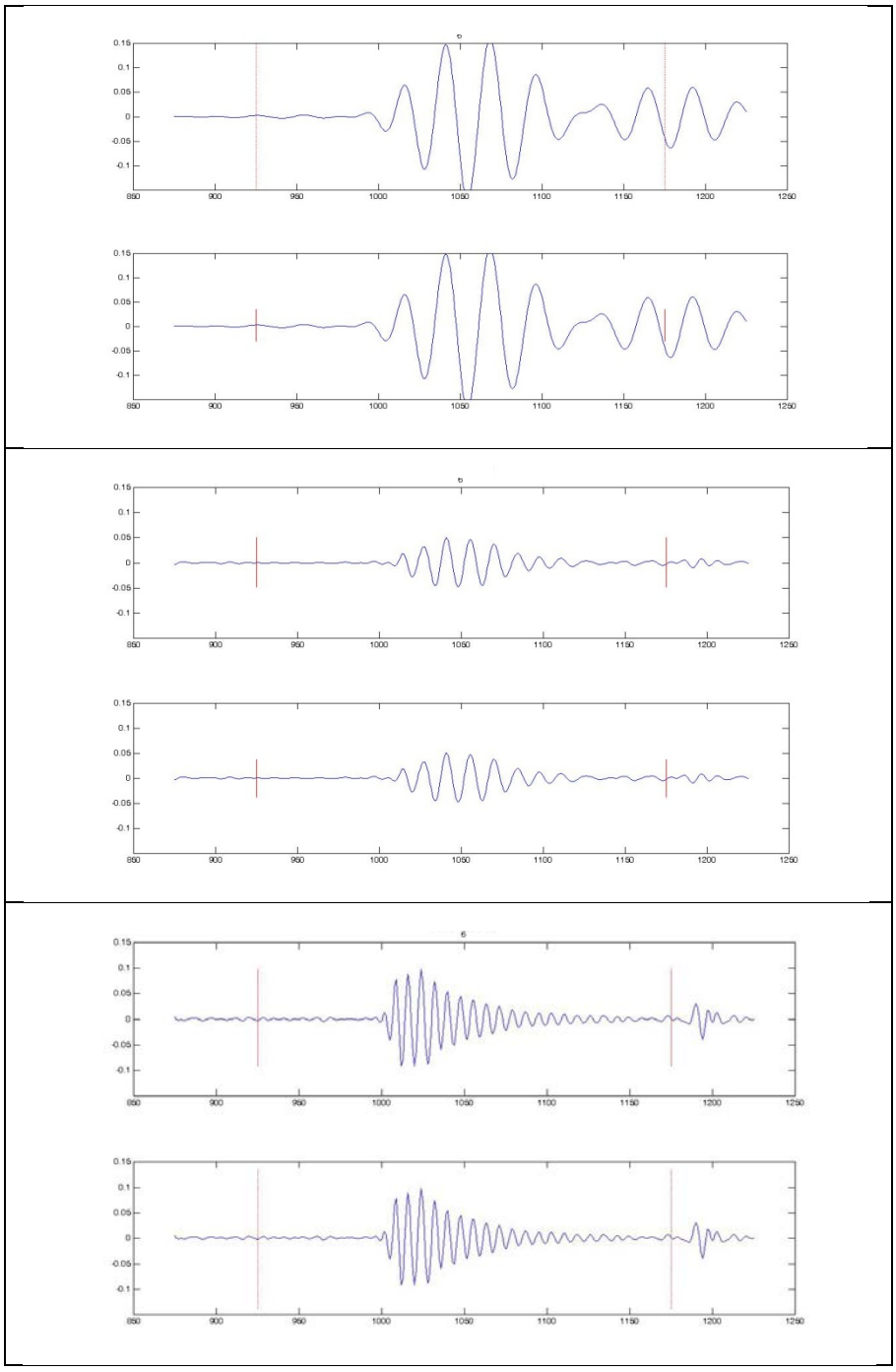

Figure 7.5. Samples of Raw Waveforms Extracted from Various Sensors in Run #5, Acquired at 5 mph

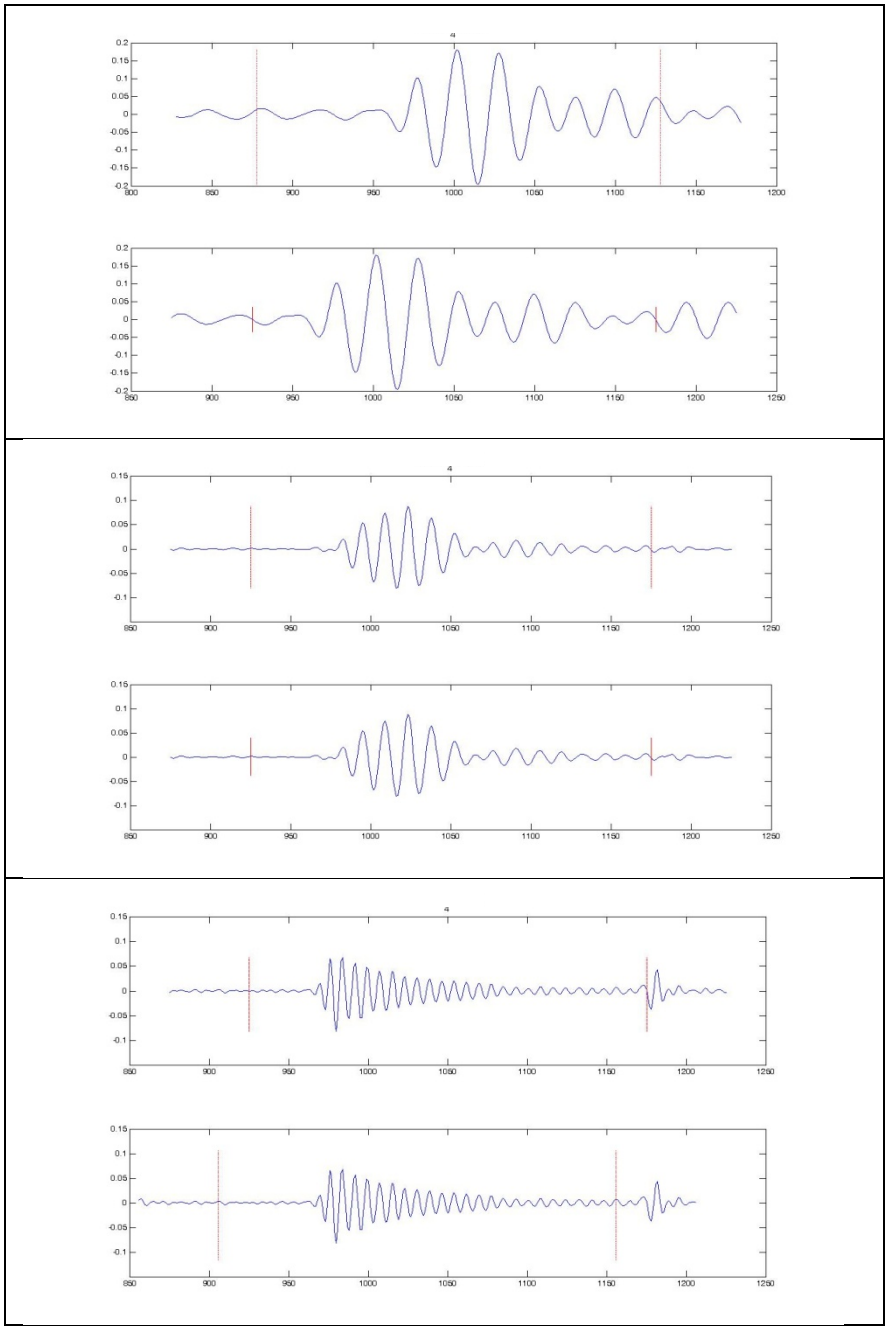

Figure 7.6. Samples of Raw Waveforms Extracted from Various Sensors in Run #15, Acquired at 10 mph, with the Air-Knife Active

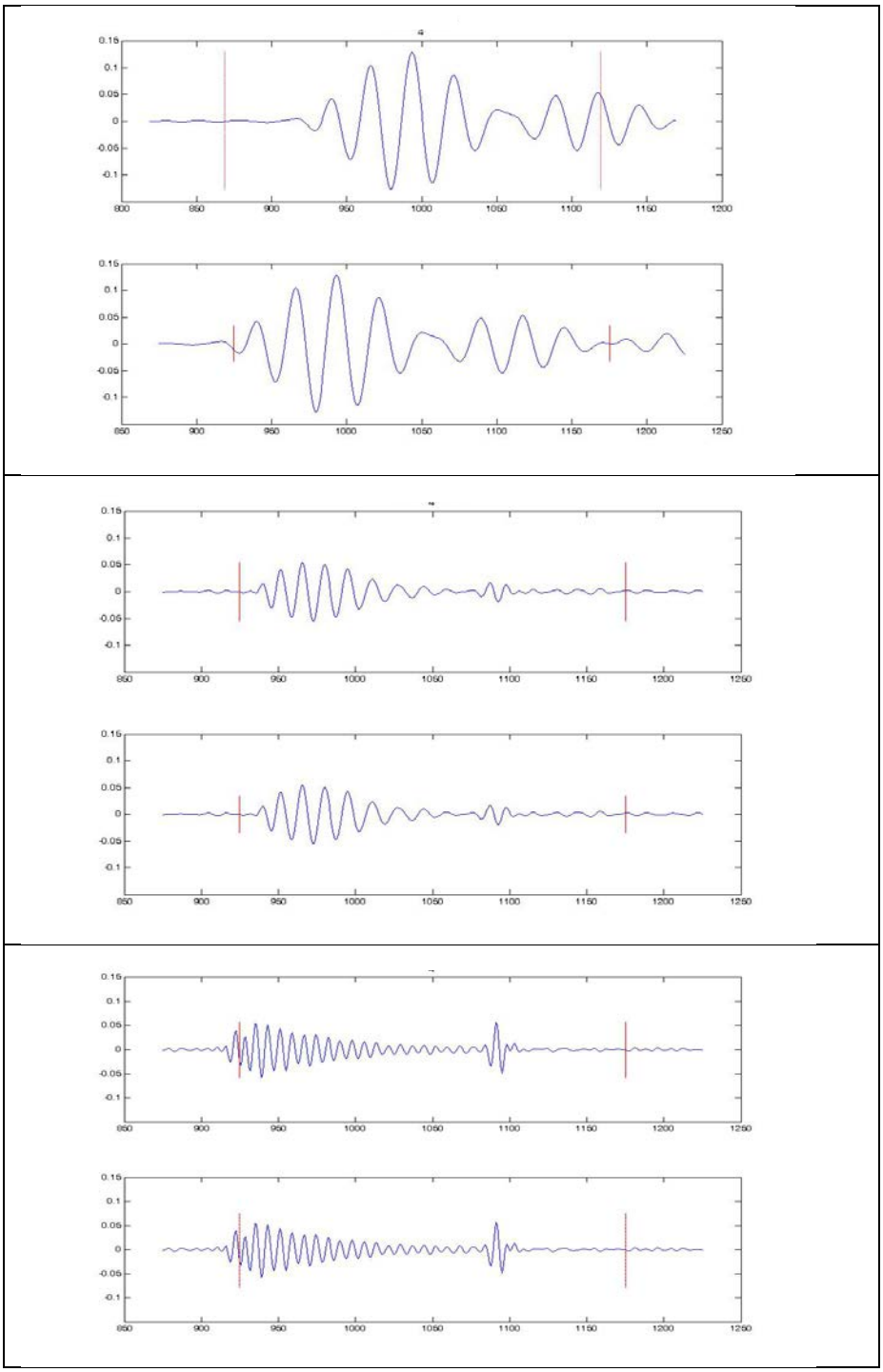

Figure 7.7. Samples of Raw Waveforms Extracted from Various Sensors in Run #16, Acquired at 10 mph

Servo-log data was also acquired by ENSCO for each of the test reported in Table 7.3; this data was also analyzed by UCSD, and the results are also reported here. Figures 7.8–7.13 contain the plot of the X and Y displacements of the servo-arm with respect to the "zero" position (red

and blue plots, respectively, named X-Tolerance and Y-Tolerance). This is the correct position of the arm with respect to the rail head. As mentioned above, the servo was not active along the Y direction, although the servo-positioning sensor was still measuring the Y displacement. Hence, since the Y position was not adjusted by the servo, the precision assessment is limited to the X-tolerance. The desired tolerance limits are also reported in the graphs. Figure 7.8 shows that at walking speed the servo was keeping the horizontal displacements within the allowed limits. Figures 7.9–7.12 show that at 5- and 10-mile per hour speeds some points along the tested paths were out of the tolerance interval. Those "outliers" can be due to the positioning-sensor reading a point at the gap between two adjacent rails (joint), or to the failure of the servo in adjusting the arm quickly enough to the correct position for a sudden vertical or horizontal misalignment. Looking at the right side of the plots depicted in Figure 7.12 (feet ~351–500) collected at walking speed along the curve, it can be deduced that the horizontal position had several points out of tolerance. Figure 7.13 is also interesting since it shows the Y position while R-4 was backing up to the starting point of the track; feet 265–360 are a mirror of the last ~100 ft inspected along the track. All figures show the same trend of the Y position, which gives confidence in the accuracy of the reading sensor. Of course no information could be obtained on the accuracy of the Y positioning adjustment as the Y servo-arm was not operated as discussed above.

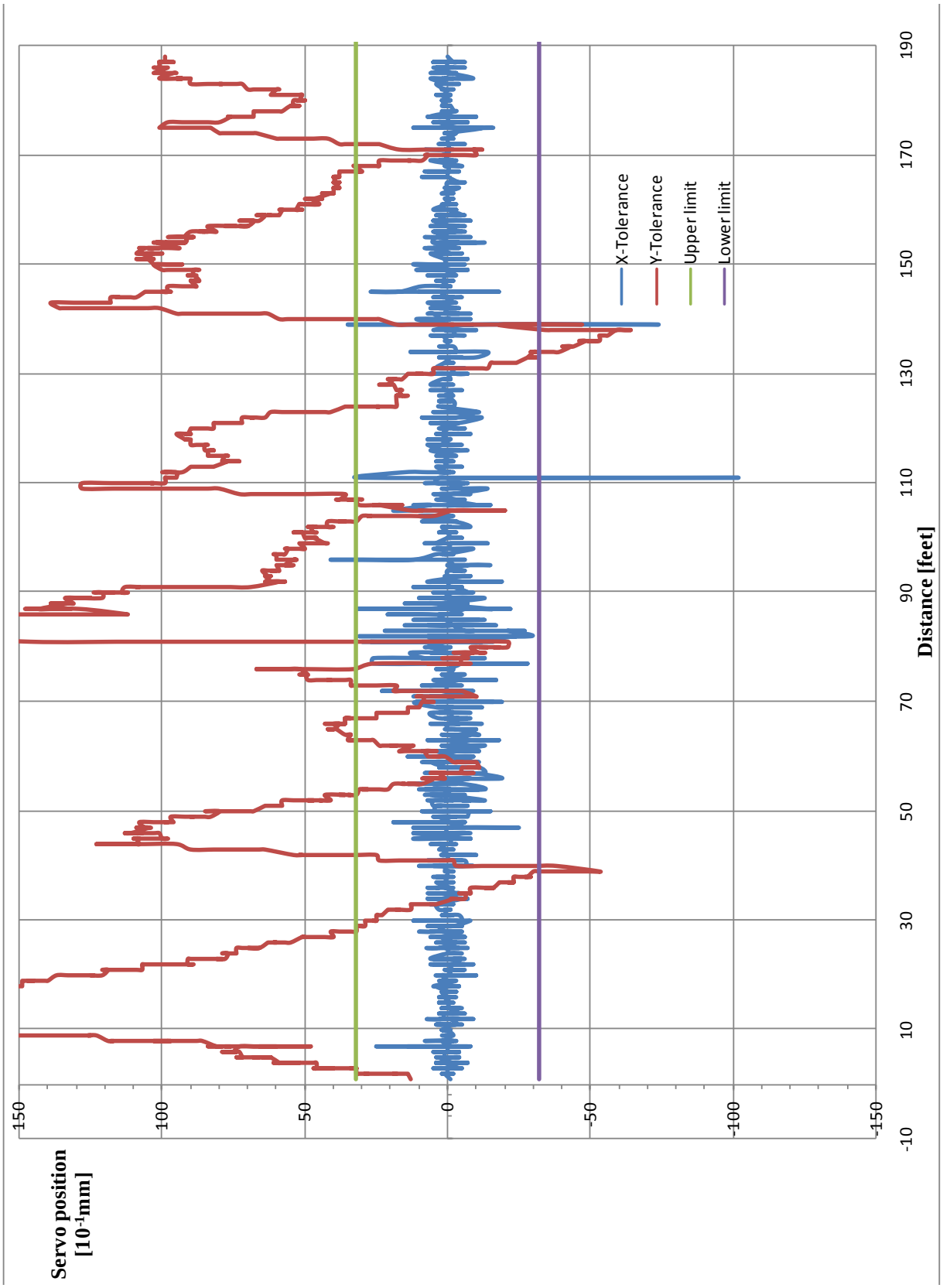

Figure 7.8. Servo-Log Data in Test #4, Walking Speed

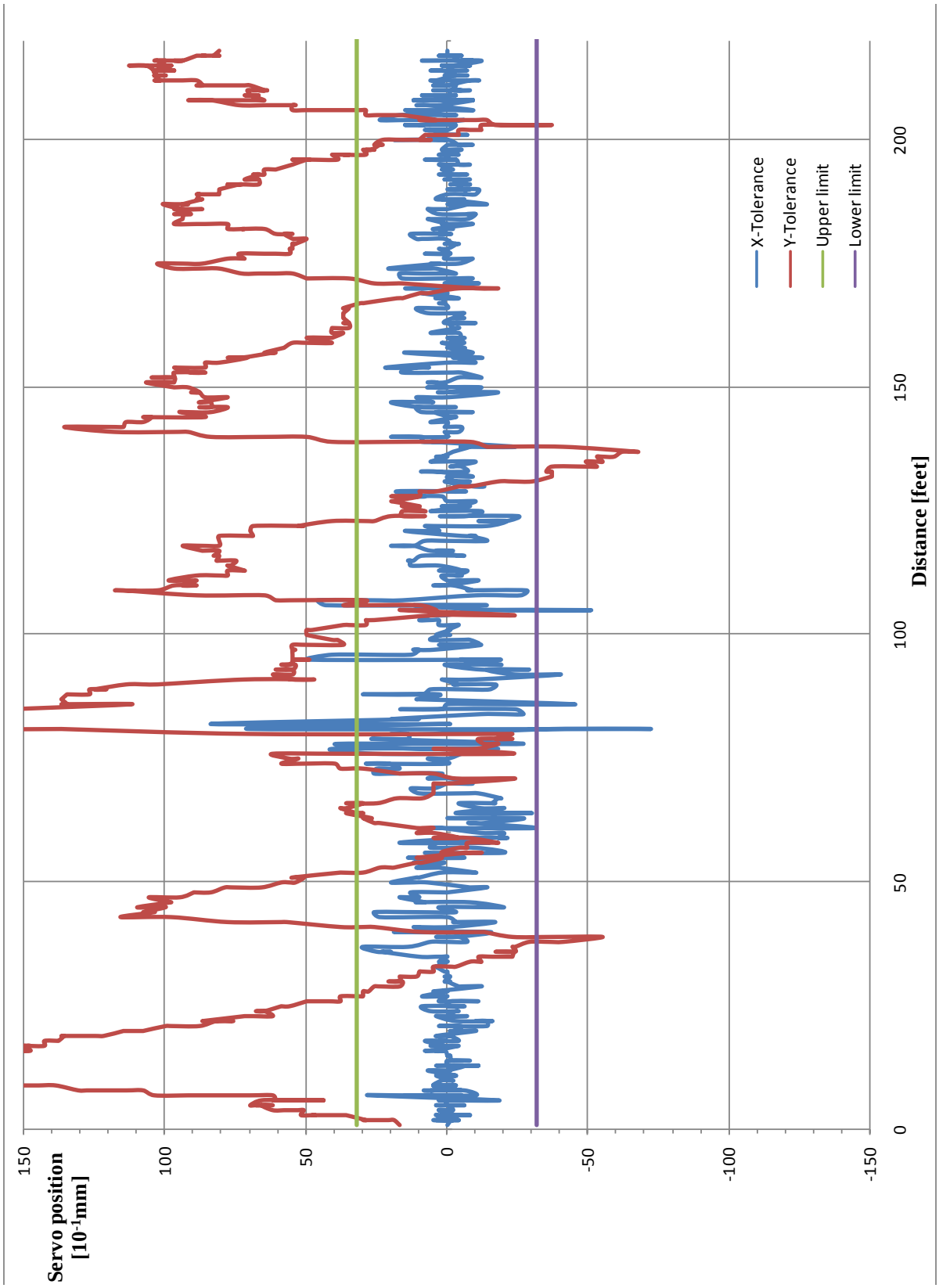

Figure 7.9. Servo-Log Data in Test #12, 5 mph Speed

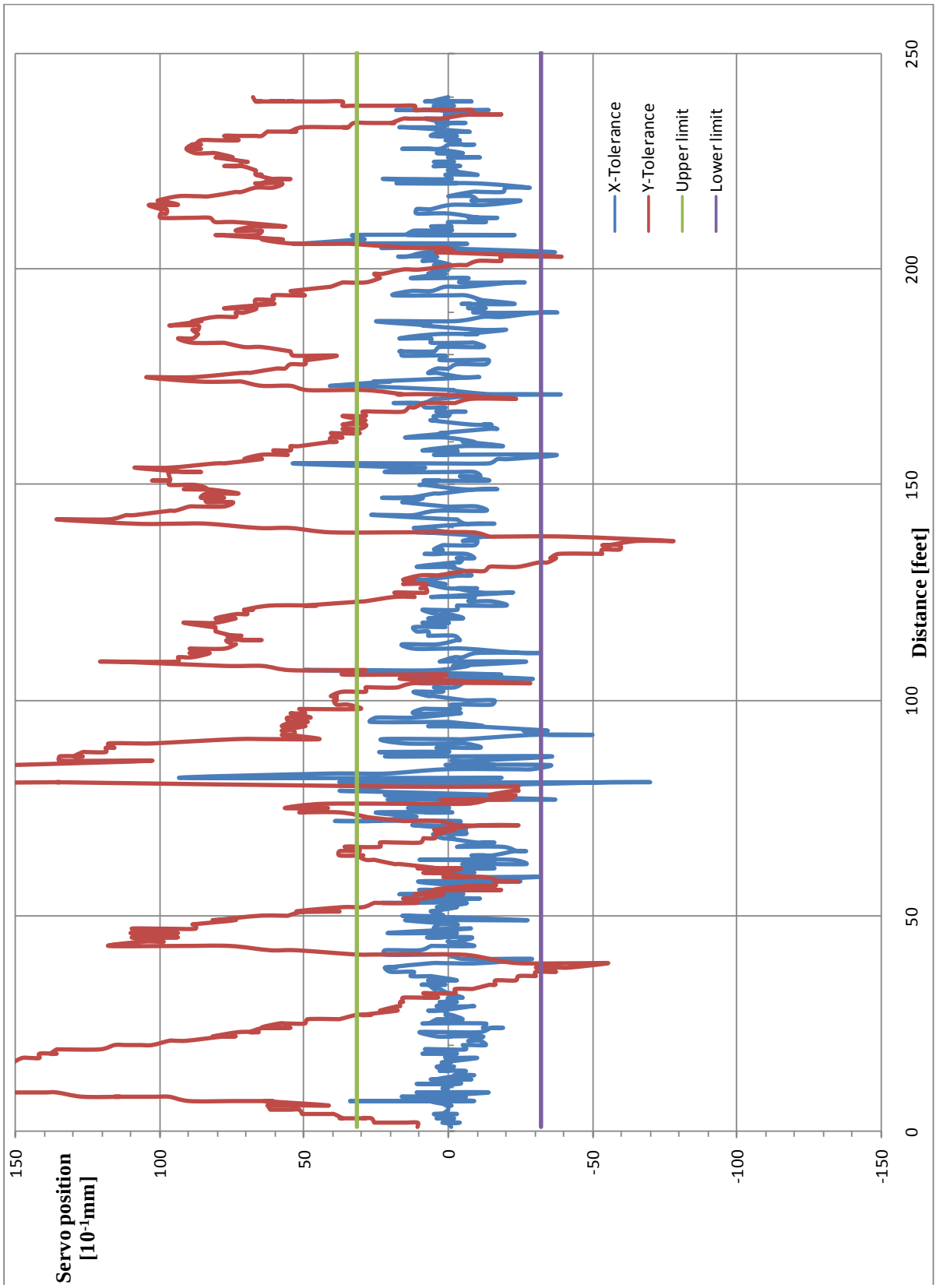

Figure 7.10. Servo-Log Data in Test #14, 5 mph Speed

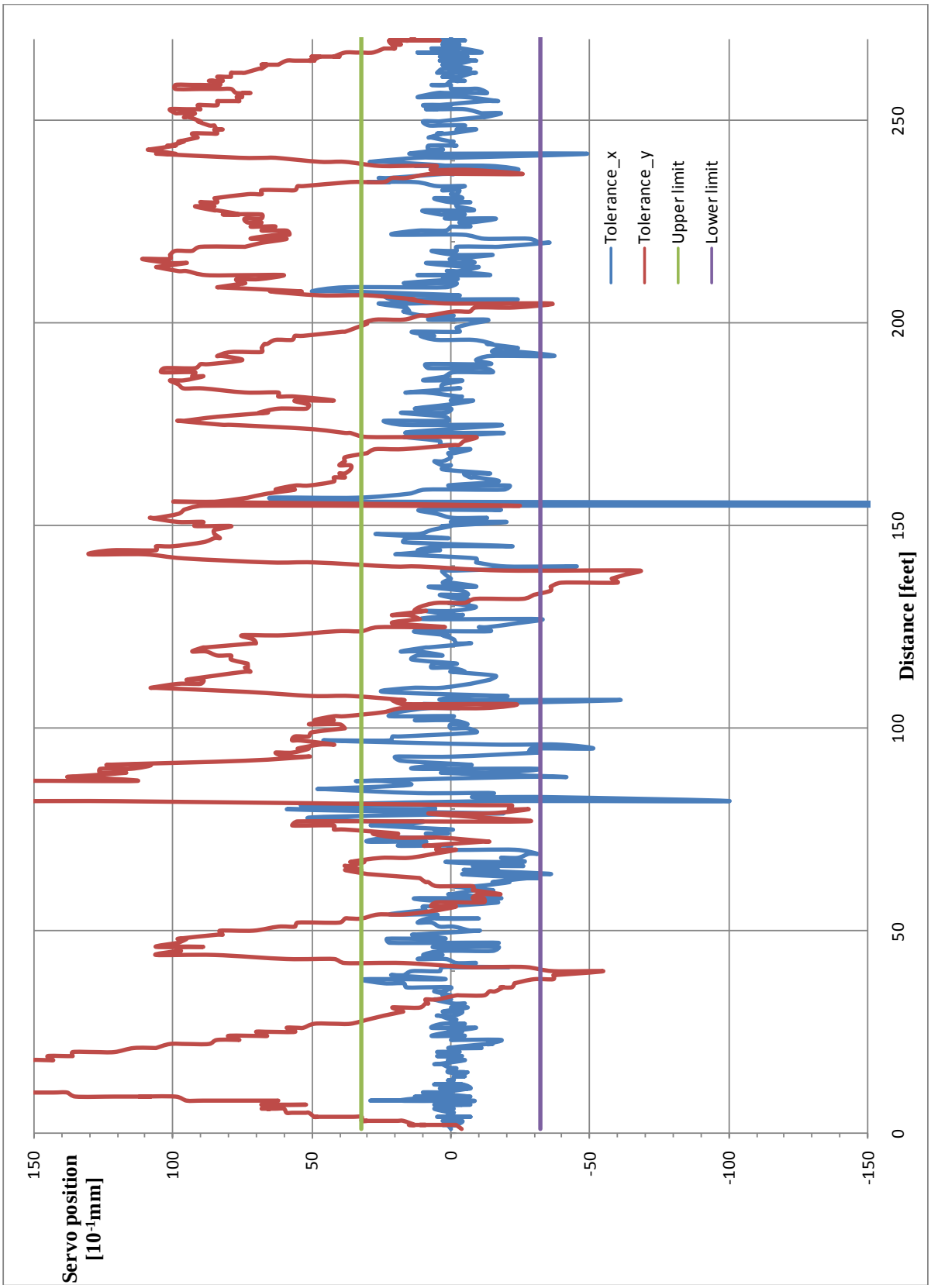

Figure 7.11. Servo-Log Data in Test #11, 10 mph Speed

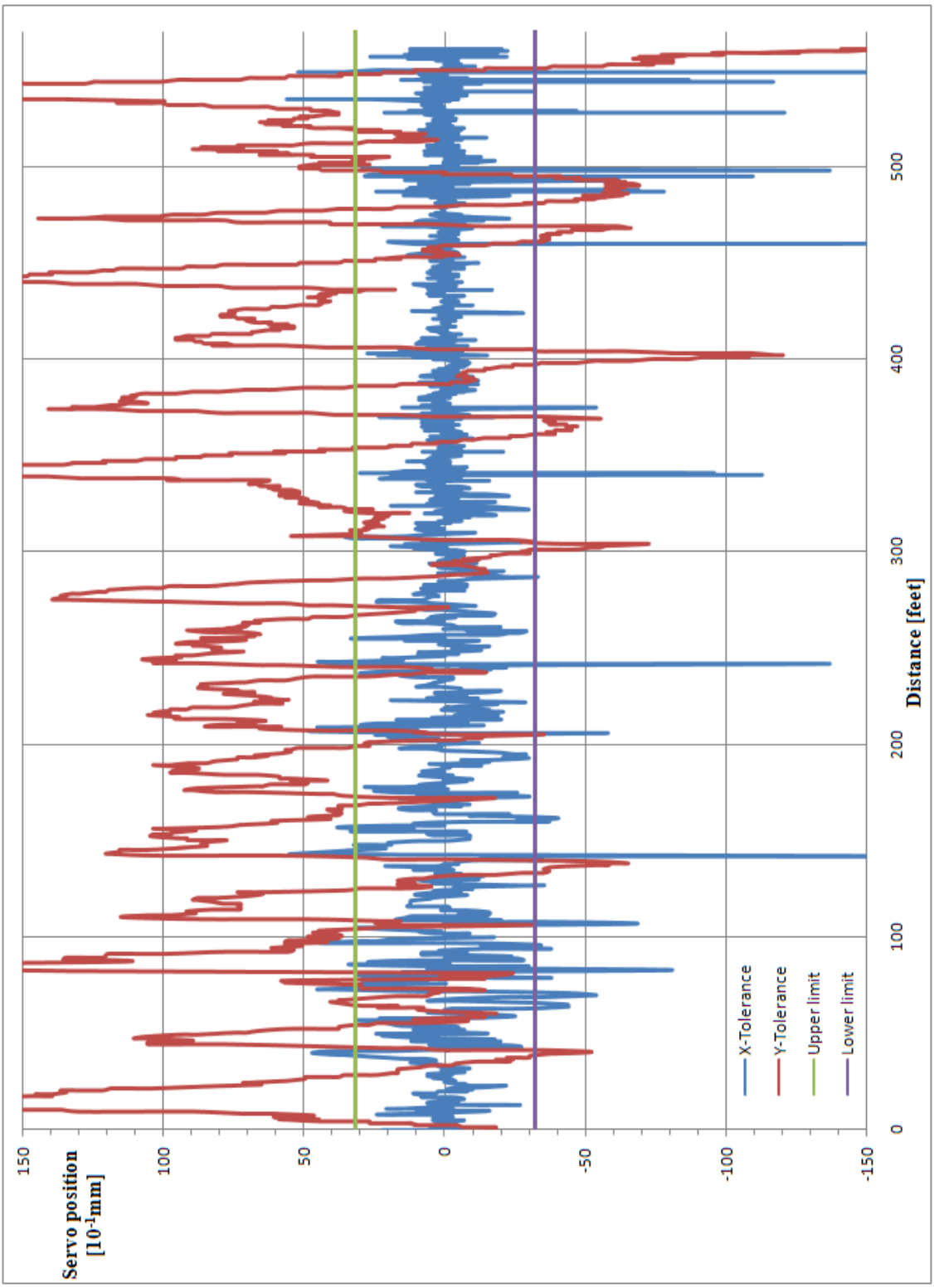

Figure 7.12. Servo-Log Data in Test #9, 10 mph Speed (positions 1–350 ft), and Walking Speed (positions 351–550 ft in curve)

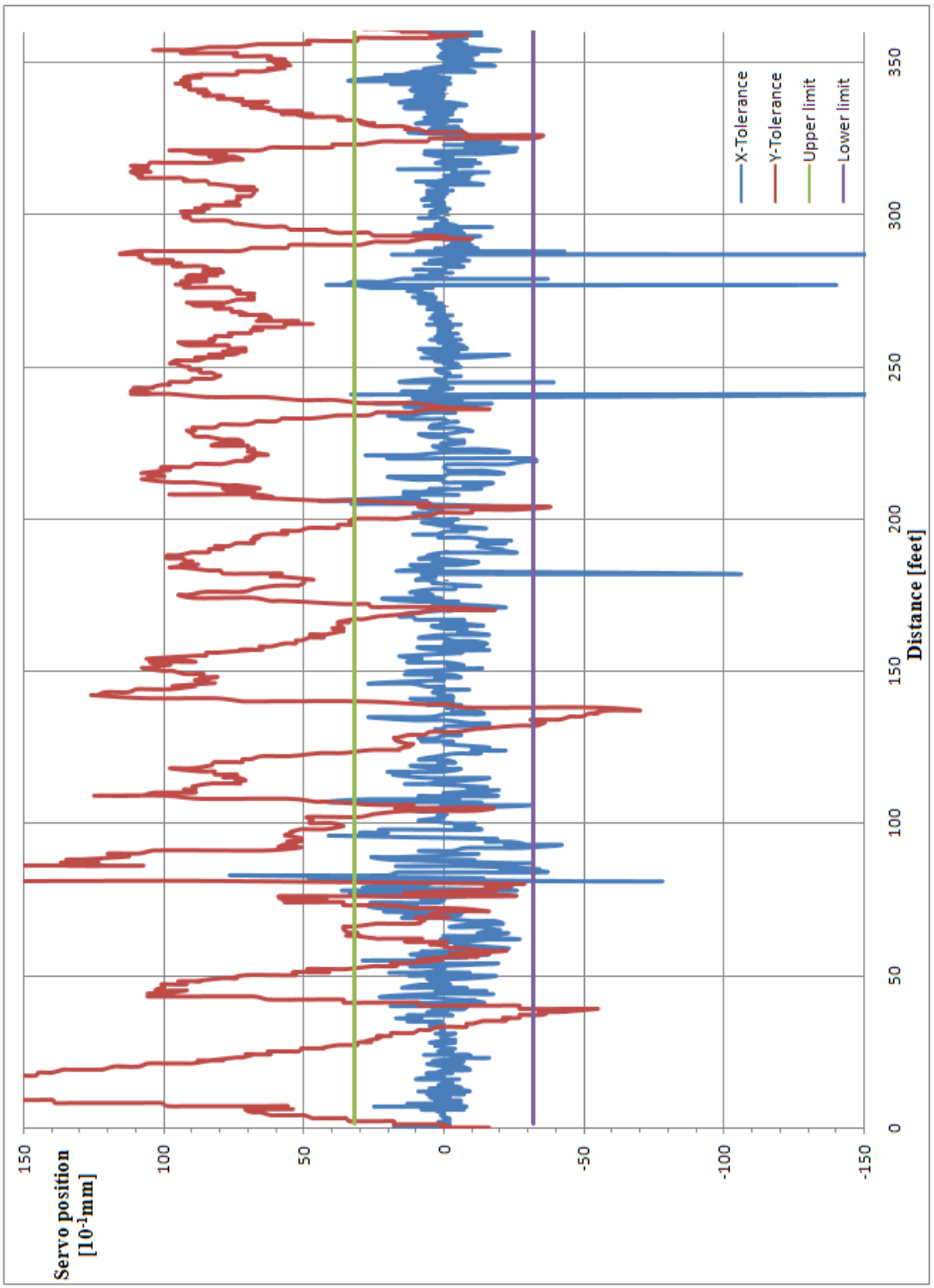

Figure 7.13. Servo-Log Data in Test #7, 5 mph Speed (positions 1–264 ft), and Walking Speed Returning Back on Same Path (positions 265–360 ft)

In conclusion, the results of the fourth field test were very useful to evaluate the substantial changes of the prototype following the third field test (March–December 2008). These changes included (1) the new compact design of the system hardware that had to accommodate the laser, (2) the new sensor mounts isolated from mechanical vibrations, and (3) the new version of the software that was completely migrated from regular LabVIEW to Real-Time LabVIEW to be able to perform at fast speed. The tests were also extremely valuable to tackle the integration of the prototype with ENSCO's servo-mechanism as well as to identify key issues needing improvement in the servo-mechanism alone.

8. Fifth Field Test (Gettysburg, PA, May 2009)

8.1 Prototype Upgrades

In light of the results of the fourth field test, upgrades were made to improve the performance and operational reliability of the Noncontact Defect Detection prototype. The following three main tasks had to be addressed:

1) Availability and stability of electrical power onboard of R-4

With major upgrade to electrical and mechanical parts in R-4, ENSCO addressed task #1. Three phase and single-phase 208 V and single-phase 110 V were available onboard. Except for a laser power supply (three phase 208 V), all the prototype components were powered through uninterrupted power source (UPS) devices.

2) Reduction and/or elimination of electrical noise in the prototype sensor lines

This task was tackled by collaborative actions among UCSD and ENSCO, which consisted mainly of a) reducing/eliminating noise sources and b) shielding sensitive components to outside interferences.

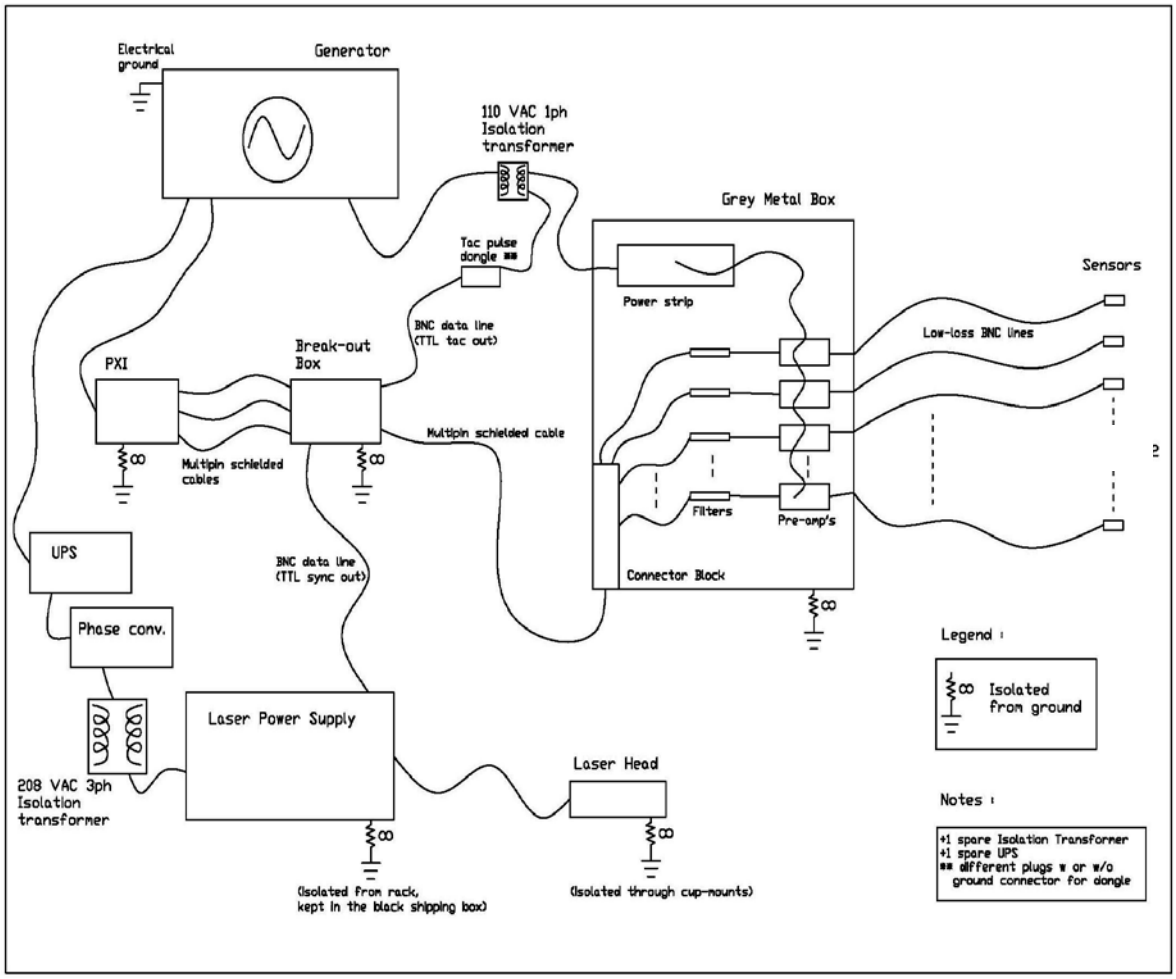

Figure 8.1. Wiring Layout of Power and Data Connections

In light of the findings of the fourth field test, it was understood that electrical components of the servo-system were causing a strong interference that was picked up by UCSD sensor lines. ENSCO installed filters along the servo-system lines to successfully eliminate this main noise source. The wiring and cable routing layout shown in Fig. 8.1 was considered to minimize any possible type of interference between power and data lines inside R-4. Isolation transformers were provided by ENSCO to avoid any noise being transmitted through ground lines. UCSD equipped its data acquisition system with an extra digital counter board to electrically separate the analog lines connected to the ultrasonic sensors and the digital lines connected to the laser digital sync-out and the ENSCO Track Geometry Measurement System (TGMS) positioning system; real-time software was modified accordingly. UCSD also replaced the sensor coaxial lines with better shielded ones (older 45-decibel shielding power stranded core was upgraded to 90-decibel shielding power solid core). Shielding of the steel box containing electrical components for the signal conditioning was increased, and signal preamplifiers that performed better were installed. The power/ground connectivity scheme was arranged to avoid any possible ground-loop connection.

3) Increase of mechanical stability of the servo-arm, reduction of resonance vibration phenomena

ENSCO redesigned the connection between the prototype mounting beam and the servo-mounts, replacing the one-support point cantilever design with a two-support points beam, through the addition of an aluminum truss structure, as shown in Figure 8.2. The new design provided sufficient stiffness for mounting of the prototype and did not show any resonance phenomena, allowing for installation of the servo-positioning sensor on the prototype mounting beam.

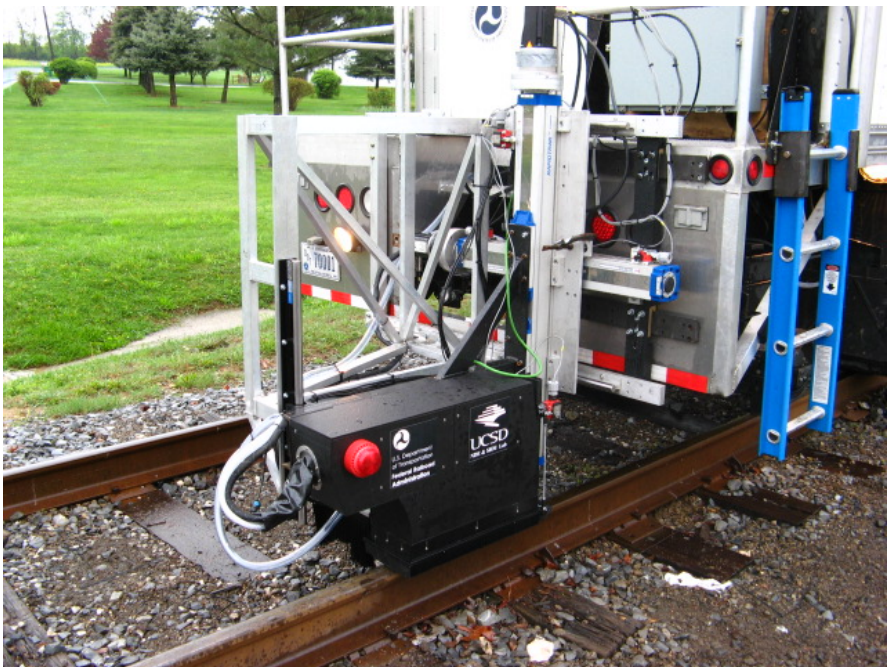

Figure 8.2. Improved Connection between the Prototype Mounting Beam and the Servo-Mounts

(This stiffer connection allowed for the installation of the servo-positioning sensor on the prototype mounting beam.)

Other minor upgrades were made to the prototype, such as installing a smaller size air-knife blower and modifying some plastic mounting parts to protect the sensors from water, dust, and dirt.

8.2 Summary of Fifth Field Test Results

The fifth field test was performed at the Gettysburg (GET) testing location during the period May 4–7, 2009, for a total of 4 days. Three additional days were spent at ENSCO in Springfield, VA, installing the system on R-4. Because of a logistical impediment, such as a train parked on the GET defect farm line, the proposed testing schedule was changed accordingly, assigning the first day's testing zone to the GET main line. During the last day of testing, after the obstructing train was removed, the prototype was tested in the GET defect farm. A detailed schedule of the testing runs is reported in Tables 8.1 and 8.2.

Table 8.1. Details of Fifth Field Test Runs, May 2009 (days #1–2)

Test Progressive Number	Date	Time	Speed	Sync-foot resolution [in]	System calibration [C] Waveform acquisition [W] Defect detection [D]	Rail condition: wet [W]/dry [D]	Railroad line	Location	Notes
1	5/4/2009 Day 1	5:03 PM	walking	n/a	C [R-4 positioning system calibration]	W	GET main	Tangent track	
2		5:25 PM							
3		6:17 PM							
4		6:40 PM							
5		7:27 PM		1.5"	D			Tangent track	Started at Mile marker 12 -20
6		7:33 PM							
7		7:37 PM						LEFT curve	
8		7:41 PM						Tangent track	
9		7:45 PM						Tangent track and light LEFT curve and RIGHT curve	
10		8:00 PM						Tangent track	
11		8:22 - 8:26 PM			W				waveform files collected: #1-#1807
1 - 2	5/5/2009 Day 2	10:55 - 11:04 AM	walking	1.5"	W [for baseline computation]	W	GET main	Tangent track	Attempting to improve the performance along the curved track, sensors were moved 1/8" towards the gage side.
3		11:16 AM			D			Tangent track	
4		12:29 PM						RIGHT curve	New baseline loaded (curves included)
5		12:35 PM						RIGHT curve and Tangent track	
6		12:45 PM						multiple locations along line	Re-testing track for potential defects. Outliers were later understood to be caused by the system not being aligned with the rail due to poor servo tracking accuracy
7		12:54 PM							
8		1:13 PM							
9		1:21 PM							
10		1:28 PM							
11		1:47 PM							
12		1:53 PM							
13		2:25 PM						Tangent track and LEFT curve	Started at Mile marker 12 -20
14		2:32 PM						Tangent track	
15 A		2:34 PM							
15 B		4:08 PM							
16		4:19 PM							
17		4:24 PM						LEFT curve	
18		5:42 PM		0.5"				Tangent track and RIGHT curve	
19		5:45 PM							

Table 8.2. Details of Fifth Field Test Runs, May 2009 (days #3–4)

Test Progressive Number	Date	Time	Speed	Sync-foot resolution [in]	System calibration [C] Waveform acquisition [W] Defect detection [D]	Rail condition: wet [W]/dry [D]	Railroad line	Location	Notes
20	5/6/2009 Day 3	6:20 PM	crawling	1.5"	D	W	GET main	Tangent track and 7 deg. RIGHT Curve and 8 deg. LEFT curve	
21		6:26 PM							
22		6:35 PM							
23		6:40 PM							
24		6:49 PM						8 deg. LEFT curve	
25		7:12 - 7:14 PM			W			8 deg. LEFT curve and 7 deg. RIGHT curve	waveform files collected: #1-#1008
26									
27									
28									
29		7:22 PM			D			7 deg. RIGHT curve	
30		7:31 PM							
31		7:45 - 7:46 PM			W			Tangent track	waveform files collected: #1-#575
32									
33		7:52 PM			D				
34	5/7/2009 Day 4	9:06 AM	crawling	1.5"	W	W	GET main	4.5 deg. RIGHT curve	waveform files collected: #1-#582
35		9:15 AM			D				
36		9:23 AM							
37		9:33 - 10:01 AM			W			7 deg. RIGHT curve and Tangent track	waveform files collected: #583-#1327
38									waveform files collected: #1328-#4168
39									waveform files collected: #4169-#6951
40								8 deg. LEFT curve	waveform files collected: #6952-#8426
41		2:02 PM			D		GET Defect farm	Tangent track (~100')	
42		2:15 PM							
43		2:34 PM							water spray not working
44		3:02 PM							water spray fixed
45		3:12 PM							
46		3:16 PM							
47		3:28 PM							time window decreased to 80 usec
48		3:39 PM							loaded UCSD baseline, time window 100 usec
49		3:45 PM							reloaded GET baseline
50		4:18 PM							moved prototype home position 1/8" towards gage side
51		4:42 PM							moved sensors towards the field side 1/8" typical system configuration
52		4:52 PM							

During days #1-2-3 and the morning of day #4, the prototype was setup and aligned, the ENSCO TGMS positioning system was calibrated, and multiple *Defect Detection* and *Raw Data Test* runs were performed, with the objective of assessing the performance of the system and servo along different track layout geometry (tangent and curved track); no defect was expected to be detected during this phase. In the afternoon of day #4, multiple *Defect Detection* and *Raw Data Test* runs were performed in the GET defect farm, with the objective of assessing the defect detection performance of the prototype. From the analysis of the results of day #1 tests, it was observed that many potential defects were identified by the prototype; a parallel check performed on the servo-log data provided by ENSCO indicated that at the different positions along the track where defects had been detected, the servo-system was not keeping the prototype over the rail within the requested tolerance of ±1/8 in (~3.2 mm) horizontal and vertical. This phenomenon can be observed in Figures 7.3–7.5, which show the D.I. graphs along with the servo-log X-Y positioning errors for different type of track (tangent track, right and left curves). A detailed analysis of the data showed that the presence of joints and the rail pitch angle varying along the rail span were keys to the unexpected poor servo-tracking performance. UCSD came to the conclusion that the servo cannot be used as a reliable positioning system for the prototype at walking speed.

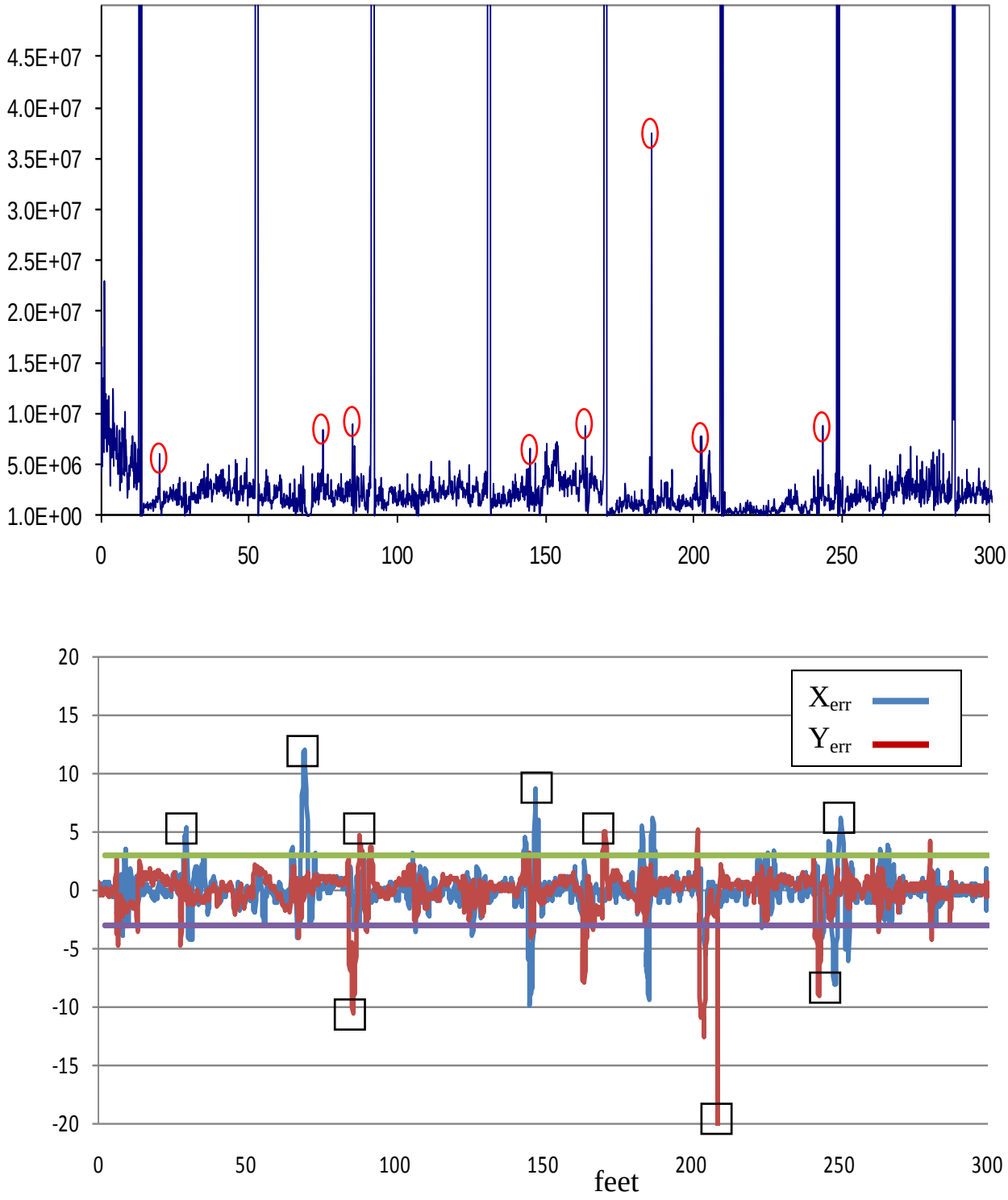

Figure 8.3. D.I. Graph and Servo-Log X-Y Positioning Error Acquired along a Tangent Track while Testing at Walking Speed (run #3, day #1)

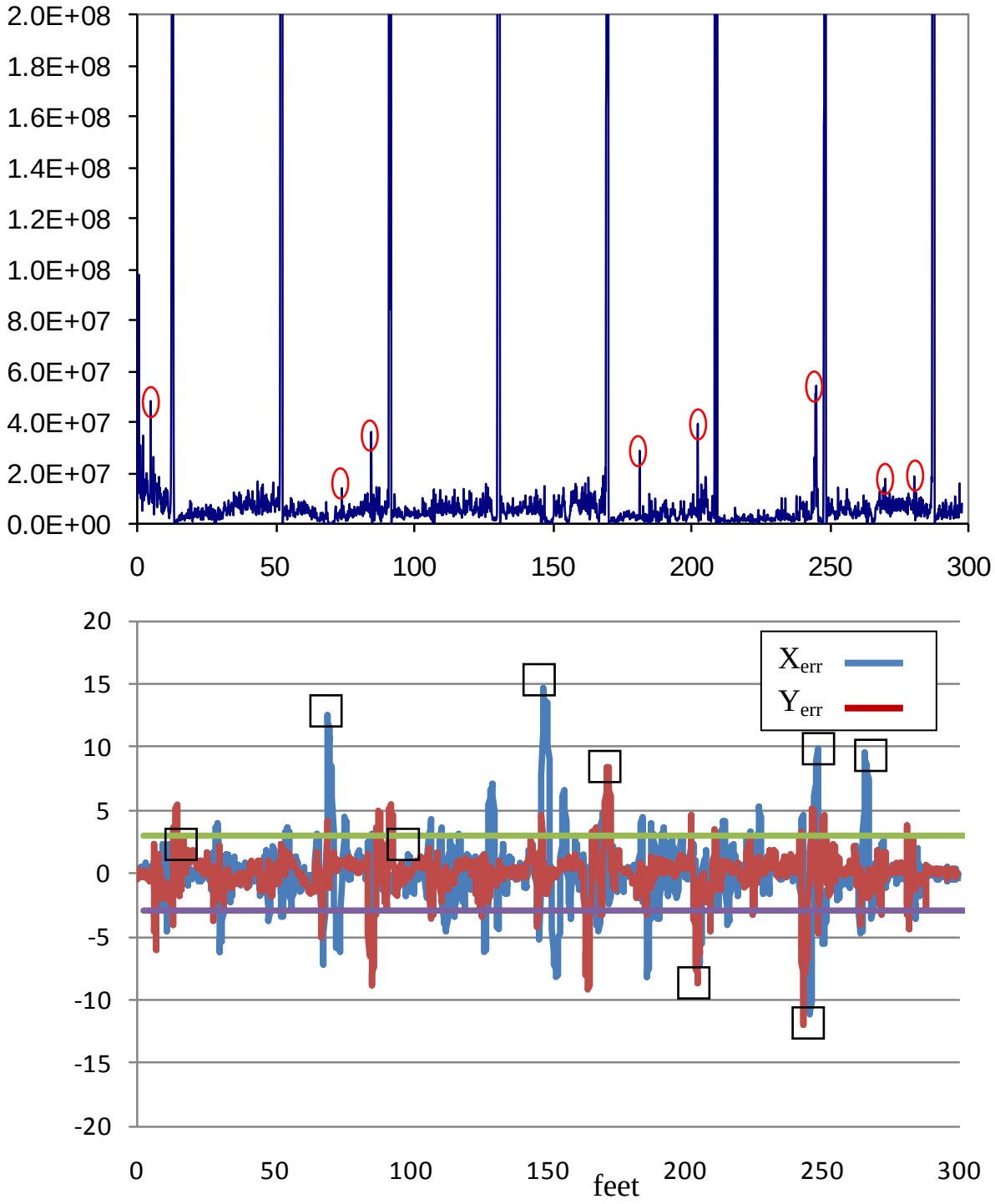

Figure 8.4. D.I. Graph and Servo-Log X-Y Positioning Error Acquired along a Tangent Track while Testing at Walking Speed (run #4, day #1)

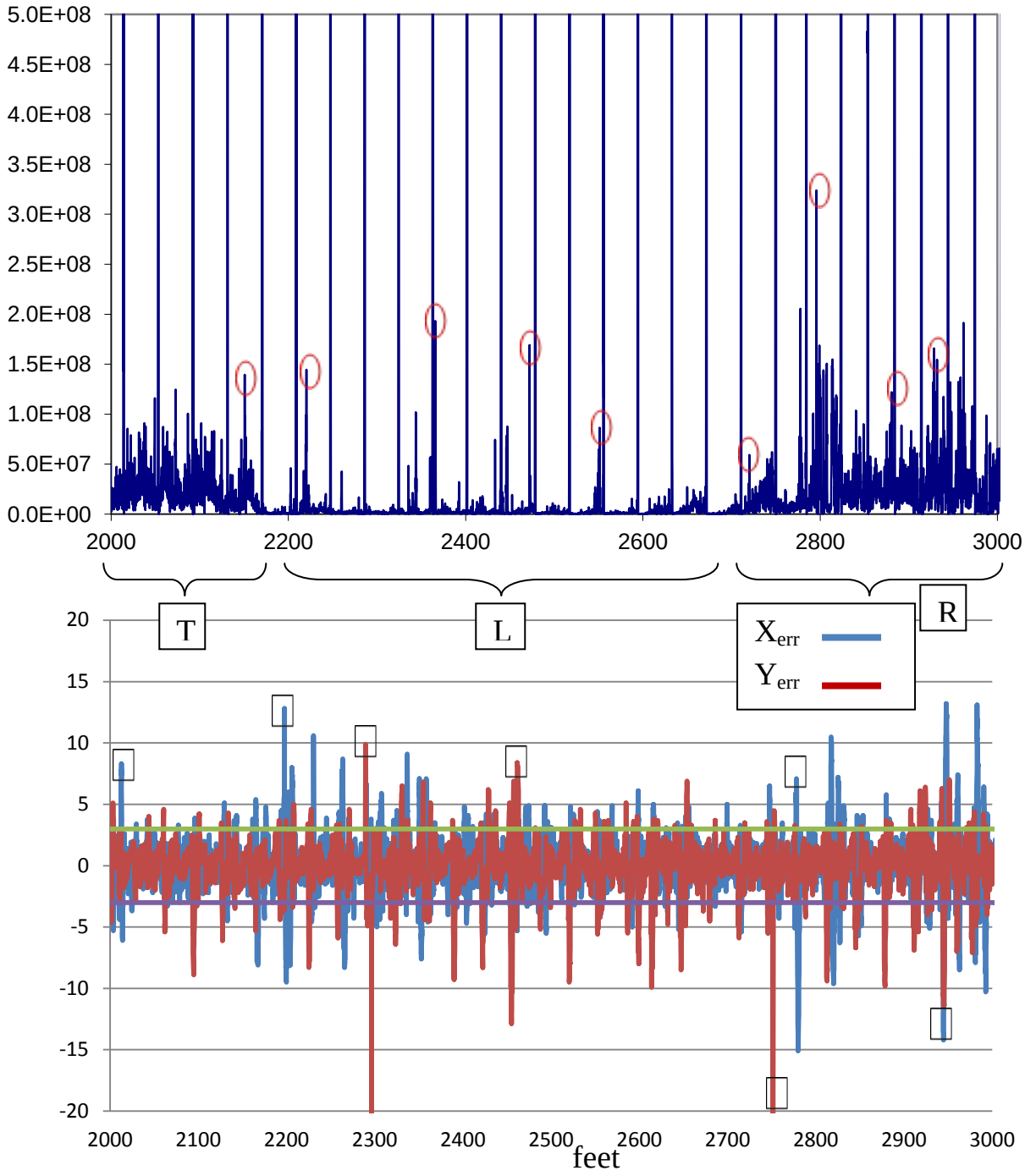

Figure 8.5. D.I. Graph and Servo-Log X-Y Positioning Error Acquired along a Tangent Track (T), a Left (L), and a Right (R) Curve while Testing at Walking Speed (run #9, day #1)

As another source of the false-positive detection, the prototype sensors along a curved track were not positioned correctly with respect to the rail. Previous UCSD calculations provided a maximum curve angle of 7.5°, which was considered to be within the system tolerances. This limit was found to be incorrect, the prototype being sensitive to rail curvature angles as small as

4.5°. At the beginning of day #2, the prototype sensors were initially moved 1/8 in toward the gage side, in an attempt of improving the system performance along a curved track. A slight improvement was noticed in the system tracking left curves, along with a substantial worsening of right curve tracking performance. To separate the servo-tracking problems from the curvature issue, days #3–4 tests were conducted at crawling speed, to ensure a better tracking performance of the servo-system allowing for focusing on the track curvature. Figures 8.6–8.8 show D.I. and servo-log graphs registered during testing at crawling speed along a tangent track, a right and a left curve respectively. Although these data showed a good servo-tracking performance for all three different track geometry layouts, the recordings along the right and left curves still showed false detections, due to the curvature of the rail.

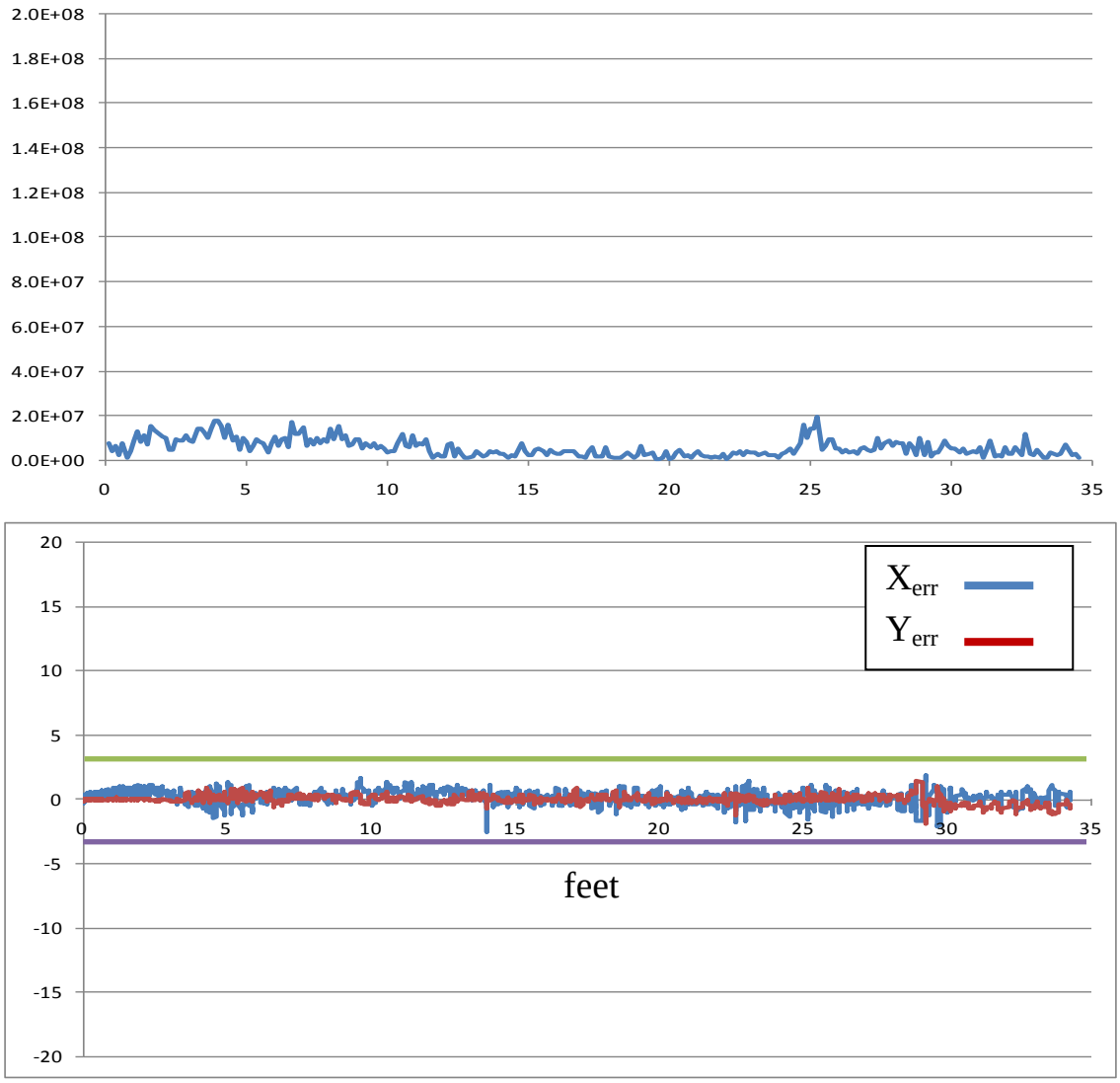

Figure 8.6. D.I. Graph and Servo-Log X-Y Positioning Error Acquired along a Tangent Track while Testing at Crawling Speed (run #33, day#3)

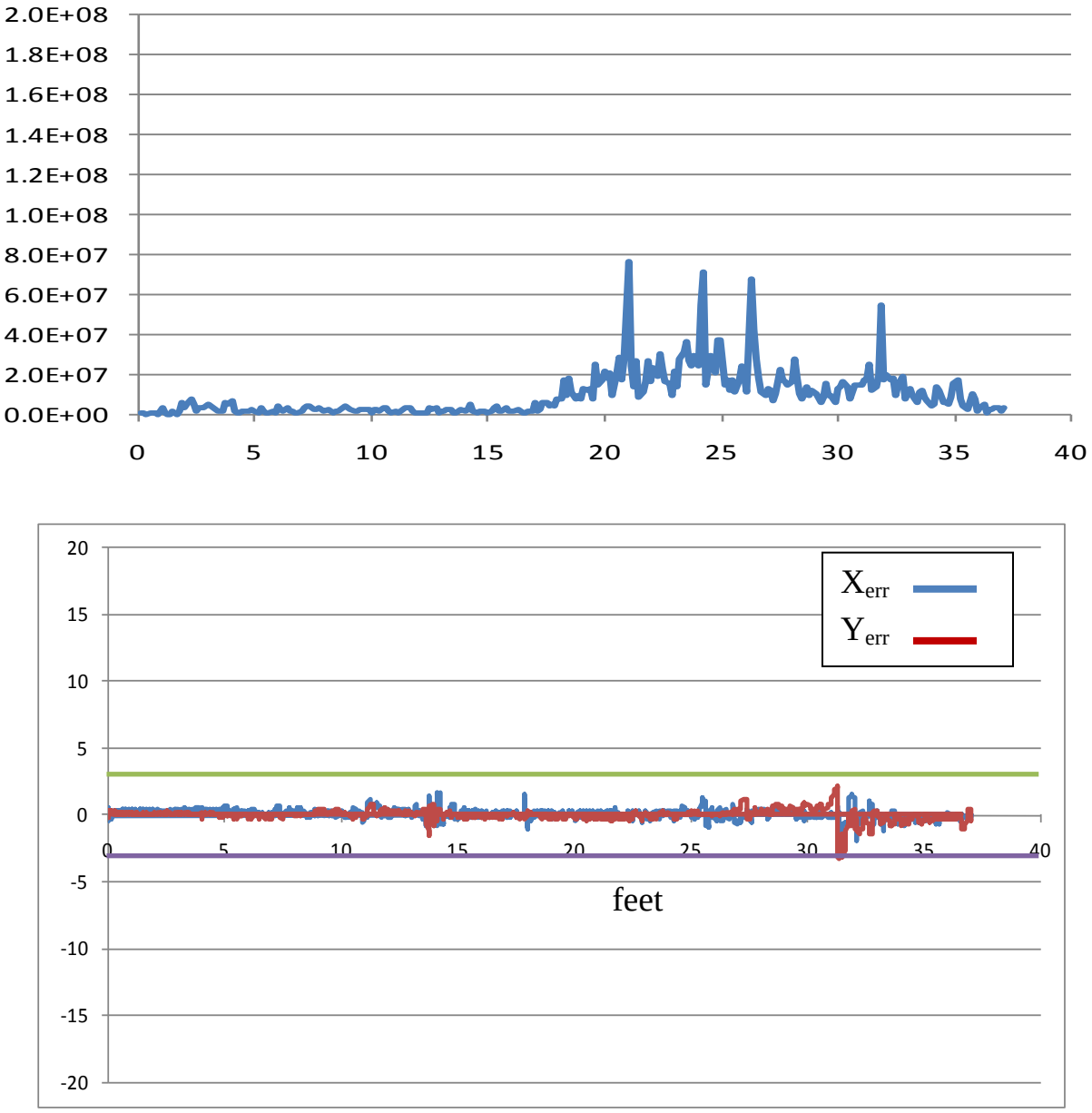

Figure 8.7. D.I. Graph and Servo-Log X-Y Positioning Error Acquired along a 7° Right Curve while Testing at Crawling Speed (run #30, day#3)

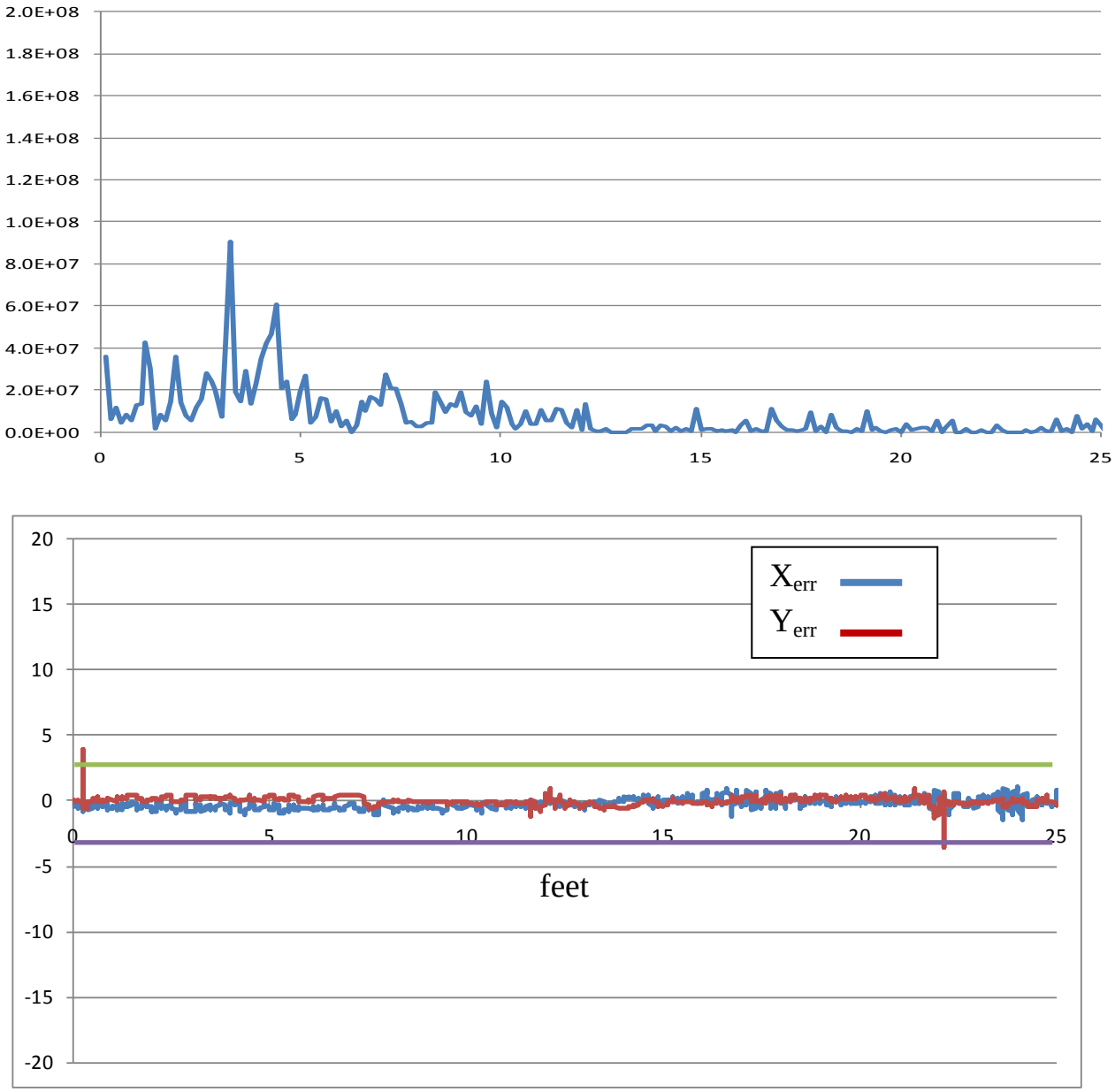

Figure 8.8. D.I. Graph and Servo-Log X-Y Positioning Error Acquired along a 8° Left Curve while Testing at Crawling Speed (run #24, day#3)

Analysis of raw data test runs along a tangent track, an 8° left, a 7° right, and a 4.5° right curves (waveforms acquired during runs #31, #25, #27, and #34, respectively) showed that signal features critical for the defect detection performance of the prototype were sensitive to the different rail curvatures. These features, shown in Figures 8.9–8.12, respectively, were calculated in defect free areas, hence a constant values was expected along the different types of rail. In the light of these results, the use of a mounting plate providing adjustment to the yaw angle in the case of a curved rail inspection was determined to be highly desirable.

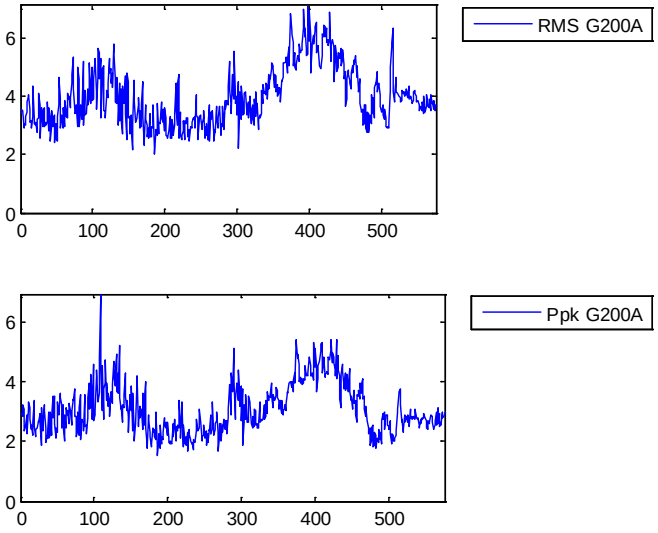

Figure 8.9. Signal Features Calculated by Postprocessing Waveforms Collected at Crawling Speed along a Tangent Track (run #31, day#3)

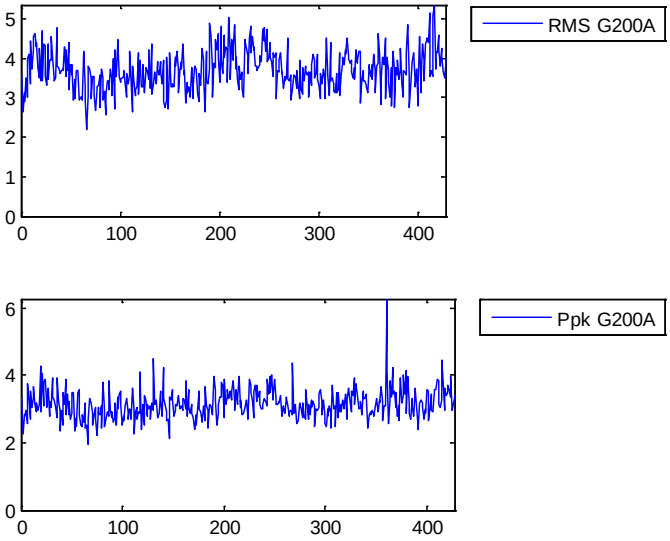

Figure 8.10. Signal Features Calculated by Postprocessing Waveforms Collected at Crawling Speed along an 8° Left Curve (run #25, day #3)

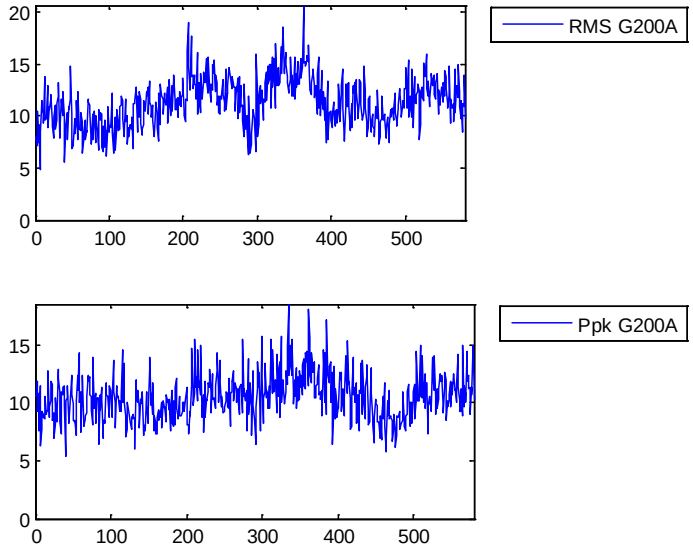

Figure 8.11. Signals Features Calculated by Postprocessing Waveforms Collected at Crawling Speed along a 7° Right Curve (run #27, day #3)

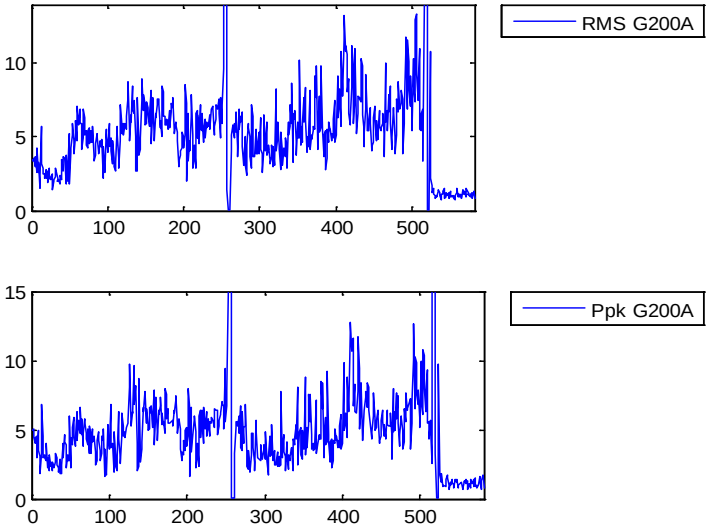

Figure 8.12. Signals Features Calculated by Postprocessing Waveforms Collected at Crawling Speed along a 4.5° Right Curve (run #34, day #3)

Table 8.3 shows the layout of the defect farm rail track; the three TDs are highlighted.

Table 8.3. Gettysburg Defect Farm Layout

Gettysburg Test Site Lay-out (ENSCO/UCSD Rail Flaw Detection - March/29-30/2006)

Location	Foot	Inches	Description
1	0	0	Start of Test Zone
2	13	3	Joint
3	32	0	Chip on gage side of rail head
4	46	3.5	Joint - Orange paint
5	52	5	Large chip (6" long) on gage side of rail head
6	56	2	Large chip (6" long) on gage side of rail head
7	78	9	Flaking on gage side of rail head
8	79	3.5	Joint - flaking on gage side of rail head at joint
9	81	7	Cut surface transverse notch 4mm depth, 50 mm length (~5% H.A)
10	82	7.5	Cut surface transverse notch 2mm depth, 25 mm length (~2% H.A)
11	84	5	Joint - Rail head change 1/2in gap
12	85	6	1st High joint bar (trolley wheel rides up)
13	86	4	Internal transverse defect w/surface head checks (80% HA)
14	87	3.5	Beginning 2nd high joint bar (trolley wheel rides up)
15	88	2	Welded ramp to match rail sizes
16	88	9.5	Joint
17	90	3.5	End 2nd high joint bar (trolley wheel rides up)
18	91	3.5	Internal transverse defect (10% HA)-possibly close to surface
19	93	10	Joint - 1/2 in gap
20	95	1	Cut surface oblique (+45deg) notch 3mm depth, 30mm length (~3.5% H.A) (ADDED LATER)
21	96	4	Internal transverse defect (40% HA)
22	97	8	Cut surface oblique (-45deg) notch 3mm depth, 30mm length (~3.5% H.A) (ADDED LATER)
23	98	9	Joint - Rail head change 1/2in gap
24	99	5	Flaking on gage side of rail head
25	103	0	Chip on gage side of rail head
26	106	7	Flaking chip on field side of rail head
27	112	3	Joint
28	121	0	Flaking chip on field side of rail head
29	126	8	Flaking chip on field side of rail head
30	145	3	Joint (double check) and
31	146	4	Beginnin flaking (severe) on gage side of rail head (continuous)
32	161	0	End flaking (severe) on gage side of rail head (continuous)
33	174	8	Flaking chip on field side of rail head
34	178	3.5	Joint
35	179	0	Flaking chip on field side of rail head
36	191	6	Flaking on gage side of rail head
37	200	0	Finish of test zone

Figures 8.13–8.16 show the results of some defect detection runs on the defect farm track. Figure 8.13 includes D.I. results related to a full run along the track (run #42, length = 100 in); the highest peaks of the D.I. correspond to joints detected during the inspection. Figure 8.14 shows the same data depicted in Figure 8.13, except for joints that have been removed from the plot for an improved readability of the plot. Figures 8.15 and 8.16 show defect detection results of runs #44 and #45 with related servo-log data plots. The plots zoom into the area where the three TDs are located (feet 70–100). The inspected rail was wetted with sprayed water during each detection run; the wet condition of the rail demonstrated to be critical for a good performance of the prototype.

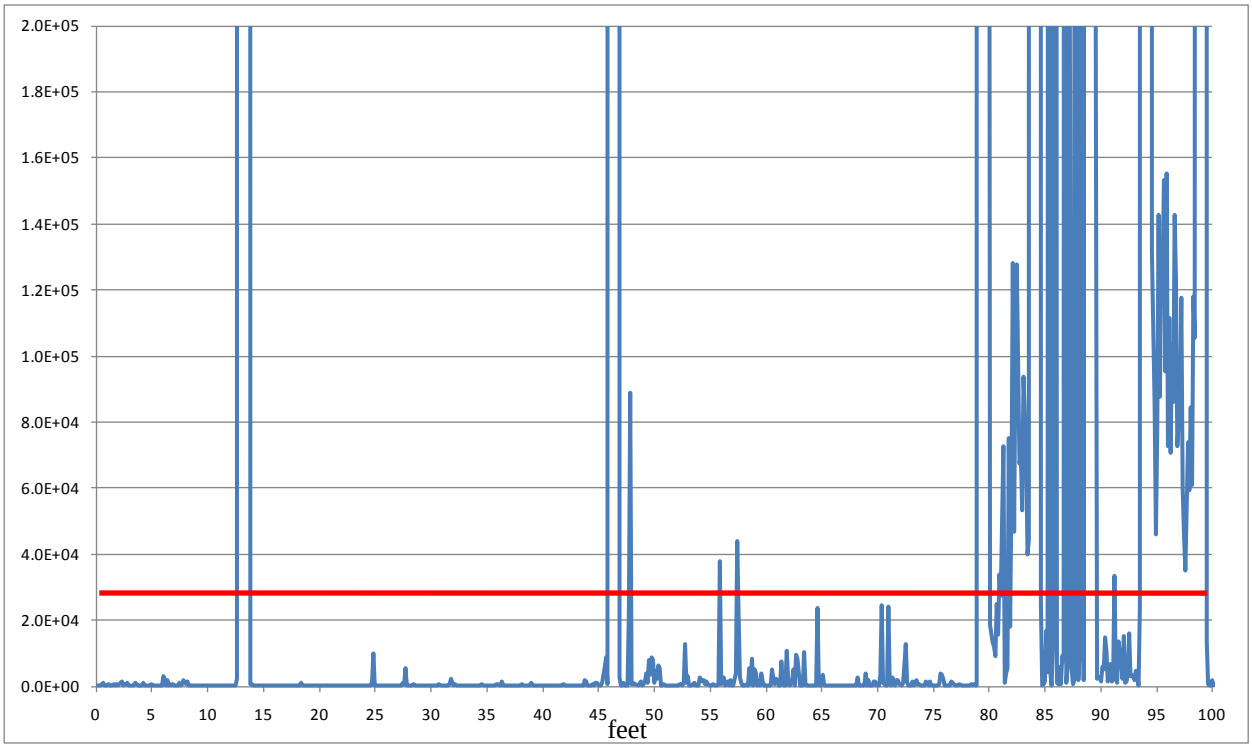

Figure 8.13. Results of a Defect Detection Run on the GET Defect Farm (run #42); the Highest Peaks of the D.I. Correspond to Joints Detected along the Track

The analysis of the D.I. plots showed a good system performance in the detection of the two TDs located at 86'4" and 96'4" from start, respectively. Ultrasonic hand mapping revealed that the first TD was located under shelling of the rail head; the "hidden" condition of this TD did not affect its detectability. The TD located at 91'3.5" from start was detected during test runs #42, #50, and #51; this TD was more difficult to detect because of its particular inclination in the rail head. The two transverse SCs located at 81'7" and 82'7.5" and the two oblique SCs at 95'1" and 97'8" from start were consistently detected within each test run. Although these defect detection runs were performed at crawling speed, the occurrence of false-positive detections because of poor servo-tracking performance was noticed. The servo-log data shown along with the D.I. plots still confirmed the occurrence of many system position "outliers" (horizontal and/or vertical position out of the ±1/8-inch tolerance) in corresponding to false-positive detections.

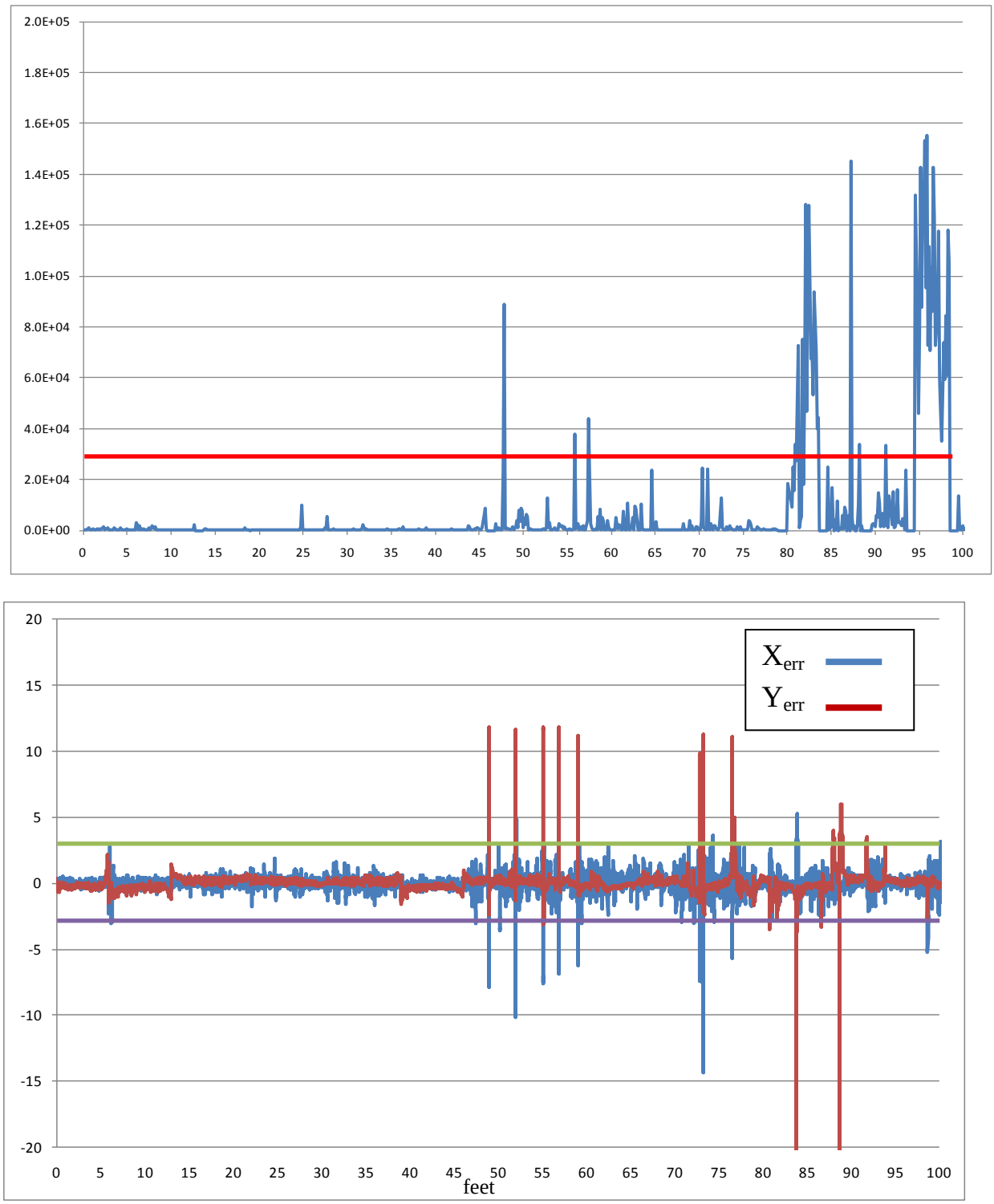

Figure 8.14. Results of a Defect Detection Run on the GET Defect Farm (run #42) with the Related Servo-Log Data; the Joints Have Been Purged from the Graph

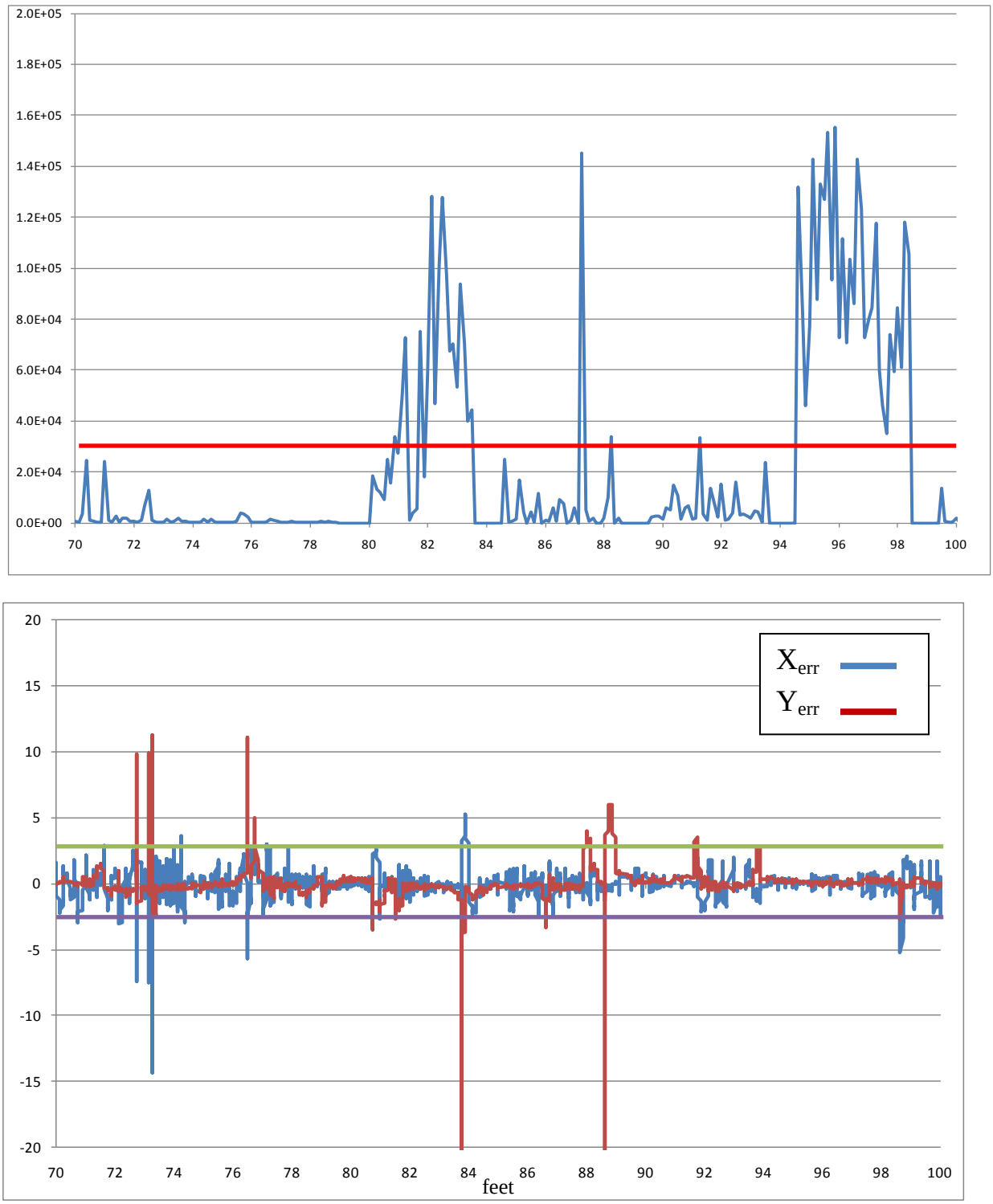

Figure 8.15. Results of a Defect Detection Run on the GET Defect Farm (run #42) with the Related Servo-Log Data

[Showing data zoom in the track area where the TDs are located (feet 70–100). Joints have been purged from the graph.]

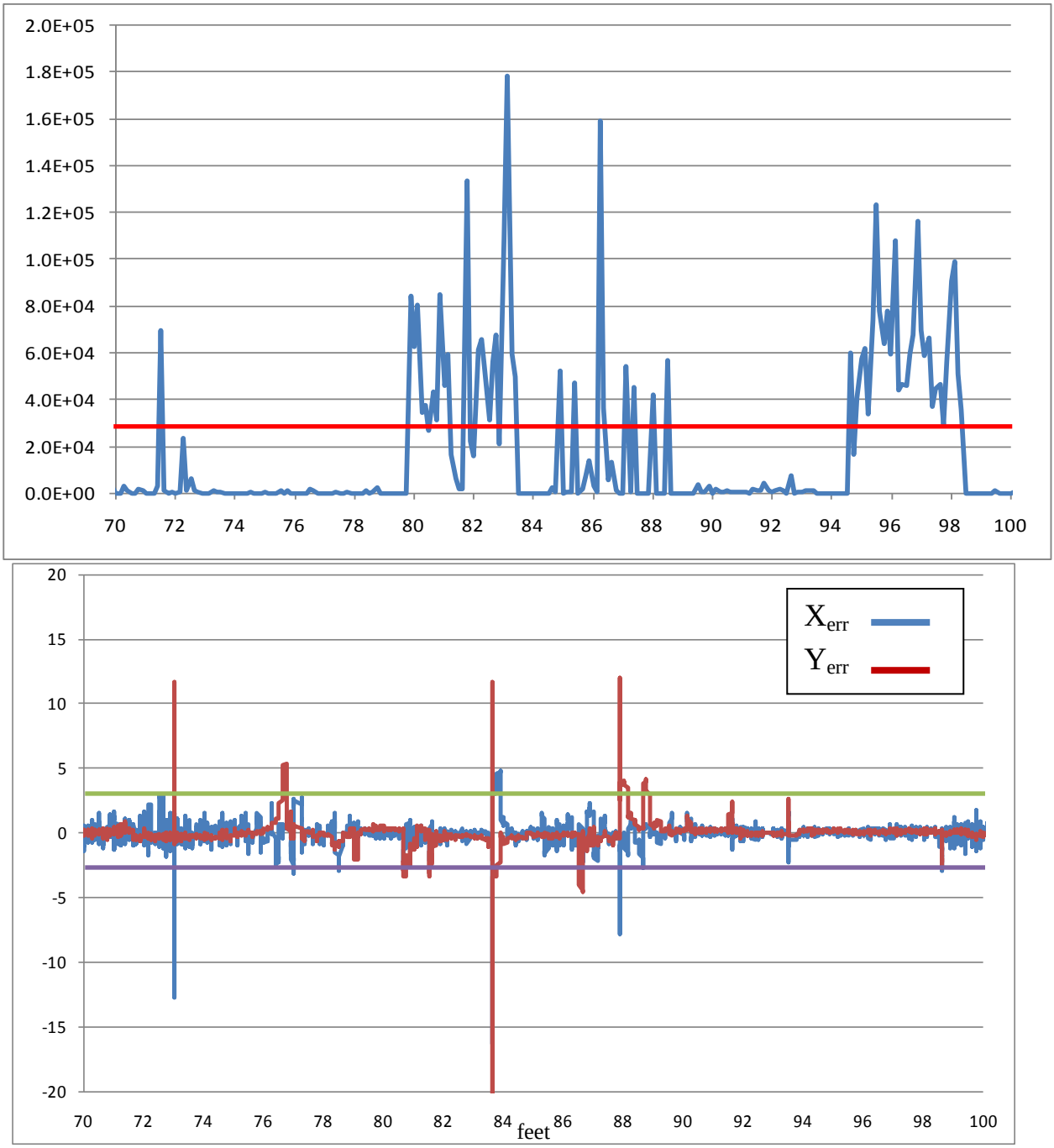

Figure 8.16. Results of a Defect Detection Run on the GET Defect Farm (run #44) with the Related Servo-Log Data

[Showing data zoom in the track area where the TDs are located (feet 70–100). Joints have been purged from the graph.]

9. Sixth Field Test (Transportation Technology Center, Pueblo, CO, June 2009)

The sixth field test occurred at the Transportation Technology Center (TTC) for 7 days between June 24 and 30, 2009. UCSD and ENSCO teams were actively involved in testing the prototype, whereas personnel from TTCI provided the logistics support of the test.

9.1 Days #1 and #2. System Setup

Days #1 and #2 were spent by UCSD and ENSCO teams setting up the prototype on R-4 in the TMB building of TTC (Figure 9.1); on day #2, ENSCO encountered problems with one of the servo-motors, hence, it was decided to start testing with the cart.

Figure 9.1. R-4 in the TMB Building (TTC)

The installation of the cart on R-4 was smooth; the prototype was mounted on the cart beam (Figure 9.2) and the laser sensor, used for tracking the position of the cart relative to the rail, was mounted off-center on the cart beam to allow for a closer installation of the ultrasonic transducers (Figure 9.3).

Figure 9.2. The Cart with the Prototype Installed before Cabling

Figure 9.3. ENSCO Laser Positioning Sensor Mounted on the Cart Beam

Figure 9.4 shows a detail of the cart new nylon wheel flanges, required to eliminate any noise eventually generated by the friction between the wheel and the rail during an inspection.

Figure 9.4. Detail of the New Nylon Wheel Flanges Required for Noise Reduction

As required by UCSD, ENSCO installed a 50-gallon water tank on the front of R-4 to supply a water spray system needed to improve the ultrasonic generation in the rail (Figure 9.5).

Figure 9.5. The 50-Gallon Water Tank for the Water Spray System Mounted on the Front of R-4

9.2 Days #3 and #4. Calibration and Troubleshooting of ENSCO Positioning System (tachometer system)

During days #3 and #4, UCSD and ENSCO encountered problems with the tach system.

The following issues were affecting the reliability of the prototype position along the track:

- ENSCO software was not capable of acquiring the tachometer pulse with a resolution of 0.5 in at an average inspection speed of 2.5 mph; hence, data was randomly lost during the acquisition.
- ENSCO encoder appeared to be slipping or nonrotating in some parts of the Balloon-Loop track; hence, for those areas, data was not collected, and a positioning error as large as 215 ft over 4,200 ft was accumulated during the inspection of the Balloon-Loop Inside rail. During the inspection of the outside rail, the accumulated error was much smaller, on the order of 25 ft over 4,200 ft.

The first problem was solved by changing ENSCO encoder resolution from 0.5 to 0.75 in and limiting the inspection speed to 2 mph; no solution was found to address the second issue. Attempting to solve these problems was extremely time-consuming, because several runs were performed over known distances, trying to calibrate the encoder, but inconsistent results were produced by the tachometer system, making the troubleshooting process very difficult.

Time and effort were also invested trying to obtain a reliable mapping of the Technology Development Section (Calibration Zone) of the Balloon Loop; some delay was at first encountered by UCSD and ENSCO in obtaining the mapping of that section from TTCI; this prompted UCSD to manually remap the defects in the Calibration Section, walking along the rail and looking at the defect tags written on the side of the rail. TTCI first provided UCSD with only 60 ft (with no TDs included) of mapping of the Calibration Section, which actually extends for more than 1,200 ft.

Figure 9.6 shows a representative example of the good performance of the cart to track the rail; the vertical and horizontal errors were within tolerance (±3.1 mm) for more than 98 percent of the time. In the proximity of joints or crushed rail heads though, it still occurred that the system was for a very short time out of the required tolerance.

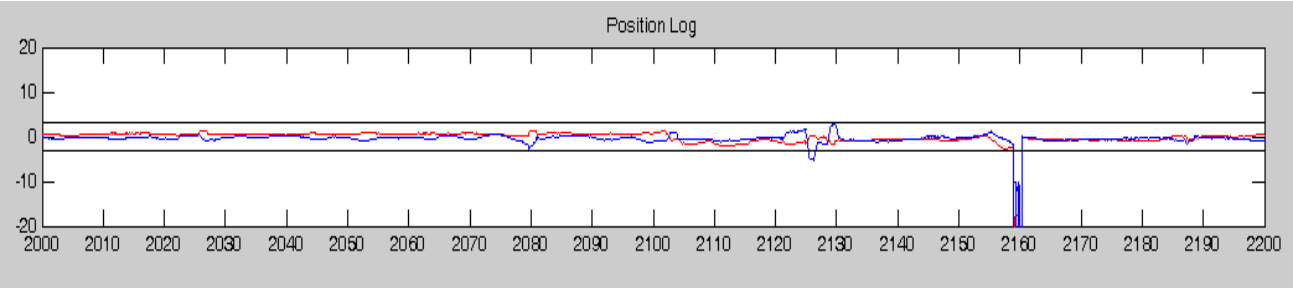

Figure 9.6. X-Y plot (mm) of the Cart Position Relatively to the Rail (X = red; Y = blue)

Table 9.1 contains the schedule of the runs performed during the entire period at TTC. Twelve runs on the Calibration Zone were completed in days #3 and #4; only run #12 was usable for defect detection, because all the remaining runs were performed in the attempt to solve the issues with ENSCO positioning system.

Table 9.1. Schedule of the Runs Performed during the Entire Period at TTC

Test #	Day #	Date	Time [EST]	Rail [Inside/ Outside]	Rail Head Area [CG=Center+Gage CF=Center+Field]	Conditions [Wet/Dry]	Distance resolution [in]	Notes
1	3	Friday June 26th	18:05	Inside	CG	Dry	0.5	Tach System Troubleshooting
2	3	Friday June 26th	18:31	Inside	CG	Dry	0.5	
3	3	Friday June 26th	19:57	Inside	CG	Dry	0.5	
4	3	Friday June 26th	21:16	Inside	CG	Dry	0.5	
5	4	Saturday June 27th	11:25	Inside	CG	Dry	0.5	
6	4	Saturday June 27th	15:11	Inside	CG	Dry	0.5	
7	4	Saturday June 27th	15:20	Inside	CG	Dry	0.5	
8	4	Saturday June 27th	15:43	Inside	CG	Dry	0.5	
9	4	Saturday June 27th	17:26	Inside	CG	Dry	0.5	
10	4	Saturday June 27th	19:52	Inside	CG	Dry	0.75	
11	4	Saturday June 27th	20:03	Inside	CG	Wet	0.75	
12	4	Saturday June 27th	20:13	Inside	CG	Wet	0.75	Technology Development Section
13	5	Sunday June 28th	15:31	Inside	CG	Wet	0.75	Aborted**
14	5	Sunday June 28th	15:35	Inside	CG	Wet	0.75	Technology Development Section
15	5	Sunday June 28th	15:49	Inside	CG	Wet	0.75	System Evaluation section
16	5	Sunday June 28th	16:42	Inside	CG	Wet	0.75	
17	5	Sunday June 28th	20:11	Inside	CG	Wet	0.75	
18	5	Sunday June 28th	20:39	Inside	CG	Wet	0.75	
19	5	Sunday June 28th	21:23	Outside	CG	Wet	0.75	
20	5	Sunday June 28th	21:48	Outside	CG	Wet	0.75	
21	5	Sunday June 28th	22:21	Outside	CG	Wet	0.75	
22	5	Sunday June 28th	23:32	Outside	CF	Wet	0.75	
23	5	Sunday June 28th	23:58	Outside	CF	Wet	0.75	
24	5	Sunday June 28th*	0:31	Inside	CF	Wet	0.75	
25	5	Sunday June 28th*	0:55	Inside	CF	Wet	0.75	
26	7	Tuesday June 30th	12:11	Inside	CG	Wet	0.75	Aborted**
27	7	Tuesday June 30th	12:13	Inside	CG	Wet	0.75	Technology Development Section
28	7	Tuesday June 30th	12:33	Inside	CG	Wet	0.75	
29	7	Tuesday June 30th	12:57	Inside	CG	Wet	0.75	
30	7	Tuesday June 30th	13:15	Inside	CG	Dry	0.75	
31	7	Tuesday June 30th	13:21	Inside	CG	Dry	0.75	
		*Test run late evening of Day 5						** Excessive Misalignment of System Position

9.3 Days #5, #6, and #7. System Evaluation

On day #5, 13 runs were performed on the Balloon Loop; 1 run was aborted because of tachometer-related problems (#13), 1 was performed on the Calibration Zone (#14), and the remaining 11 were acquired on the System Evaluation Zone (#15–25, green background in Table 9.1). Six runs were performed on the inside rail, whereas the remaining five runs inspected the outside rail. For each rail, the prototype sensor configuration was modified to inspect the Gage/Center and the Field/Center sides of the rail head.

The alignment problems mentioned earlier were still encountered during the analysis of the data acquired during the System Evaluation runs; a careful analysis had to be performed on the results, attempting to realign the data looking at the position of detected joints.

On day #6, UCSD analyzed the results of the 11 System Evaluation tests and submitted the data for review to the government representatives Luis Maal (FRA) and John Choros (Volpe Center). The analysis of the results showed that the system picked up welds along the track. As a result, it was later decided to resubmit the data to the government representatives, after removing all the detections related to known defect-free welds.

During day #7, six runs were performed on 700 ft of the Calibration Zone, where all the known TDs were located; one of the runs was aborted because of tachometer-related problems (#26), whereas five runs were successfully recorded (#27–31).

Table 9.2 lists the discontinuities within the inspected track; 15 TDs are included.

For each of the seven tests considered (yellow background in Table 9.1), the right columns of Table 9.2 show an X mark when the defect on the related row was detected. For each test, the POD (POD [%]) was calculated as the ratio of detected TDs over the total number of available TDs. The number of false positives was also counted for each test.

The conclusion is that for a 700-foot run, on a track containing 15 TDs ranging from 5 to 75 percent head area reduction, the system showed an average POD of approximately 73 percent with 10 false-positive calls; both the values have been averaged over seven runs. Some of the defect detections that were considered false-positive calls may be related to defects or discontinuities not reported in the mapping (many defects had to be added to the list initially provided by TTCI); for example, potential discontinuities not reported could be the ones detected with high redundancy at locations 223, 402, 475, and 542 ft.

The computation of the false positives does not take into account peaks not related to TDs but related to other defects or discontinuities like joints or welds. Clearly, one area of the graph (rail plug between joints at 373.51 and 411.85 ft) is really noisy in all the seven tests, and it is not usable for defect detection. After visual inspection of that piece of rail, it can be deduced that the system is too sensitive to heavy shelling of the top of the rail head.

Figures 9.7 and 9.8 show the raw data related to the D.I. related to two sample runs, respectively, #12 and #14.

Table 9.2. Details of Fifth Field Test Runs, May 2009 (days #3–4)

TTC Technology Development section												
List of Discontinuities				Positive detections of Transverse Defects (TDs)								
INSIDE RAIL				Run #	12	14	27	28	29	30	31	
Tie #	Flaw	Flaw Size	Dist (ft)									
	Joint		0 (469.62 from ZERO of RTDF)									
	Weld		5.38									
	Weld		27.38									
	Weld		61.38									
	Weld		70.38									
	Weld		108.38									
	Head chip		109.56									
	Weld		134.38									
376	**TD w/shell**	**5%**	**138.74**		X	X	X	X	X	X	X	
	Weld		144.38									
383	**Crushed Head w/TD**	**5%**	**150.90**		X	X	X	X	X	X	X	
	Weld		154.38									
	Weld		168.33									
	Weld		204.68									
	Weld		227.59									
	Weld		241.38									
	Weld		249.38									
455	**TD notch (Ih)**	**0.75in.**	**267.93**									
	Weld		280.38									
	Weld with Shell		306.38									
	Joint		326.19									
`	**HSD w/TD notch**	**10in./0.75in.**	**333.17**		X	X	X	X	X	X	X	
	Detail fracture (TD)	**10%**	**340.00**		X	X	X	X	X	X	X	
	Weld		349.38									
	Joint		355.08									
512	**HSD w/TD**	**10in./20%**	**359.06**		X	X	X	X	X	X	X	
	Joint		373.51									
	Joint		411.85									
	Head chip		416.38									
555	**TD notch (Gage S. Upp. H.)**	**0.75in.**	**429.28**		X	X	X	X	X	X	X	
559	**TD notch**	**0.75in.**	**435.76**		X	X	X	X	X	X	X	
563	**TD (suspect not visible/marked)**	**75%**	**441.73**		X			X	X			
	Joint		444.62									
570	**TD**	**8%**	**454.38**		X	X	X	X	X	X	X	
	Joint		467.43									
	weld		486.55									
598	**TD Notch/artificial shell**		**496.51**		X	X		X	X	X	X	
606	Shell / Eng Burn (Field)		510.96									
610	**TD Notch/artificial shell**		**518.43**					X	X			
	weld		527.39									
	Transverse notch (no shelling)		**530.38**									
623	Artificial shell		537.35									
631	**TD (very small)**		**550.30**			X					X	
637	**TD Notch/artificial shell**		**557.77**		X	X	X	X	X	X	X	
	Joint		569.22									
	Shop weld		587.15									
	Shop weld		597.11									
	Field weld		642.43									
	Shop weld		661.85									
	weld		691.23									
	crushed weld		696.71									
	Joint		699.70									
	LEGEND:			**Sum**	11	11	9	12	12	10	11	
	BHC=Bolt hole crack			**Tot. TDs**	15.00	15.00	15.00	15.00	15.00	15.00	15.00	
	SB=Slotted Base											**Average:**
	SDH=Side drilled hole			**POD [%]**	**73.3**	**73.3**	**60.0**	**80.0**	**80.0**	**66.7**	**73.3**	**72.4**
	HV=Head Void											
	HSD=Head Surface Damage			**False positives**	**11**	**8**	**5**	**9**	**12**	**12**	**12**	**9.9**
	SCH=Saw Cut (head)											
	SCB=Saw Cut (base)											
	VSH=Vertical Split Head											
	HSH=Horizontal Split Head											
	EDH=End Drilled Hole (TD)											
	WSC=Web Saw Cut											
	TD=Transverse Defect											
	TD notch = Artificial TD											

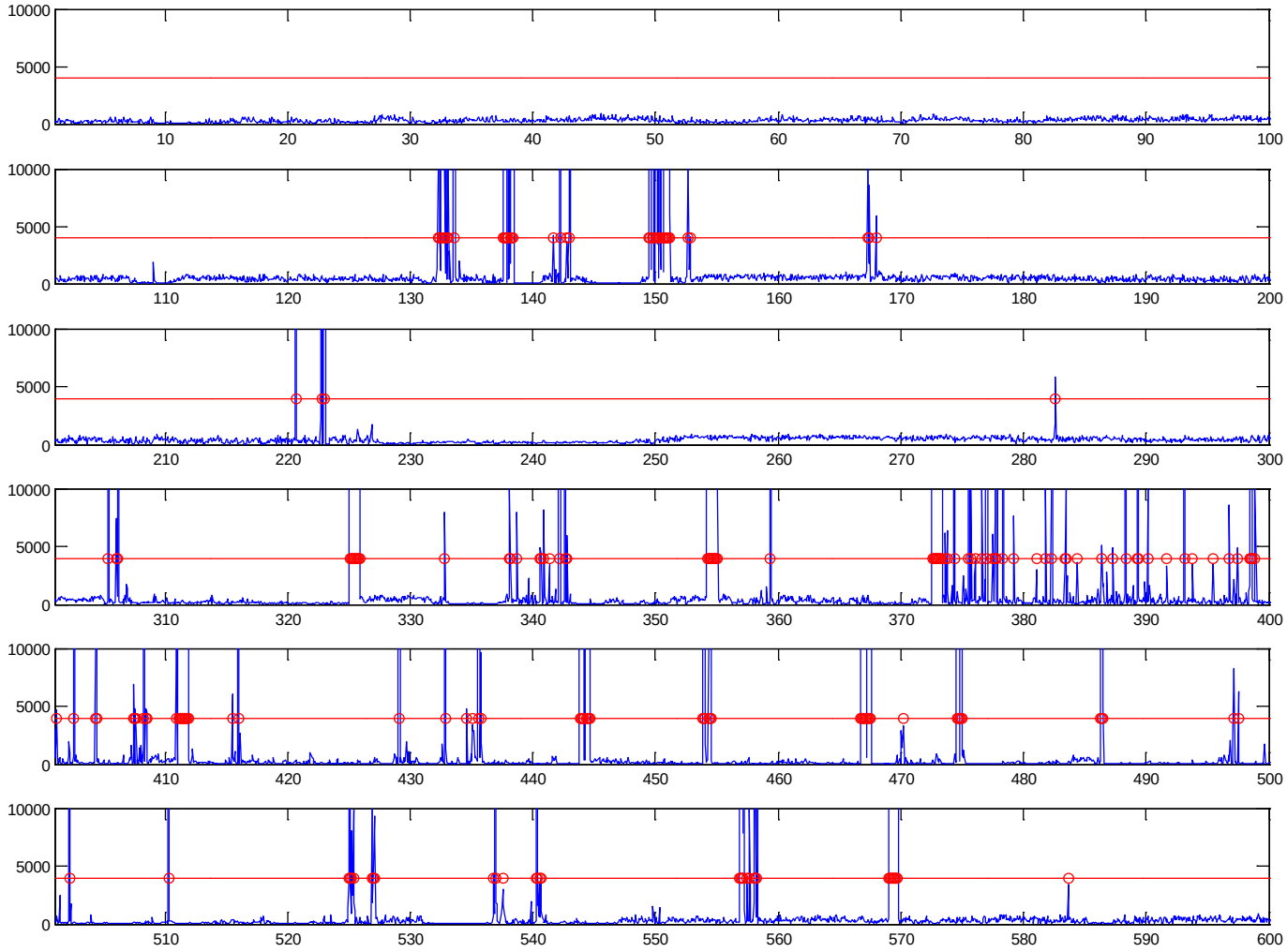

Figure 9.7. Test #12: D.I. Plot

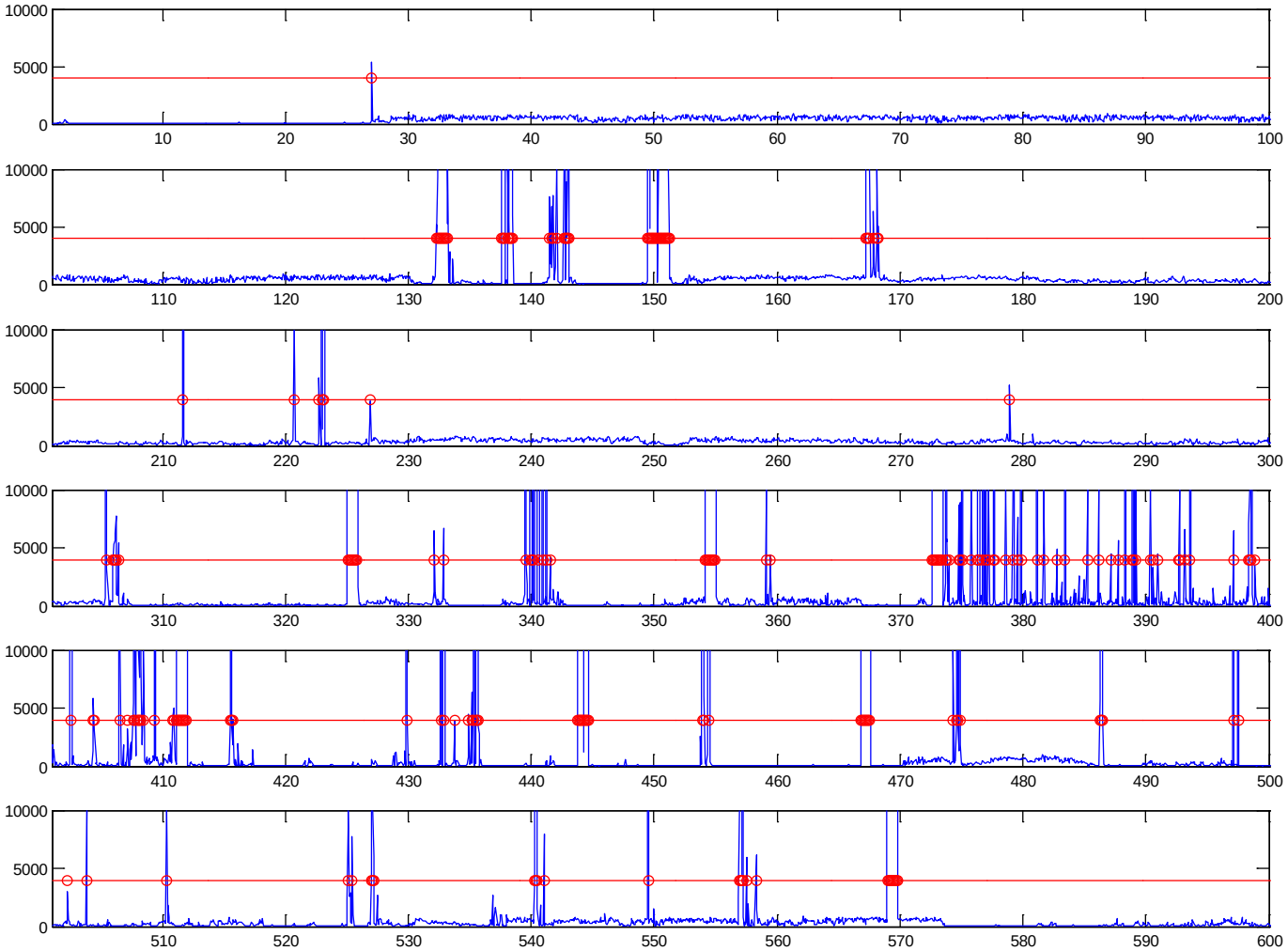

Figure 9.8. Test #14: D.I. Plot

9.4 Conclusions on Prototype Performance during Sixth Field Test

The system performance in the detection of the TDs located in the Calibration Zone was very satisfactory. The size of the detected TDs ranges between 5 and 75 percent of head area reduction and were mainly located in the middle and upper zone of the head. The system was able to detect, reliably, TDs covered by natural shelling (e.g., TDs at locations 138.74, 333.17, and 359.06 ft) and artificial shelling (e.g., TDs at locations 496.51 and 557.77 ft). However, the system was very sensitive to the presence of heavy shelling on the top of the rail head; this "noisy" behavior was never experienced before since the prototype was never tested in a rail with a similar heavy-shelling condition. The prototype was also sensitive to noise generated by the friction between wheel and rail, especially when R-4 was on a curved piece of track. A solution to this problem could be spraying water on the R-4 wheels closest to the prototype to avoid or minimize the noise generation. The system defect-detection was also triggered by defect-free welds; this seems to be a common problem among rail inspection system, and it could be solved by using an existing vision system or another device with a similar concept.

10. Seventh Field Test (Herzog Services Defect Farm, St. Joseph, MO, June 2010)

10.1 Seventh Field Test Timeline

The seventh field test occurred at Herzog Services, Inc., for 6 days between June 13 and June 18, 2010. UCSD and ENSCO teams were actively involved in testing the prototype, whereas Herzog Services provided access to their facility, including the rail defect farm, to accommodate the tests. In addition, representatives from BNSF Railway, Union Pacific Railroad (UP), FRA, and the Volpe Center observed the tests.

Day #1 and part of day #2 were spent by UCSD and ENSCO teams setting up the prototype on R-4 in Herzog Services' main building. R-4 was equipped with a new system of nozzles spraying water at the four R-4 wheel locations, aiming at reducing the noise occurring at the wheel-rail interface. The water reservoir was installed in the front of R-4 (Figure 10.1).

Figure 10.1. Water Reservoir for the Supply of the Water Spray System Installed to Reduce the Noise Created at the Wheel-Rail Interface

On day #2 ENSCO personnel installed reflective targets on the track to mark 20-foot blocks, welds, and joints.

The new positioning system installed by ENSCO on R-4 was tested, and it performed satisfactorily at the necessary resolution. At the end of day #2, two blind tests were conducted as previously agreed with Herzog. The results of the blind tests were submitted to staff

members observing the tests, J. Choros, Leith Al-Nazer, Carlo Patrick, and T. Elbert, representing Volpe Center, FRA, and Herzog, respectively.

In the morning of day #3, several tests were run with the purpose of testing multiple system configurations, varying from different sensor sets and new settings for the ultrasonic signal time gating.

During day #3, after Mr. Elbert released a list with the known defect locations, ENSCO installed and tested reflective targets near the flaws (Figure 10.2).

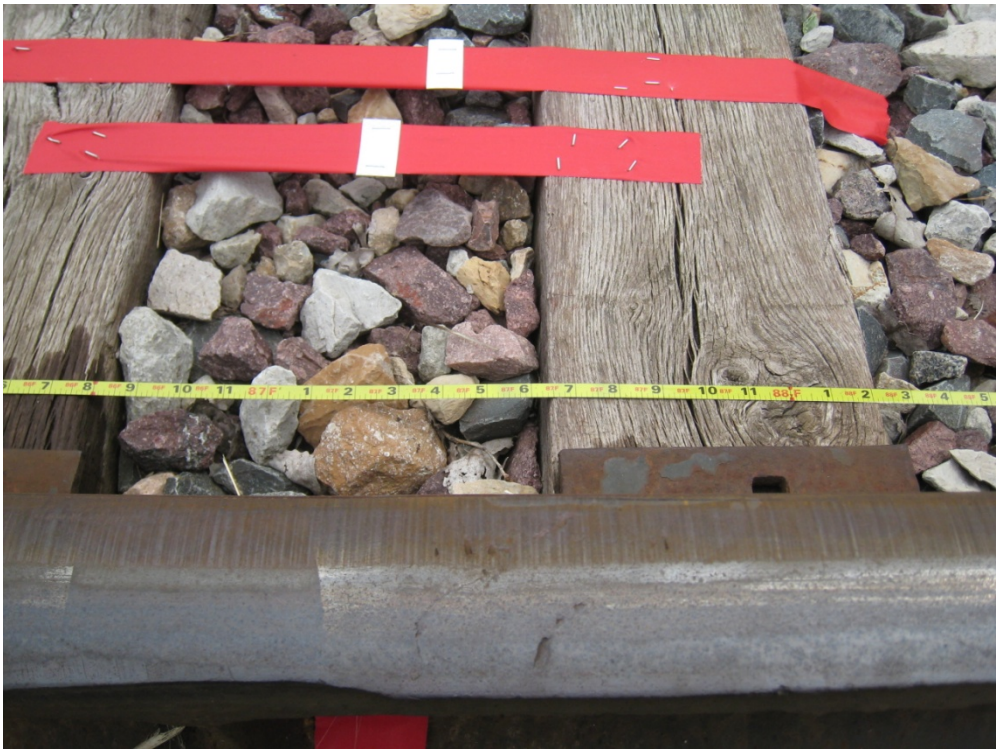

Figure 10.2. Reflective Targets Placed in Correspondence of Joints, Weld, and Defects

The rest of day #3 was spent comparing UCSD results to Herzog's list of known defects. In the morning of day #4, a different set of sensors responding at higher frequency was installed, and several tests were run to assess the new configuration. During the day, the prototype performance was demonstrated to representatives of BNSF, UP, as well as to several Herzog employees. At the end of the day, the initial sensor setting was reinstalled on the prototype.

The beginning of day #5 was spent running several tests showing the prototype performance to representatives of BNSF and UP. In the afternoon, a new configuration with the sensors slightly moved toward the field side of the rail head was also tested.

In the morning of day #6, the prototype was tested at a higher speed (~8–9 mph), and later, the sensors were moved back toward the gage side of the rail head. More runs at a higher speed were conducted before concluding the field test. Some problems with the flanging of the cart occurred during the latest higher speed tests. These were solved by adjusting the pressure of the actuators installed on the cart.

Figure 10.3 shows pictures of the UCSD prototype as well as a group picture of participants to the tests.

Figure 10.3. The UCSD Prototype at Herzog and Picture of Some of the Test Participants and Observers from UCSD, ENSCO, FRA, Volpe Center, Herzog, BNSF Railway, and UP

10.2 Description of Testing Area and Mapping of the Track

Figure 10.4 shows an aerial view of Herzog railroad track testing facility. Areas 1 (Tangent) and 2 (Spiral) were composed of 136 RE rails, whereas the track in areas 3 and 4 had smaller rail sections (115 and 90 RE, respectively).

Figure 10.4. Aerial View of Herzog Railroad Track Testing Facility (rail defect farm)

Table 10.1 contains the mapping of the test zone. Joints, welds, 20-foot distance marks, and defects detected by the blind tests performed on day #2 are included in the table.

Table 10.2 contains the schedule of the runs performed during the entire period at Herzog. A total of 54 tests were performed, running the prototype in the different areas of the track. Most of the tests were run up to the track spiral (Area 2), whereas a few were extended to the curve (Areas 3 and 4). Some runs were limited to the area with the frog (within Area 1). Most of the tests were run at walking speed. A few tests at 5 and 9 mph were run to assess the dependence of the prototype performance on speed. The distance positioning resolution was maintained at 0.25 in for all the runs.

Table 10.1. Mapping of the Test Zone

Tie Number/Event Catalog at Hezog Test Facility

Date: June 14, 2010

NOTE: Tie Numbering starts at "0"

DM = Distance Marker

LE = Leading Edge of Tie (in Direction of Increasing Tie Count)

TE = Trailing Edge of Tie (in Direction of Increasing Tie Count)

Tie	Event Description
0	UCSD Laser Position at Start of Test
1	0 DM at TE of Tie 1
7	**UCSD DEFECT FROM BLIND TEST (9' 2")**
12	20' DM at TE of Tie 12
14	**UCSD DEFECT FROM BLIND TEST (24' BETWEEN TIE 14 & 15)**
18	**UCSD DEFECT FROM BLIND TEST (29' 6" ON TIE 18)**
20	**Joint** at LE of Tie 20
22	**UCSD DEFECT FROM BLIND TEST (37' ON TIE 22)**
23	**UCSD DEFECT FROM BLIND TEST (39' ON TIE 23)**
23	40' DM 10" after TE of Tie 23
25	**UCSD DEFECT FROM BLIND TEST (43' ON TIE 25)**
27	**UCSD DEFECT FROM BLIND TEST (46' ON TIE 27)**
32	**UCSD DEFECT FROM BLIND TEST (55' 2" ON TIE 32)**
34	**Weld** 2.5" after TE of Tie 34
	UCSD DEFECT FROM BLIND TEST (59' 2" BETWEEN TIE 34 & 35)
	60' DM 12" after TE of Tie 34
42	**Joint** on Tie 42
46	80' DM 5" after TE of Tie 46
50	**Weld** 6" after TE of Tie
	UCSD DEFECT FROM BLIND TEST (87' 4" BETWEEN TIE 50 & 51)
55	**Weld** at LE of Tie 55 on Tie
56	**Joint** at TE of Tie 56 on Tie
57	100' DM 6" after TE of Tie 57
58	**Weld** 5" after LE of Tie 58 on Tie
62	**Weld** 11" after TE of Tie 62
68	120' DM 2.5" after LE of Tie 68 on Tie
72	**Joint** 13.5" after TE of Tie 72
73	**Start of Frog**
78	140' DM 8" after TE of Tie 78
81	**Joint** 3" after LE of Tie 81 on Tie
	End of Frog
85	**Start of Guard Rail**

Tie	Event Description
88	160' DM 1" after TE of Tie 88
90	**End of Guard Rail**
92	**Joint** 14" after TE of Tie 92
94	**Weld** 14" after TE of Tie 94
95	**UCSD DEFECT FROM BLIND TEST (174' ON TIE 95)**
98	180' DM 3" after LE of Tie 98 on Tie
101	**UCSD DEFECT FROM BLIND TEST (186' 6" BETWEEN TIE 101 & 102)**
103	**Joint** 5" after LE of Tie 103 on Tie
106	**Weld** 7" after LE of Tie 106 on Tie
	UCSD DEFECT FROM BLIND TEST (194' BETWEEN TIE 106 & 107)
	UCSD DEFECT FROM BLIND TEST (195' 3" BETWEEN TIE 106 & 107)
110	200' DM 5" after TE of Tie 110
113	**Joint** 0.5" after LE of Tie 113 on Tie
116	**Weld** 8" after LE of Tie 116 on Tie
123	220' DM 2" after TE of Tie
127	**UCSD DEFECT FROM BLIND TEST (230' 6" BETWEEN TIE 127 & 128)**
130	**Joint** 3" after LE of Tie 130 on Tie
135	240' DM 5.5" after LE of Tie 135 on Tie
138	**Weld** 0.5" after TE of Tie 138
139	**Joint** 1.5" after TE of Tie 139
147	280' DM 3" after LE of Tie 147 on Tie
151	**Joint** 2" after TE of Tie 151
159	280' DM 0.5" after LE of Tie 159 on Tie
160	**Joint** 7.5" after TE of Tie 160
169	300' DM 9" after TE of Tie 169
180	320' DM 1.5" after LE of Tie 180 on Tie
	Joint 6" after TE of Tie 160
190	340' DM on LE of Tie 190 on Tie
199	**Joint** 1.5" after LE of Tie 199 on Tie
	360' DM 17" after TE of Te 199
209	380' DM 13" after TE of Tie 209
217	**Joint** 2.5" after TE of Tie 217
219	400' DM 14" after TE of Tie 219

Table 10.2. Schedule of the Runs Performed during the Test at Herzog Services

Test #	Day #	Date	Speed [MPH]	End of test area	Distance resolution [in]	Test type
1	2	Monday June 14th	2	spiral	0.25	Baseline
2	2	Monday June 14th	2	spiral	0.25	Baseline
3	2	Monday June 14th	2	spiral	0.25	Baseline
4	2	Monday June 14th	2	spiral	0.25	tack pulse check
5	2	Monday June 14th	2	spiral	0.25	tack pulse check
6	2	Monday June 14th	2	curve	0.25	noise check
7	2	Monday June 14th	2	spiral	0.25	noise check
8	2	Monday June 14th	2	spiral	0.25	overall check
9	2	Monday June 14th	2	spiral	0.25	Blind test #1
10	2	Monday June 14th	2	spiral	0.25	Blind test #2
11	3	Tuesday June 15th	2	spiral	0.25	Damage Index
12	3	Tuesday June 15th	2	spiral	0.25	Damage Index
13	3	Tuesday June 15th	1	spiral	0.25	Damage Index
14	3	Tuesday June 15th	2	spiral	0.25	Damage Index
15	3	Tuesday June 15th	2	spiral	0.25	Damage Index
16	3	Tuesday June 15th	2	spiral	0.25	Damage Index
17	3	Tuesday June 15th	2	spiral	0.25	Damage Index
18	3	Tuesday June 15th	2	spiral	0.25	Damage Index
19	4	Wednesday June 16th	2	spiral	0.25	Baseline
20	4	Wednesday June 16th	2	spiral	0.25	Damage Index
21	4	Wednesday June 16th	2	spiral	0.25	Damage Index
22	4	Wednesday June 16th	2	spiral	0.25	Damage Index
23	4	Wednesday June 16th	2	spiral	0.25	Damage Index
24	4	Wednesday June 16th	2	spiral	0.25	Baseline
25	4	Wednesday June 16th	5	spiral	0.25	Damage Index
26	4	Wednesday June 16th	5	spiral	0.25	Damage Index
27	4	Wednesday June 16th	2	spiral	0.25	Damage Index
28	4	Wednesday June 16th	2	spiral	0.25	Damage Index
29	5	Thursday June 17th	2	spiral	0.25	Damage Index
30	5	Thursday June 17th	2	spiral	0.25	Damage Index
31	5	Thursday June 17th	2	spiral	0.25	Damage Index
32	5	Thursday June 17th	2	spiral	0.25	Damage Index
33	5	Thursday June 17th	2	frog	0.25	Damage Index
34	5	Thursday June 17th	2	frog	0.25	Damage Index
35	5	Thursday June 17th	2	frog	0.25	Damage Index
36	5	Thursday June 17th	2	frog	0.25	Damage Index
37	5	Thursday June 17th	2	frog	0.25	Damage Index
38	5	Thursday June 17th	2	frog	0.25	Damage Index
39	5	Thursday June 17th	2	frog	0.25	Damage Index
40	5	Thursday June 17th	5	frog	0.25	Damage Index
41	5	Thursday June 17th	2	curve	0.25	Damage Index
42	5	Thursday June 17th	2	curve	0.25	Damage Index
43	5	Thursday June 17th	2	spiral	0.25	Baseline
44	5	Thursday June 17th	2	spiral	0.25	Damage Index
45	5	Thursday June 17th	2	spiral	0.25	Damage Index
46	5	Thursday June 17th	5	spiral	0.25	Damage Index
47	6	Friday June 18th	9	spiral	0.25	Damage Index
48	6	Friday June 18th	9	spiral	0.25	Damage Index
49	6	Friday June 18th	9	spiral	0.25	Damage Index
50	6	Friday June 18th	2	frog	0.25	Damage Index
51	6	Friday June 18th	9	spiral	0.25	Damage Index
52	6	Friday June 18th	5	spiral	0.25	Damage Index
53	6	Friday June 18th	5	curve	0.25	Damage Index
54	6	Friday June 18th	5	spiral	0.25	Damage Index

10.3 Results of the Blind Tests

The results of the blind tests performed on day #2 are reported in Table 10.3.

The inspected area included 12 rail-head defects, such as DFs, TDs under shelling, defective field and plane welds, side drilled holes (simulating TDs), horizontal split heads (HSHs), and vertical split heads (VSHs).

Two different signal processing approaches were used for the two tests. One configuration was less sensitive to small rail-head discontinuities (blind test 1, run #9) than the other one (blind test 2, run #10).

As shown in Table 10.3, 10 of 12 defects were correctly detected by blind test #1 ("less sensitive configuration"), whereas 11 of 12 defects were correctly detected by blind test #2 ("more sensitive configuration"). Blind test #1 therefore had an 83.34-percent detection rate with zero false positives (0 F.P.). Blind test #2 had a 91.67-percent detection rate at the cost of four false positives (4 F.P.). However, following hand mapping of the test area, three of the four false positives mapped to shallow defects under shelling, as noted in Table 9.3. Hence, the true false-positive detection for blind test #2 was as low as 1 F.P.

As shown in the table, the UCSD list provided for both blind test #1 and #2 did not include the 80 percent defective plane weld (DFW) at tie #136. However, this defect was correctly detected by the system but not included in the original list, because it was considered a weld. Later in the tests, a method was identified to distinguish "good welds" from "defective weld" based on their different ultrasonic signature. When this differentiation was applied, the last defect at tie #136 was consistently detected as a defect by the system.

Table 10.3. Results of the Two Blind Tests Performed on Day #2

Herzog defect farm June 15, 2010

Transverse defects on gage and center of rail head

feet	inches	tie #	defect		UCSD list 1		UCSD list 2	
9	4	7	90% DF (3 field holes, 2 up to gage)		1	7	1	7
23	11	14	SDH (1/4" dia, 3/4" deep on gage)		1	14	1	14
29	9	18	SDH (1/4" dia, 1/2" deep on gage)		1	18	1	18
33	4	22	2" HSH		1	22	1	22
38	11	23	1' VSH		1	23	1	23
42	8	25	gage TD (10% H.A. very deep)		1	25	1	25
46	1	27	10% DPW (TD in weld center head, width of web)		1	27	1	27
55	0	32	small TD (10% H.A. center head) (newly found)		1	32	1	32
59	2	34	50% DFW (center head width of web)		1	34	1	34
87	2	50	DFW under shelling (10% H.A. center head/field)		0		1	50
193	8	106	TD under shelling (10% H.A.)		1	106	1	106
245	1	136	80% DFW (starts at gage)		0		0	
				Detected	**10**		**11**	
				All	**12**		**12**	
				% detection	**83.33**		**91.67**	
				F.P.	**0**		**4***	*(3 of 4 mapped to shallow defects under shelling at ties # 101, 107 & 127)

feet	inches	tie#
174		95
186	**6**	**101**
195	**4**	**107**
230	**8**	**127**

Figure 10.5 plots the results of the blind tests along with industry average and AREMA Recommendation for reliability of defect detection (particularly TDs). The detection percentage was computed as the number of detected defects divided by the total number of defects of a given size class. The 21- to 40-percent size class was not tested since no defect of such size was present on the track. The plot shows that the UCSD system outperformed both industry average and AREMA recommendations in all defect size classes, including the largest size class of 81–100 percent once the weld differentiation method was implemented.

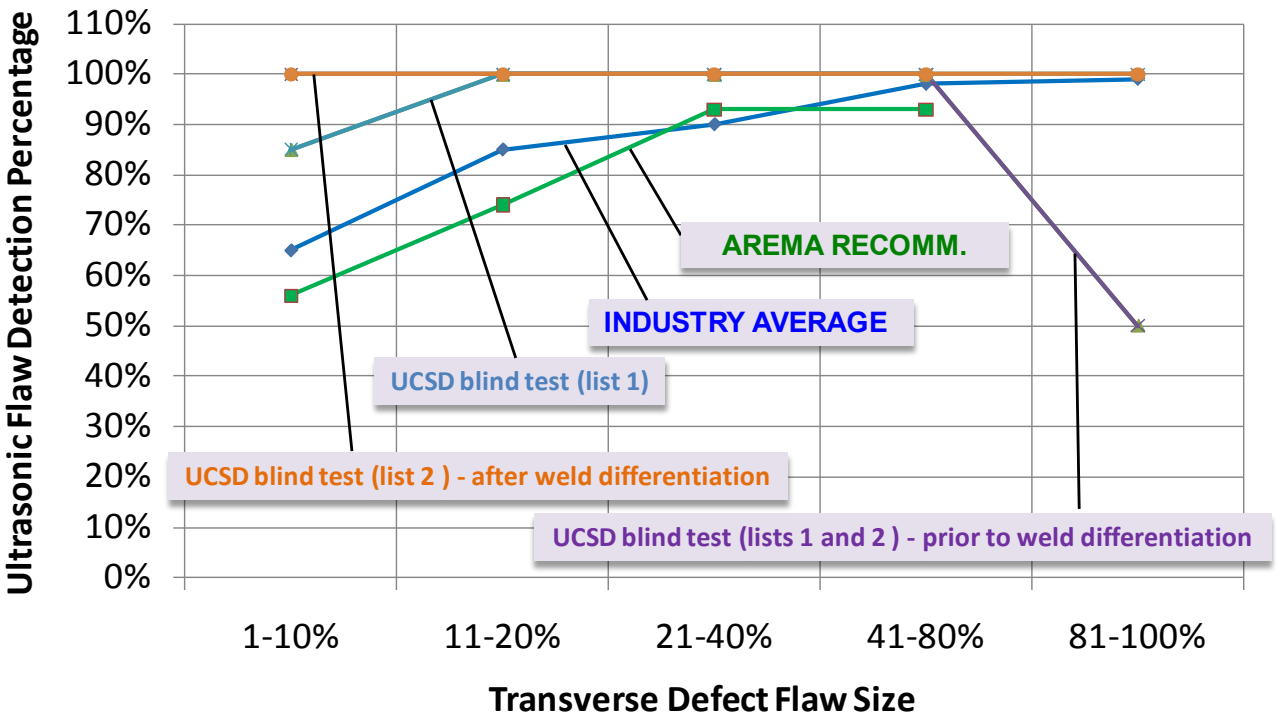

Figure 10.5. Results of UCSD Blind Tests at Herzog Rail Defect Farm on June 15, 2010 (comparison with industry average and AREMA standards)

10.4 D.I. Plots

This section includes the D.I. plots of some sample tests. For display purposes, the plots are reported here as partial zooms of different areas of the track. In addition to the D.I. plots, all raw data was collected during the tests. This raw data is being currently analyzed at UCSD to explore other signal processing strategies for potential further enhancement of the system performance.

10.4.1 Level of Shelling

Different scales of visualization of the D.I. plots were used for different areas of the rail. This is to adapt the response of the system to different levels of shelling of the rail. In the different conditions of shelling encountered during the test, the defect-free level of the D.I. was varying, but the defect indications were always easily distinguishable from the noise level. An automatic gain control feature will be implemented in the final configuration of the system to solve the visualization issue related to rescaling the data in presence of moderate and heavy shelling. Such automatic gain control is also used in conventional ultrasonic rail inspection systems.

The system sensitivity to shelling could also be an interesting feature of the system, potentially used to estimate the severity of shelling; hence, the thickness of the layer that needs to be ground during rail maintenance. This potential for rail surface characterization was highlighted by personnel from the FRA Office of Railroad Safety who attended the tests.

Figure 10.10 shows an example of a rail with a moderate level of shelling. The D.I. increases but the DFW at 87'2" is still well recognizable. Figures 10.6–10.12 show D.I. plots related to run #20, conducted at 2 mph. Figure 10.13 includes the D.I. plot of the full run #20 (feet 0–255).

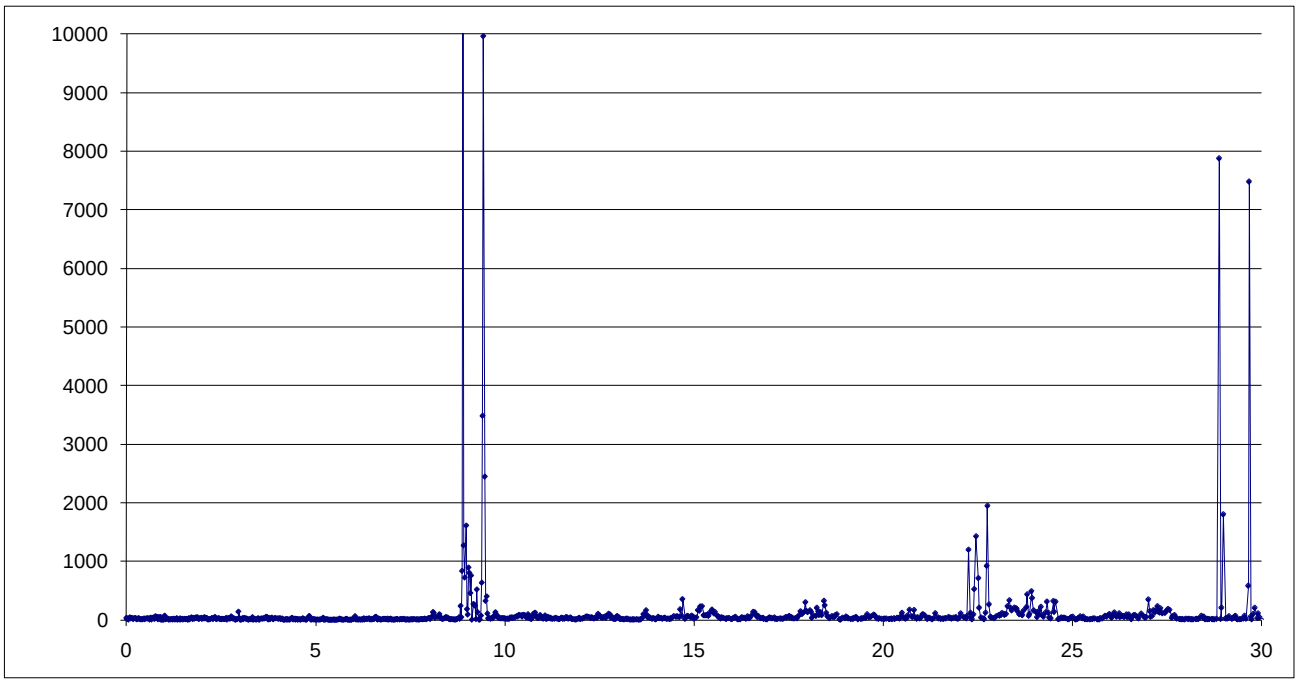

Figure 10.6. D.I. Plot (0–30 ft), Run #20 Conducted at 2 mph

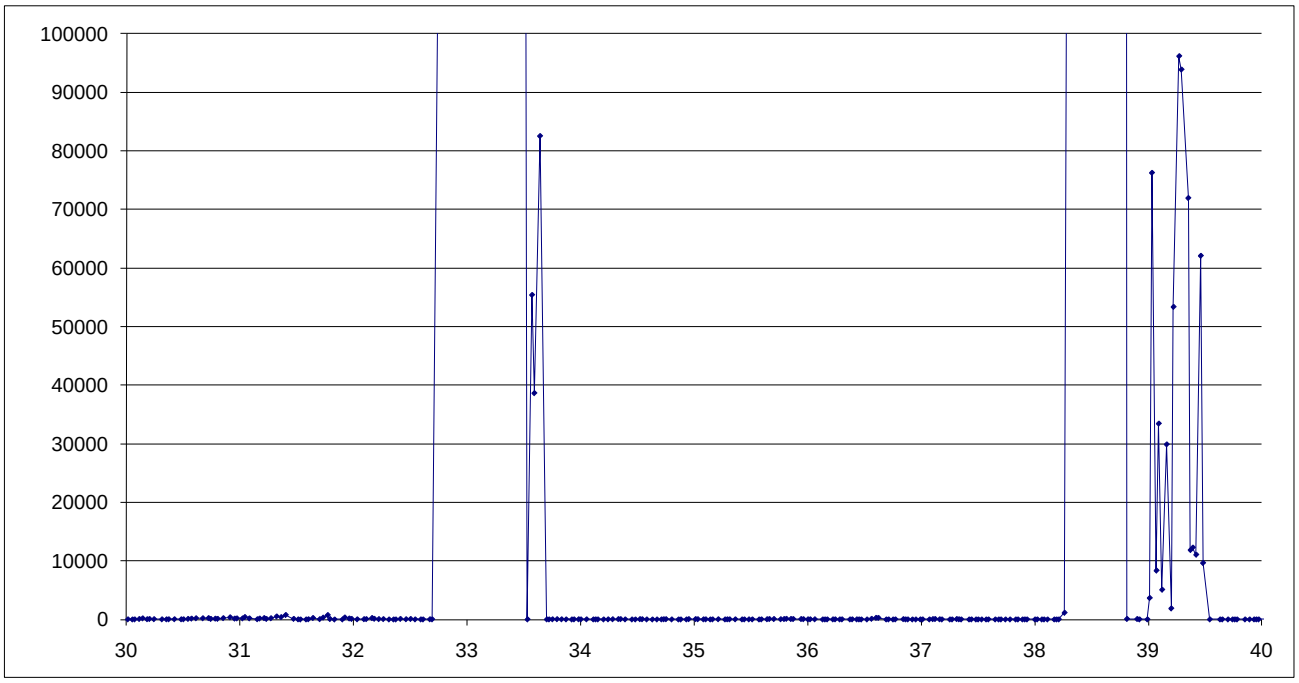

Figure 10.7. D.I. Plot (30–40 ft), Run #20 Conducted at 2 mph

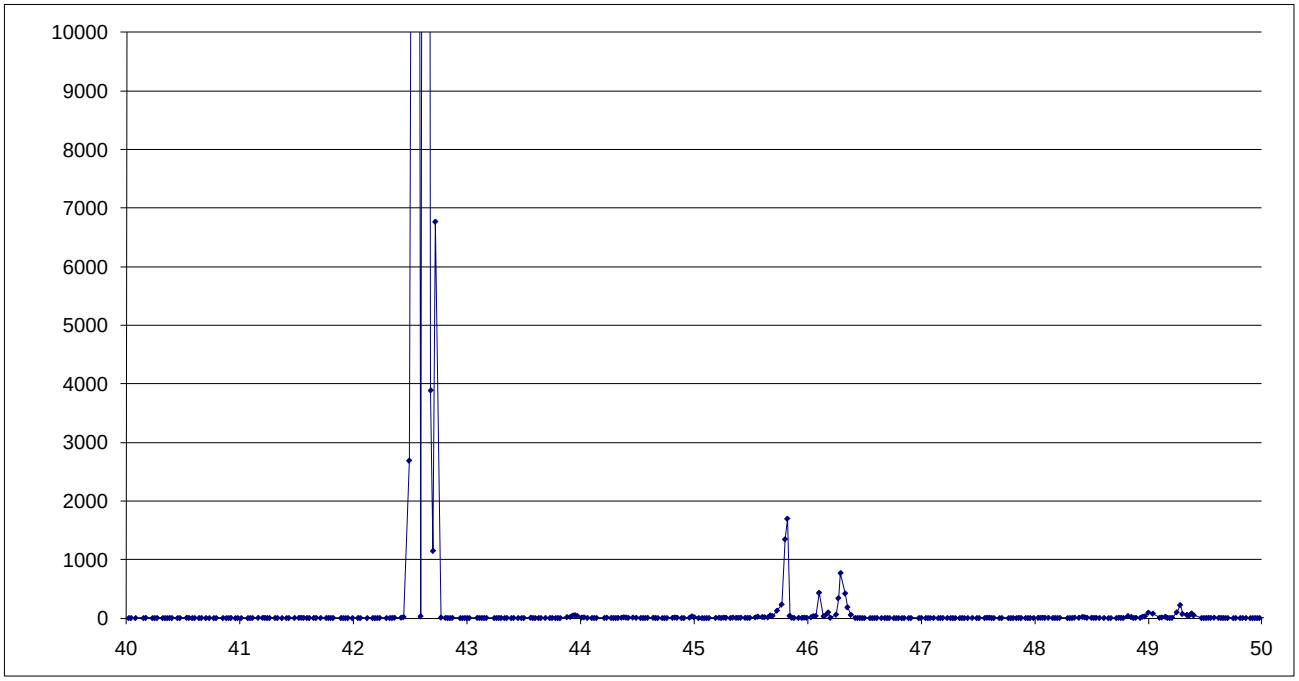

Figure 10.8. D.I. Plot (40–50 ft), Run #20 Conducted at 2 mph

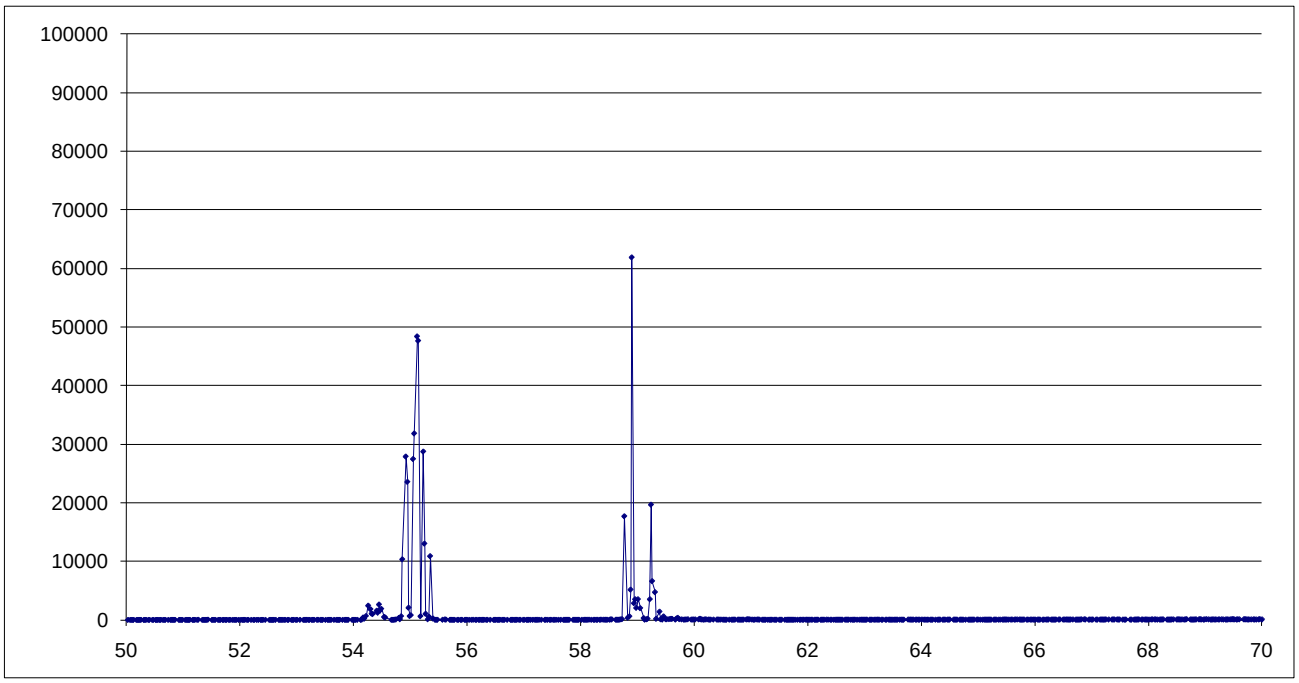

Figure 10.9. D.I. Plot (50–70 ft), Run #20 Conducted at 2 mph

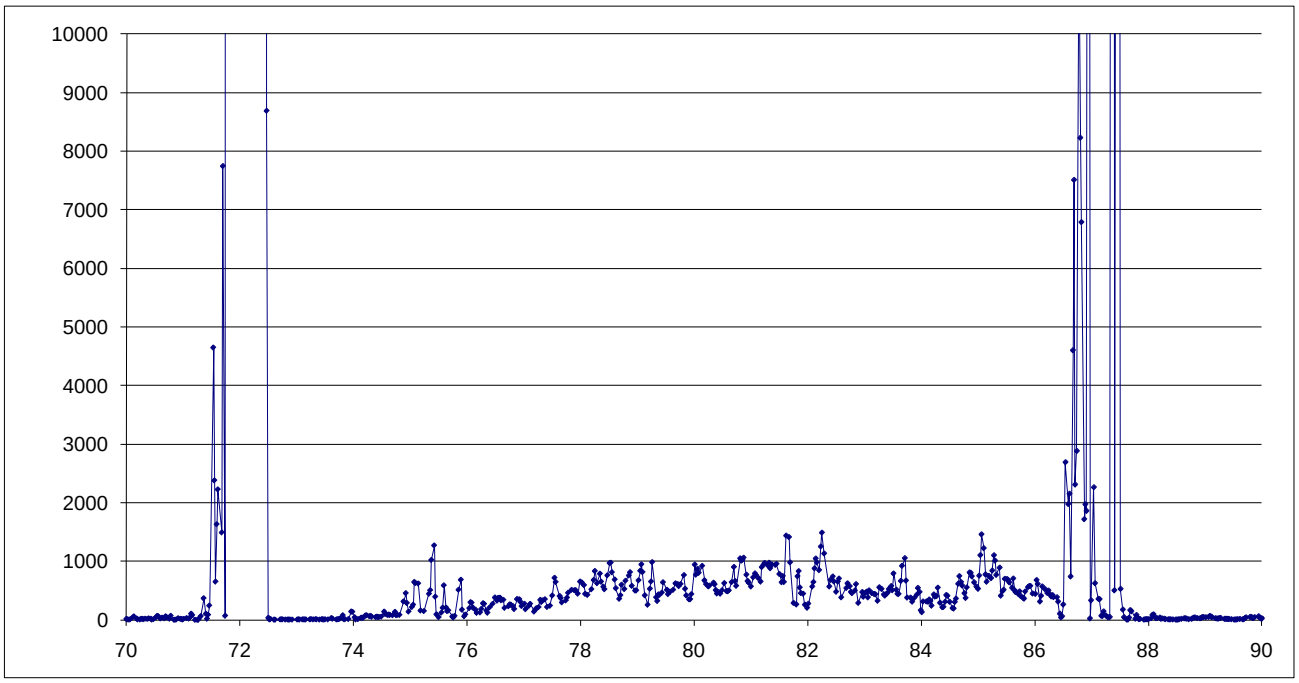

Figure 10.10. D.I. Plot (70–90 ft), Run #20 Conducted at 2 mph

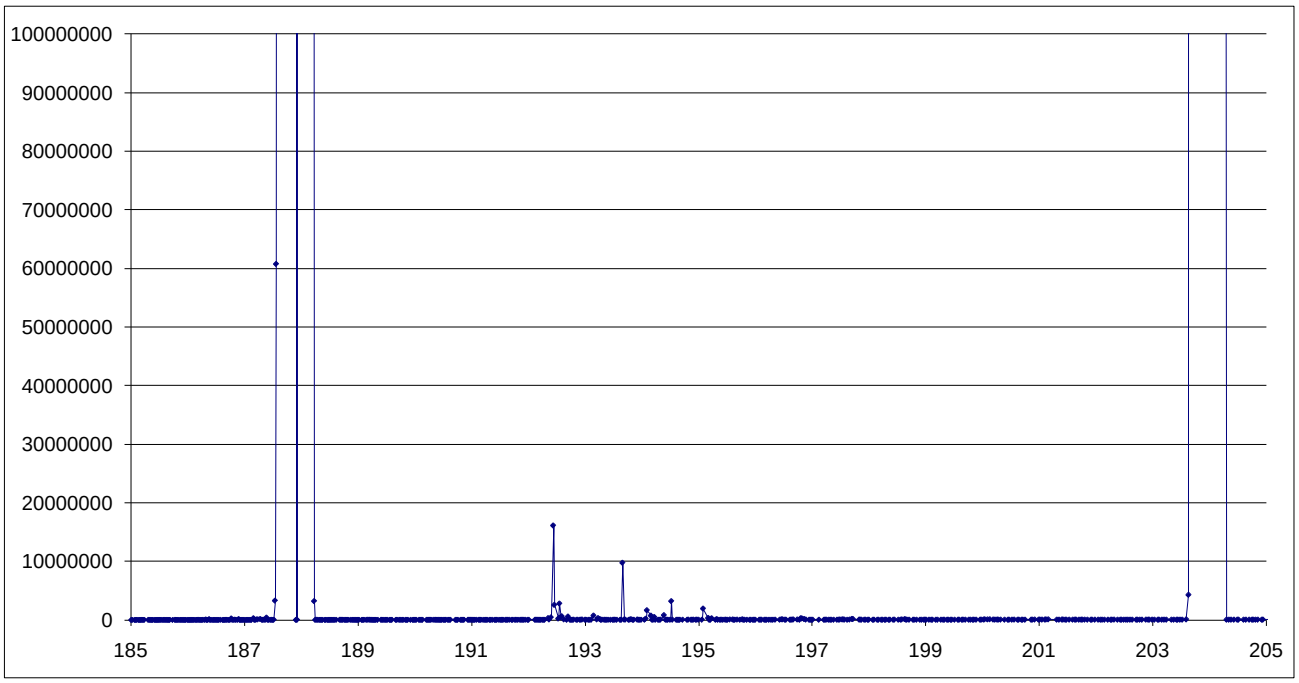

Figure 10.11. D.I. Plot (185–205 ft), Run #20 Conducted at 2 mph

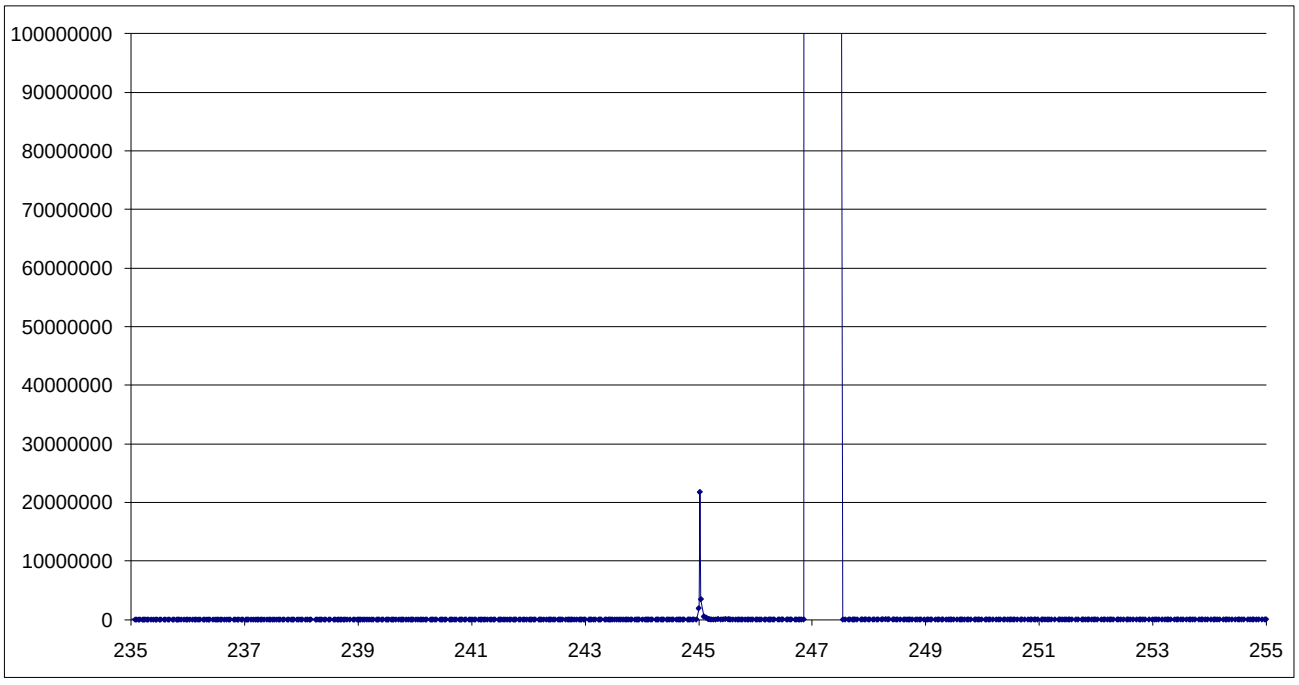

Figure 10.12. D.I. Plot (235–255 ft), Run #20 Conducted at 2 mph

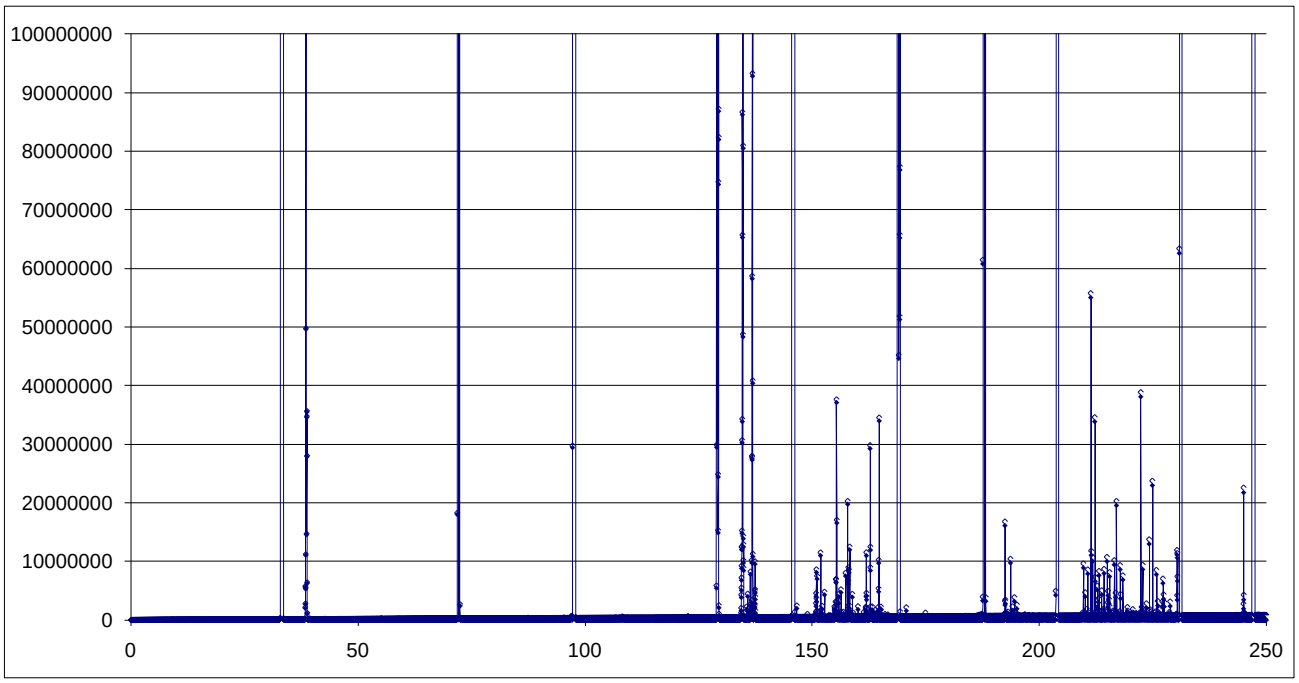

Figure 10.13. D.I. Plot (0–255 ft), Run #20 Conducted at 2 mph

Figure 10.14 includes the D.I. plot of the full run #47 (feet 0–255) conducted at 9 mph, the maximum speed obtainable on the track.

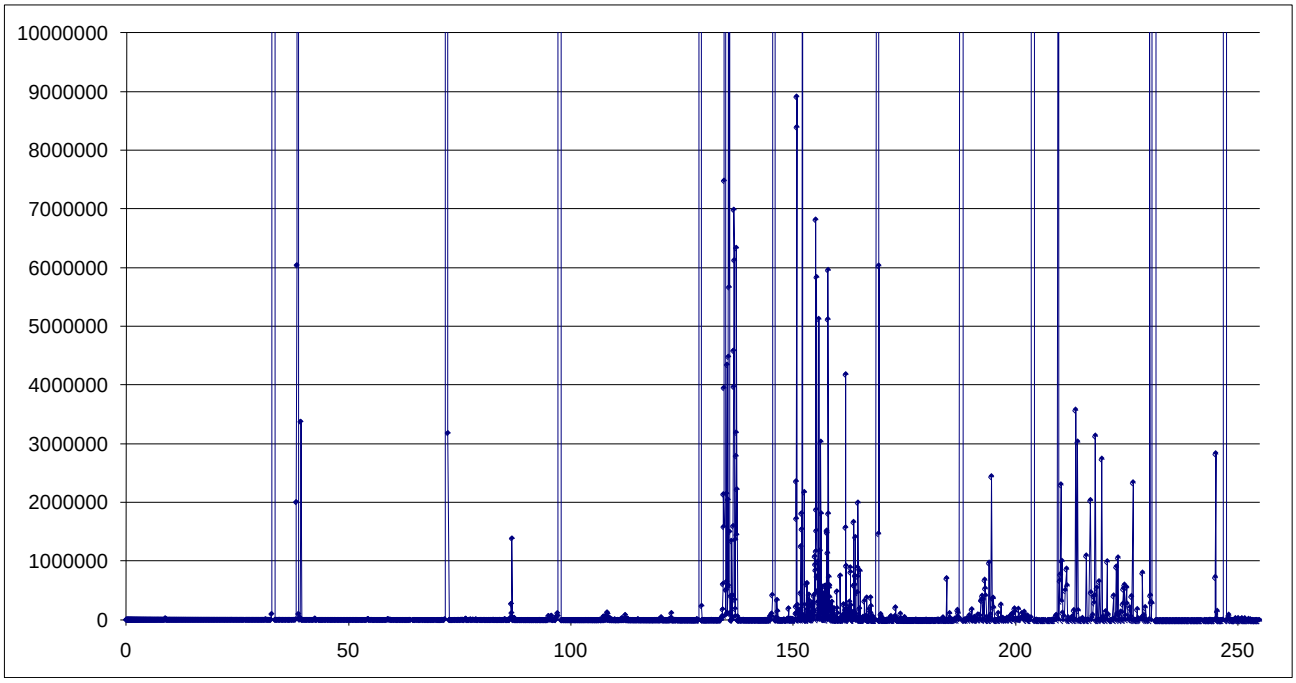

Figure 10.14. D.I. Plot (0–255 ft), Run #47 Conducted at 9 mph

The runs at 9 mph showed that the system is mechanically reliable. Defect detection repeatability at this speed is somewhat reduced because of the degraded position resolution (severely reducing overlapping). Maintaining position resolution at higher speeds could be achieved by a higher repetition-rate laser, a second laser, and/or a larger inspection gage (distance between sensor pairs).

10.4.2 Weld Signatures

One achievement of the tests was the realization that the system showed a different response between "good welds" and "defective welds," hence allowing for the detection of weld defects. This differentiation is rarely achievable by current ultrasonic rail inspection systems. As shown in the example of Figure 10.15, the prototype detected a good weld at 54'6", a 10% TD at 55'0", and a 50% DFW at 59'2". It can be seen in this plot that the response to a "good weld" is a high-level stable plateau with no local minima points, whereas defects and "defective welds" produce a more "jumpy" D.I. with several local minima points. This behavior could be used to train an automatic defect classification algorithm or used under operator's judgment to detect defects within welds.

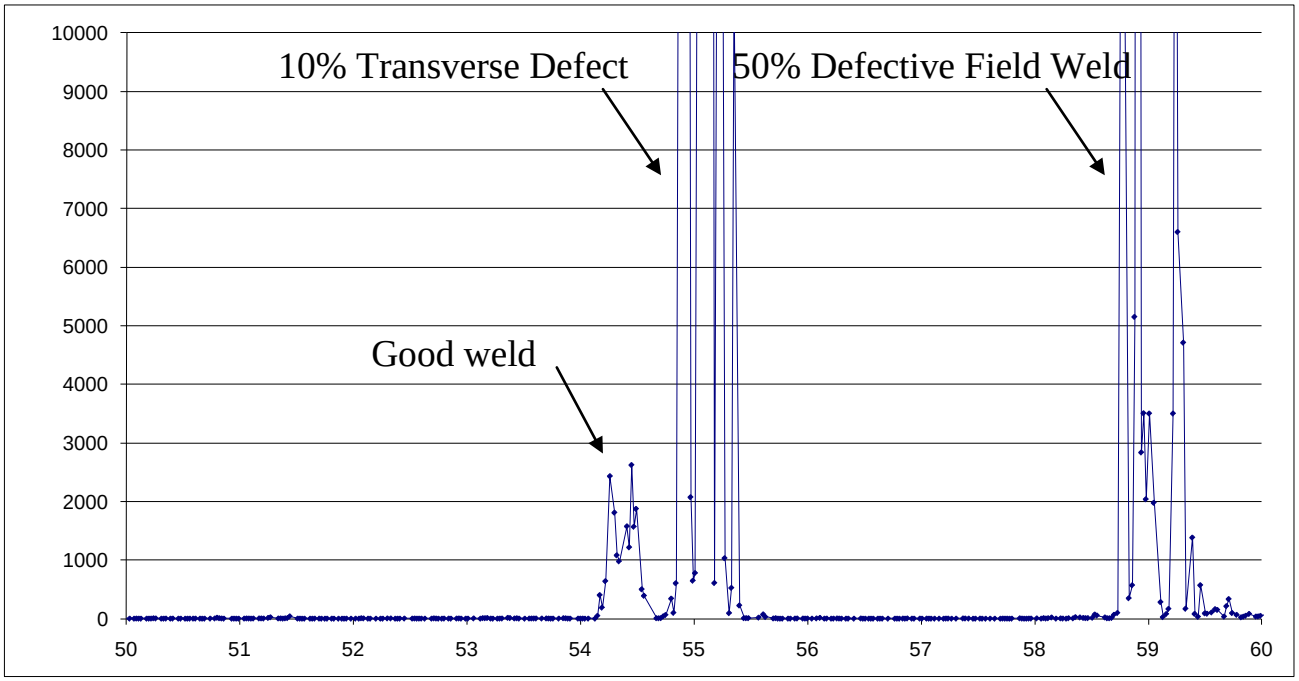

Figure 10.15. Example of Different Signatures of "Good Weld," "TD," and "Defective Weld"

10.4.3 Detection of HSH and VSH Defects

The prototype overall goal was targeting TDs because these are historically the number 1 cause of concern for train accidents. However, the number 2 cause of concern is VSH defects. An excellent outcome of the tests was the realization that the system showed an excellent reliability of detection of the VSH defect. This is an important achievement, because VSH is often missed by conventional ultrasonic rail inspections because its orientation may not render a reflection of the ultrasonic beam from ultrasonic wheel search units. Figure 10.16 shows an example of detection of the 1-foot-long VSH defect present at Herzog's rail defect farm (tie #23 from Table 10.3).

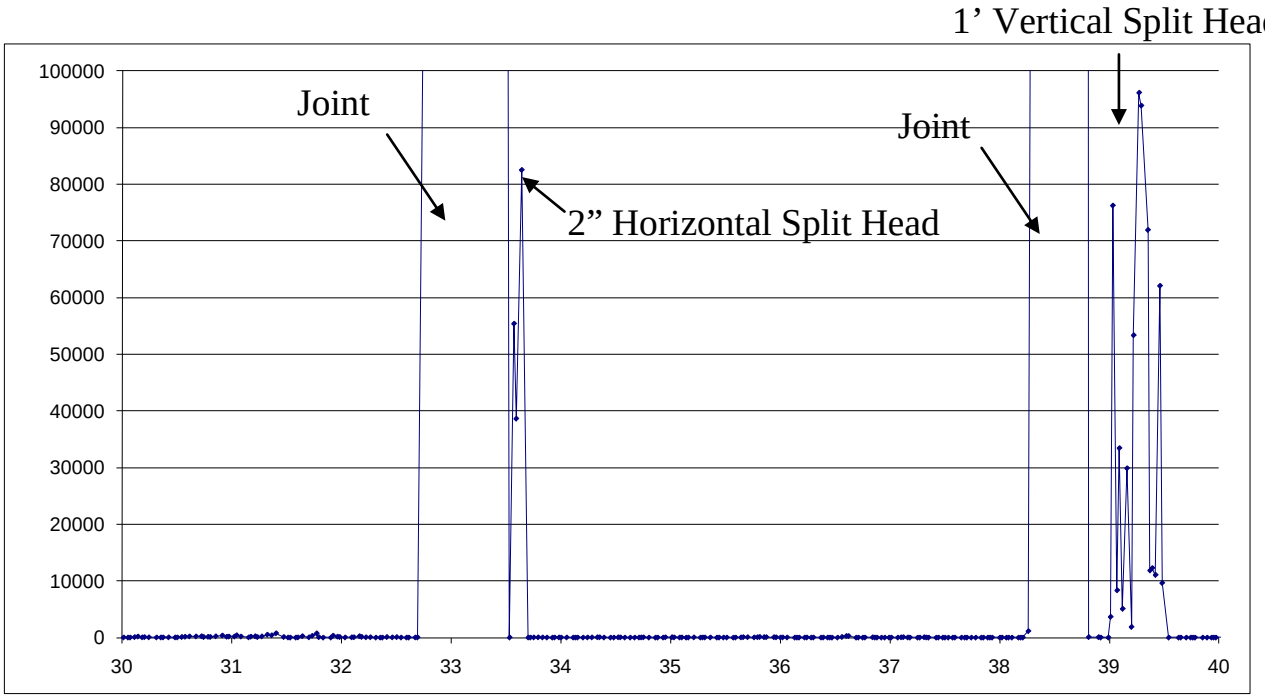

Figure 10.16. Example of Clear Detection of 1-Foot-Long VSH Defect (two joints and an HSH defect also shown)

10.4.4 Conclusions on the Prototype Performance during Seventh Field Test

The system performance at Herzog Services rail defect farm was very promising. The improved water-spraying system worked successfully for the reduction of the noise generated by R-4 at the wheel-rail interface.

The system was able to detect, reliably, TD including some under shelling, side drilled holes, artificial HSHs/VSHs, and defective field and plane welds. The defect detection reliability shown during the blind tests well exceeded industry average and AREMA recommendations.

The system was also sensitive to the presence of good welds but with a different signature than the one related to the flaws. Specifically, the D.I. plotted in real-time indicated a good weld as a high-level stable plateau without local minima, whereas it indicated defects (including defective welds) as peaks with several local maxima with interposed one or more local minima.

After the initial setup, the system did not require any time-consuming adjustments, such as sensor and/or optics alignments. Testing at higher speed (up to the allowed 9 mph) did not show any mechanical/ultrasonic related problem to the prototype. The only problem noticed at higher speeds was the degradation in signal positioning resolution from the desired 0.25-inch interval. This loss in resolution could be avoided with the use of a faster-repetition laser, the use of a second laser firing off-phase from the existing laser, and/or a larger inspection gage (distance between sensor pairs).

Visitors from BNSF and UP, as well as Herzog hosts, made several comments regarding the good performance of the system, particularly pertaining to the following points:

1) Excellent signal-to-noise ratio of the defect indications over the noise floor;
2) Potential to distinguish “good welds” from “defective welds”;
3) Simplicity of hardware; and
4) Ability to detect the VSH defect very clearly.

In addition, personnel from the FRA Office of Railroad Safety pointed out the prototype’s potential to characterize different rail surface conditions related to the severity of shelling, which could be useful to guide rational rail grinding decisions.

11. Construction of the UCSD Rail Defect Farm

It was determined in 2009 that further development of the rail inspection prototype required a new defect farm onsite at UCSD. Such a facility has now been constructed at the UCSD Camp Elliott Field Station, approximately 8 miles from the main UCSD campus. The Camp Elliott Field Station hosts also some of UCSD's high-visibility structural testing facilities, including the world-only Outdoor Shake Table for earthquake engineering testing and the Blast Simulator Facility for blast studies.

The new UCSD/FRA Rail Defect Farm (Figure 11.1) is a 250-foot-long track with a tangent portion and an 8° curved portion. BNSF donated the rails and most of the ties and ballast. Sopac Rail, Inc., performed the construction. The track features approximately 15 natural rail defects, including TDs under shelling, and some artificial rail defects. This facility will be used primarily for the technology development of the FRA/UCSD rail inspection prototype. It is also expected that the facility will be available to other developers of rail inspection technologies.

Figure 11.1. The New Rail Defect Farm at UCSD for Development of Rail Inspection Technologies
(Funding provided by the FRA with in-kind material donation by BNSF.)

12. Conclusions and Recommendations for Future Studies

The performance of the UCSD/FRA rail inspection system at Herzog's rail defect farm was very promising. Two blind tests were conducted at a slow speed (~2 mph). The system was able to detect, reliably, TDs including some under shelling, side drilled holes, artificial HSHs and VSHs, and defective field and plane welds. The defect detection reliability shown during the blind tests exceeded the industry average and AREMA recommendations. Also, as an observation of particular interest not originally foreseen, the prototype appears capable of distinguishing defective and nondefective welds. The system proved to be sensitive to the presence of good welds but with a different signature than the one related to the flaws.

Successful results were equally obtained testing at walking speed and at 5 mph. Testing at higher speeds (up to the allowed 9 mph in the Herzog's test track) was also conducted after the blind tests. The system performed well at these speeds, although with a decreased position resolution compared with the lower speeds. Modifications to the system hardware are necessary to achieve robust performance at the higher speeds.

Interesting outcomes of the Herzog tests were also the excellent detectability of the VSH defect and the potential for characterizing different rail surface conditions, which could be useful to better schedule rail grinding operations. Overall, the prototype meets the original research and development project's objective, which was defined as efficient and reliable rail defect detection from a moving rail car. In this regard, the performance characteristics of particular interest of the prototype, at this final stage, are:

1) Excellent signal-to-noise ratio of defect indications, enhancing system reliability;
2) Large variety of defect types successfully targeted by the system (TD, HSH, and VSH);
3) Potential to successfully inspect welds;
4) Simplicity of hardware (compared with other systems); and

Tentative future steps leading to full operational development and commercialization of the system may include the following:

- an implementation of an automatic gain control for D.I. visualization to respond adequately to the different rail surface conditions;
- an increase in the number of air-coupled sensors for full coverage of the rail head including gage side, center and field side (current coverage is limited for the field side);
- an upgrade for testing at higher speeds without loss in position resolution, achievable with a faster laser, multiple lasers, and/or different sensor positions); and
- a design and implementation of an automatic pattern recognition algorithm for distinguishing good welds from defective welds and defects automatically.

The new UCSD Rail Defect Farm facility, a 250-foot-long track with a number of artificial and in-service defects built with FRA funding and BNSF in-kind support, is available for technology development of this and others rail inspection technologies.

13. References

Bartoli, I., Lanza di Scalea, F., Fateh, M., and Viola, E. (2005). Modeling guided wave propagation with application to the long-range defect detection in railroad tracks. *NDT&E International*, *38*(5), 325–334.

Bartoli, I., Marzani, A., Lanza di Scalea, F., and Viola, E. (2006). Modeling wave propagation in damped waveguides of arbitrary cross-section. *Journal of Sound and Vibration*, *295*, 685–707.

Castaings, M., and Hosten, B. (2003). Guided waves propagating in sandwich structures made of anisotropic, viscoelastic, composite materials. *The Journal of the Acoustical Society of America*, *113*, 2622–2634.

Coccia, S., Bartoli, I., Phillips, R., Salamone, S., Lanza di Scalea, F., Fateh, M., and Carr. G. (2009). *UCSD/FRA ultrasonic guided-wave system for rail inspection*. In *Proceedings from the AREMA Annual Conference*, 20–23 Sept., Chicago, IL.

Federal Railroad Administration. (2008). Safety statistics data: 1998–2008. Washington, DC: U.S. Department of Transportation.

Hayashi, T., Song, W. J., and Rose, J. L. (2003). Guided wave dispersion curves for a bar with an arbitrary cross-section, a rod and rail example. *Ultrasonics*, *41*, 175–183.

Hesse, D., and Cawley P. (2006). Surface wave modes in rails. *The Journal of Acoustical Society of America*, *120*(2), 733–740.

Lanza di Scalea, F., and McNamara, J. (2004). Measuring high-frequency wave propagation in railroad tracks by joint time-frequency analysis. *Journal of Sound and Vibration*, *273*, 637–651.

Lanza di Scalea, F., Bartoli, I., Rizzo, P., and Fateh, M. (2005a). High-Speed Defect Detection in Rails by Non-contact Guided Ultrasonic Testing. *Journal of the Transportation Research Board*, *1916*, 66–77; http://trb.metapress.com/content/m5513168721l5r207/fulltext.pdf.

Lanza di Scalea, F., Rizzo, P., Coccia, S., Bartoli, I., Fateh, M., Viola, E. and Pascale, G. (2005b). Noncontact ultrasonic inspection of rails and signal processing for automatic defect detection and classification. *Insight*, *47*(6), 346–353.

Lanza di Scalea, F., Rizzo, P., Coccia, S., Bartoli, I., and Fateh, M. (2006). Laser–air-coupled hybrid noncontact system for defect detection in rail tracks: Status of FRA prototype development at University of California–San Diego. *Journal of the Transportation Research Board*, *1943*, 57–64; http://trb.metapress.com/content/jrm2n74210210n84/fulltext.pdf.

Lanza di Scalea, F. (2007a). Ultrasonic testing applications in the railroad industry. In P. O. Moore (Ed.), *Nondestructive testing handbook* (3rd ed.) (pp. 535–540). Columbus, OH: American Society for Nondestructive Testing.

Lanza di Scalea, F., Rizzo, P., Coccia, S., Bartoli I., and Fateh M. (2007b). On-line high-speed rail defect detection—phase III. In P. S. Ranade (Ed.), *Technology in rail transport management* (pp. 55–65). Hyderabad, India: The Icfai University Press.

Lee, C. M., Rose, J. L., and Cho, Y. (2009). A guided wave approach to defect detection under shelling in rail. *NDT&E International*, *2*(3), 174–180.

Loveday, P. W. (2009). Semianalytical finite element analysis of elastic waveguides subjected to axial loads. *Ultrasonics*, *49*(3), 298–300.

National Transportation Safety Board. (1994). *Derailment of Burlington Northern Freight Train no. 01-142-30 and release of hazardous materials in the town of Superior, Wisconsin, June 30, 1992* (NTSB Report No. HZM-94-01). Washington, DC: National Transportation Safety Board.

National Transportation Safety Board. (2008). *Railroad accident brief: Derailment of CSX transportation train no. Q39010, Oneida, New York, March 12, 2007* (NTSB Report No. RAB-08-05). Washington, DC: National Transportation Safety Board; http://www.ntsb.gov/publictn/2008/RAB0805.pdf.

Rose, J. L. (1999). *Ultrasonic Waves in Solid Media*, Cambridge University Press, Cambridge, U.K.

Rose, J. L., Avioli, M. J., Mudge, P., and Sanderson, R. (2004). Guided wave inspection potential of defects in rail. *NDT&E International*, *37*(2), 153–161.

Ryue, J., Thompson, D. J., White, P. R., and Thompson, D. R. (2008). Investigations of propagating wave types in railway tracks at high frequencies. *Journal of Sound and Vibration*, *315*(1–2), 157–175.

Thompson, D. J. (2008). A continuous damped vibration absorber to reduce broad-band wave propagation in beams. *Journal of Sound and Vibration*, *311*(3–5), 824–842.

Wilcox, P., Evans, M., Pavlakovic, B., Alleyne, D. N., Vine, K., Cawley, P., and Lowe, M. J. S. (2003). Guided wave testing of rail. *Insight*, *45*, 413–420.

Abbreviations and Acronyms

AREMA	American Railway Engineering and Maintenance-of-Way Association
BHC	bolt hole crack
CG	center gage
CF	center field
DF	detail fracture
DFW	defective field weld
D.I.	damage index
DM	distance marker
DPW	defective plant weld
EDH	end drilled hole
EMI	electromagnetic interference
FE	finite element
FRA	Federal Railroad Administration
ft	feet
GET	Gettysburg and Northern Railroad
H.A.	head area
HF1	high-frequency parameter of sensor pair 1
HF2	high-frequency parameter of sensor pair 2
H.F.-D.I.	high-frequency damage index
HSD	head surface damage
HSH	horizontal split head
HV	head void
ID	internal defect
in	inch
J	joint
kHz	kilohertz
LE	leading edge of tie
LF1	low-frequency parameter of sensor pair 1
LF2	low-frequency parameter of sensor pair 2
L.F.-D.I.	low-frequency damage index

MHz	megahertz
mm	millimeter
mph	mile(s) per hour
NI	National Instruments
Np	Nepers
NTSB	National Transportation Safety Board
POD	probability of detection
Ppk	peak-to-peak
RCF	rolling contact fatigue
RE	short for AREMA
RMS	root mean square
SAFE	Semianalytical Finite Element
SB	slotted base
SC	surface cut
SCB	saw cut base
SCH	saw cut head
SDH	side drilled hole
s.p.	sensor pair
SPBW	superimposition of bulk waves
3-D	three-dimensional
TDD	transverse detail defect
TE	trailing edge of tie
TF	transverse fissure
TGMS	Track Geometry Measurement System
TTC	Transportation Technology Center
TTCI	Transportation Technology Center, Inc.
UCSD	University of California–San Diego
UPS	uninterruptible power supply
VSH	vertical split head
WSC	web saw cut